

0.1 Manifestation and Origin of the Isotope Effect.

V.G. Plekhanov

Computer Science College, Erika Street 7a, Tallinn 10416, Estonia.

Abstract. This article reviews from one point of view the current status of the manifestations of isotope effect in a nuclear, atomic and molecular as well as solid state physics. Although these manifestations vary, they have one common feature - they all depend on mass. Such view allows to see the success and failure as well as the borders of the isotope effect. Force constant dependence on the isotope mass as well as "mass - independent" isotope effect explicitly gives evidence to these borders. The dependence of the energy of zero - point vibrations on the mass of isotopes puts forward the unique possibility of the experimental study of its, for instance, in isotope - mixed crystals. The energy of zero - point vibrations in isotope - mixed crystals obtained from experiments turned out, as a rule, to be compared (excluding $^{12}\text{C}_x^{13}\text{C}_{1-x}$, $\text{LiH}_x\text{D}_{1-x}$ mixed crystals) to the energy of the longitudinal optical phonons. This is the first experimental determination of the energy zero - point vibrations, that is, on the other hand, a witness to the correct quantum electrodynamics in solids. The analysis of the neutron β - decay accompanying the participation of different kind of quarks allows to trace the "disappear" mass in this process. At present time we don't explain not only the observed mass pattern (M_n , M_p , m_u , m_d , etc.) but also the Standard Model can't explain the origin of the mass of elementary particles and their hierarchy. The last one don't permit to find the origin of the isotope effect. To explain this the New Physics as in Cosmology and Nuclear Physics beyond the Standard Model is required.

1. Introduction.

2. Sub - nucleonic structure and the modern picture of isotopes.

- 2.1. The nucleons and its constituents.
 - 2.1.1. Mass and nuclear binding energy.
 - 2.1.2. The nuclear radius.
- 2.2. The force between nucleons.
- 2.3. Nucleon structure.
 - 2.3.1. Quarks and leptons.
 - 2.3.2. Strong and weak interactions.
- 2.4. Isotope effect in nuclear physics.
- 2.5. The origin of the mass.
- 2.6. New physics beyond the Standard Model.

3. Isotopes in atomic and molecular physics.

- 3.1. Some general remarks.

- 3.2. Motion of the nucleus - atomic isotope shift.
- 3.3. Separation of mass - and field shift contributions.
 - 3.3.1. Mass isotope shift.
 - 3.3.2. Field isotope shift.
- 3.4. Vibrations in a diatomic molecule.
 - 3.4.1. Raman and IR spectra of molecules.
 - 3.4.2. Isotope shift in molecular frequencies.
 - 3.4.3. "Mass - independent" isotope effect.

4. Isotope Effect in Solids.

- 4.1. Elementary excitations.
- 4.2. Phonons.
- 4.3. Electronic excitations.
- 4.4. Effects related to isotopic disorder.
 - 4.4.1. Thermal conductivity.
 - 4.4.2. Disorder - induced Raman scattering.
 - 4.4.3. Effects of isotope randomness on electronic properties and exciton transition.
- 4.5. Zero - point vibration energy.

5. Some modern application of the stable and radioactive isotopes.

- 5.1. Stable isotopes.
 - 5.1.1. Traditional applications.
 - 5.1.1.1. Diffusion.
 - 5.1.1.2. Neutron transmutative doping of semiconductors.
 - 5.1.1.3. Optical fiber.
 - 5.1.1.4. Laser materials.
 - 5.1.2. New applications - quantum information.
- 5.2. Radioactive isotopes.
 - 5.2.1. Human health.
 - 5.2.2. Geochronology.
 - 5.2.3. Solid state physics.

6. Conclusion.

Acknowledgments.

7. References.

PACS: 03.67.-a; 24.85.+p; 29.25.Rm; 31.30.Gs; 32.10.Bi; 33.20.-t; 42.65.-k; 82.20.Tr; 91.80.Hj.

Keywords: physics of isotopes; zero-point energy; mass of quarks; standard model.

Introduction.

Investigation, manufacture and application of isotopes are highly variety and is determined by the different areas of science and technique. The range of the application of isotopes is exclusively wide: starting with the investigation of universal principle of the structure matter and common normality evolution of Universe [1; 2] and finished by different biochemical process in live organisms as well as special technical applications [3]. The presence of isotopes and isotope effect in nature serves the bright illustration of the mutual connection between simplicity and complexity in science [4].

The paramount meaning has the role of isotopes in the fundamental natural science investigations. This includes not only the study nature nuclear interactions and, in this way, the origin of isotope effect, but also the reconstructions of nucleogenesis process of the Universe, which could explain the observable in nature relative spreading of chemical elements [1; 2]. As is well-known, one of the intrigue peculiarity in the dependence on their atomic number is a sharp gap at the transition from light elements to hard one - the region of Li, Be, B and further to carbon. The observable gap connects with the next reason: the synthesis of the light elements is accompanied by the couple collisions between nucleon and nucleus with subsequent decay inside stars [5]: $d + n \longrightarrow T \longrightarrow {}^3\text{He} + n \longrightarrow {}^4\text{He}$. Couple mechanism cuts off the symmetric nucleus ${}^4\text{He}$ because such nucleus ${}^5\text{He}$ doesn't exist it is therefore impossible transition to hard nuclides. This paradox overcomes with help of three particle scheme - synthesis C nucleus and 3α - particles [2]: $3\alpha \longrightarrow {}^{12}\text{C}$. This reaction opens the synthesis of the hard elements.

Before describing the contents of the next chapters of the present review let's dwell on the sources of nuclear physics and its structure which would allow to make the isotope effect model more transparent.

Investigations of the atomic nucleus, and the fundamental forces that determine nuclear structure as is well-known offer fascinating insights into the nature of the physical world [5-15]. We all well-known that the history of the nuclear physics dates from the latter years of the nineteenth century when Henry Becquerel in 1896 discovered the radioactivity. He was working with compounds containing the element uranium. Becquerel found that photographic plates covered to keep out light became fogged, or partially exposed, when these uranium compounds were anywhere near the plates. Two years after Becquerel's discovery, Pierre and Marie Curie in France and Rutherford in England succeeded in separating a naturally occurring radioactive element, radium ($Z = 88$) from the ore. It was soon revealed that there are three, distinctly different types of radiation emitted by radioactive substances. They were called alpha (α), beta (β) and gamma (γ) rays - terms which have been retained in ours days. When a radioactive source was placed in a magnetic field, it was found that there were

three different of activity, as the trajectories of some of the rays emitted were deflected to one direction, some to the opposite direction, and some not affected at all. Subsequently it was found that α - rays consist of positively charged ${}^4\text{He}$ nuclei, β - rays are made of electrons (positrons) and γ - rays are nothing but electromagnetic radiation that carries no net charge. The existence of the nucleus as the small central part of an atom was first proposed by Rutherford in 1911. Rutherford proposal that the atom does consist of a small, heavy positively charged centre surrounded by orbiting electrons which occupy the vast bulk of the atoms volume. The simplest atom - hydrogen - consisted of a proton and a single orbital electron. Later, in 1920, the radii of a few heavy nuclei were measured by Chadwick and were found to be of the order of 10^{-14} m., much smaller than the order of 10^{-10} m for atomic radii (for details, see e.g. [7-12]).

The building blocks of nuclei are neutrons and protons, two aspects, or quantum states, of the same particle, the nucleon. Since a neutron does not carry any net electric charge and is unstable as an isolated particle (see, below), it was not discovered until 1932 by Chadwick, whose existence has been anticipated by Rutherford as early as 1920. Since only positive charges (protons) are present in nucleus, the electromagnetic force inside a nucleus is repulsive and the nucleons cannot be held together unless there is another source of force that is attractive and stronger than Coulomb. Here we have our first encounter with strong interaction (see, also Table 1). In the 1934 Hideki Yukawa proposed the first significant theory of the strong force to explain how the nucleus holds together. As we know, with Fermi and Yukawa's papers the modern model of the atom was complete [5-9].

Studies of the structure of the nucleus have shown that it is composed of protons and neutrons, and more recently studies [15-17] of very high energy collisions have shown that these protons and neutrons are themselves composed of elusive particles called quarks. Particle physics deals with the world of the quarks and all other particles still thought to be fundamental. One may argue that, since nuclear force is only one aspect of the strong interaction between quarks, all we need therefore to do is to understand quantum chromodynamics (QCD)^{1*)} (for details see [15-18] and below). The structure of neutrons and protons is discerned only at very high energies (see, e.g. [18]) and, for all practical purpose concerning nuclear structure, research and nuclear physics applications in the modern world, the neutron - proton model of the nucleus is entirely adequate.

1*)QCD is the modern theory of the strong interaction. QCD, the theory of quarks, gluons and their interactions, is a self-contained part of the Standard Model (see below) of elementary particles. Historically its route are in nuclear physics and the description of ordinary matter - understanding what protons and neutrons (and their structure) and how they interact. Nowadays QCD is used to describe most of what goes at high - energy accelerators.

Thus, our present knowledge of physical phenomena suggests that there are four types of forces between physical objects:

- 1) gravitational;
- 2) electromagnetic;
- 3) strong and
- 4) weak.

Both gravitational and electromagnetic forces are infinite in range and their interaction strength diminish with the square of the distance of separation. Clearly, nuclear force cannot follow the same radial dependence. Being much stronger, it would have pulled the nucleons in different nuclei together into a single unit and destroy all the atomic structure we are familiar with. In fact, nuclear force has a very short distance. As we know at present time, only three particles, the proton, the electron and the photon, are stable. Another particle, the neutron, is stable when it is bound within a nucleus, and is unstable with life-time of 887 ± 2 s when it is free (for details see, also [15-17]). Since nuclei are involved in a wide variety of applied and pure research, nuclear physics overlaps with a number of other fields of physics: particles; astrophysics; stellar evolution etc. Therefore, the primary aim of nuclear physics is to understand the force between nucleons, the structure of nuclei, and how nuclei interact with each other and with other subatomic particles. These three questions are, to a large extent, related with each other. Much of current research in nuclear physics (see, e.g. [4-14]) relates to the study of nuclei under extreme conditions such as high spin and excitation energy. Nuclei may also have extreme shapes (for instance similar to that American footballs) or extreme neutron-to-proton ratios. Modern experimenters can create such nuclei using artificially induced fusion or nucleon transfer reactions, employing ion beams from different sources. Beams with even higher energies (e.g. from accelerator) can be used to create nuclei at very high temperatures, and there are signs that these experiments have produced phase transition from normal nuclear matter to a new state, the quarks condensate, the quark-gluon plasma, in which the quarks mingle with one another, rather than being segregated in triplets as they are in neutrons and protons.

If in the nuclear physics the meaning of isotope is establishing one [10, 12, 13, 18] then application isotope effect in atomic [19 - 22] and molecular [23 - 25] physics allow to get the results, which are difficult to overestimate so far as owing to this results it was to construct the "building" of the science of 20 century - the quantum mechanics. The last fifty years the isotope effect is one of the modern and power methods to investigation of structure and properties of solids. This conclusion support the numerous reviews (see, e.g. [26 - 28]) and first monographs [3, 19] dedicated to isotope effect of stable isotopes. In the last years the more and more investigations of solid state physics are conducted by using radioactive isotopes, which give evidence already comprehensive list of references (see, for instance [30 - 33]). It is a well-known fact large and successful application of the radioactive elements in medicine [34 - 36], the direction in isotope physics, which is more finance supportive in different states (see, for example, [37] and references therein). Moreover it is obviously a leading role of the isotope physics at the study of the nature nuclear interactions and reconstruction of nucleogenesis process in the Universe [1, 2, 38] which could be

explained as the observable in nature relative spreading of chemical elements.

Such wide field of isotope applications stimulate necessity for examination and critical analysis from one point of view the microscopical nature of isotope effect. Such approach to isotope physics allow to make known not only the intrinsic contradiction inherent this area of physics but also determine the borders of the effect. The expedient of such approach is not only obvious, but also topical so far as the author of present review knows no such similar paper. With the aim of filling up this gap undertakes the present attempt to consider not only the isotope physics from the very common position (from quarks to condensed matter) but also indicate the principle of new isotope application in quantum information. A step-by-step comparison with existing theoretical models not only revealing the degree of agreement (or disagreement) but provide a new impulse both for the development of new theoretical ideas and for conducting new experiments.

The present review consists of five part. First one is traditional introduction in subject of writing. The second part devotes to the short description of the ground of nature of isotope effect. With this aim the detail analysis of the neutron and proton structure and their mutual transformation in the weak interaction process was conducted. Noted, that the main characteristics of isotope effect - the mass of free particles (proton and neutron) doesn't conserve in the weak interaction process. This contradiction is removed although partly if we take into account the modern presentation [39 - 41] that the mass of proton (neutron) is created from quark condensate (not from constituent quarks [18, 41]) which is the coherent superposition of the states with different chirality. Thus the elucidation of the reason of origin of the nucleon mass is taken down to elucidation of the reason to break down the chiral symmetry in Quantum Chromodynamics [42 - 47]. Isotope effect in atomic and molecular physics shortly describe in third part. Here is an example of mass independent isotope effect. In a more detailed fourth part of the review is considered the manifestation of isotope effect in phonon and electron (exciton) states of solids. With comparison to the change of corresponding characteristics (for example: the lines shift in absorption, scattering, emission spectra) at the isotope effect in atomic physics and condensed matter physics on two orders more in solid (see, for example [48]). In this part the try to determination of the border of isotope effect and force constant in isotope effect on the isotope mass is made. It is underlined that taking into account only linear part of electron - phonon interaction is not sufficient for the description of the experimental facts on the elementary excitations of systems consisting of light elements with isotope effect.

The subject of quantum information brings together ideas from quantum physics, classical information theory and computer science. This topic is devoted the fifth part of review. It is very significant that information can be expressed in different ways without losing its essential nature, since this leads to the possibility of the automatic manipulation of information - a machine need only be able to manipulate quite simple things like integers in order to do surprisingly powerful information processing. It is easy to do from document preparation to differential calculus and even to translating between human lan-

guages.

We should remind that quantum mechanics has developed originally as a theory to explain behavior of large number (ensembles) of microscopic objects, such as atoms or electrons [49]. However over the last decades, considerable interest in the application of quantum theory to individual systems - mesoscopic and even macroscopic systems where a small number of collective degree of freedom show genuine quantum behavior (see, e.g. [50]). One exciting aspect of this developing fundamental research is its technological potential. It results that might be termed quantum information technology. As we well know, the first deep insight into quantum information theory came with Bell's 1964 analysis [51] of the paradoxical thought-experiment by Einstein and coworkers in 1935 [52]. Bell's inequality draws attention to the importance of correlations between separated quantum objects which have interacted in the past, but which no longer influence one another. In essence his argument shows that the degree of correlation which can be present in such systems exceeds that which could be predicted on the basis of any law of physics which describes particles in terms of classical variables rather than quantum states. The next link between quantum mechanics and information theory came about when it was realized that simple properties of quantum systems, such as the unavoidable disturbance involved in measurement, could be put to practical use in quantum cryptography (see, e.g. review [53] and references therein). Quantum cryptography covers several ideas, of which the most firmly established is quantum key distribution. This is an ingenious method in which transmitted quantum states are used to perform a very particular communication task. The significant feature is that the principles of quantum mechanics guarantee a type of conservation of quantum information, so that if the necessary quantum information arrives at the parties wishing to establish a random key, they can be sure it has not gone elsewhere, such as to spy. In this part of review consider not only theory of cryptography but also its practical application [54].

Some unsolved and difficult task of isotope physics are listed in conclusion. From the immense volume of literature concerned with isotope physics and its application we primarily selected those review and monographs which contain extensive references.

2. Sub - nucleonic structure and the modern picture of isotopes.

2.1. The nucleons and its constituents.

An atom consists of an extremely small, positively charged nucleus (see Fig. 1) surrounded by a cloud of negatively charged electrons. Although typically the nucleus is less than one ten-thousandth the size of the atom, the nucleus contains more than 99.9% of the mass of the atom. Atomic nucleus is the small, central part of an atom consisting of A - nucleons, Z - protons and N - neutrons (Fig.2). The atomic mass of the nucleus, A , is equal to $Z+N$. A given element can have many different isotopes, which differ from one another by the number of neutrons contained in the nuclei [55]. In a neutral atom, the number of electrons

orbiting the nucleus equals the number of protons in the nucleus. As usually nuclear size is measured in fermis ($1\text{fm} = 10^{-15}\text{m}$, also called femtometers). The basic properties of the atomic constituents can be read in Table 2.

As we can see from this Table, protons have a positive charge of magnitude $e = 1.6022 \cdot 10^{-19}\text{ C}$ (Coulombs) equal and opposite of that of the electron. Neutrons are uncharged. Thus a neutral atom (A, Z) contains Z electrons and can be written symbolically as ${}^A_Z\text{X}_N$ (see also Fig. 2). Here X is chemical symbol and N is neutron number and is equal $N = A - Z$ ^{2*)}. The masses of proton and neutron are almost the same, approximately 1836 and 1839 electron masses (m_e), respectively. Apart from electric charge, the proton and neutron have almost the same properties. This is why there is a common name of them: nucleon. Both the proton and neutron are nucleons. As we well know the proton is denoted by letter p and the neutron by n . Chemical properties of an element are determined by the charge of its atomic nucleus, i.e. by the number of protons (electrons). It should be added, that although it is true that the neutron has zero net charge, it is nonetheless composed of electrically charged quarks (see below), in the same way that a neutral atom is nonetheless composed of protons and electrons. As such, the neutron experiences the electromagnetic interaction. The net charge is zero, so if we are far enough away from the neutron that it appears to occupy no volume, then the total effect of the electric force will add up to zero. The movement of the charges inside the neutrons do not cancel however, and this is what gives the neutron its nonzero magnetic moment.

2*) Nuclei with the same N and different Z are called isotones, and nuclides with the same mass number A are known as isobars. In a symbolic representation of a nuclear species or nuclide, it is usual to omit the N and Z subscripts and include only the mass number as a superscript, since $A = N + Z$ and the symbol X representing the chemical elements.

Each of the atomic constituents has a spin $1/2$ in units of \hbar ($= \hbar/2\pi$) and is an example of the class of particles of half-integer spin known as fermions. Fermions obey the exclusion principle of Pauli (see, e.g. [12], which determines the way electrons can occupy atomic energy states. The same rule applies, as will be shown below, to nucleons in nuclei. Associated with the spin is a magnetic dipole moment. Compared with the magnetic moment of electron, nuclear moments are very small. However, they play an important role in the theory of nuclear structure. It may be surprising that the uncharged neutron has a magnetic moment. This reflects the fact that it has an underlying quark substructure (see, e.g. [56]), consisting of charged components. Electron scattering off these basic nuclear constituents (proton and neutron) makes up for the ideal probe to obtain a detailed view of the internal structure. A very detailed analysis using the best available data has been carried out recently by Kelly [57], these data originate from recoil or target polarization experiments. In Fig. 3 the proton charge and magnetization distributions are given. What should be noted is the softer charge distribution compared to the magnetic one for proton. These resulting densities are quite similar to Gaussian density distributions that can be expected

starting from quark picture (for details, see below) and, at the same time more realistic than the exponential density distributions [57]. The neutron charge and magnetization are also given in Fig. 3. What is striking is that magnetization distribution resembles very closely the corresponding proton distribution. Since scattering on neutrons normally carries the larger error (see, e.g. [9,10], the neutron charge distribution is not precisely fixed. Nonetheless, one notices that the interior charge density is balanced by a negative charge density, situated at the neutron surface region, thereby making up for the integral vanishing of the total charge of the neutron.

We should remind from atomic physics that the quantity $e\hbar/2m$ is called magneton. For atomic motion we use the electron mass and obtain the Bohr magneton $\mu_B = 5.7884 \cdot 10^{-5} \text{eV/T}$. Putting in the proton mass we have the nuclear magneton $\mu_N = 3.1525 \cdot 10^{-8} \text{eV/T}$. Note that $\mu_N \ll \mu_B$ owing to the difference in the masses, thus under most circumstances atomic magnetism has much larger effects than nuclear magnetism. Ordinary magnetic interactions of matter (ferromagnetism, for example) are determined by atomic magnetism.

We can write

$$\mu = g_l \mu_N \quad (1),$$

where g_l is the g - factor associated with the orbital angular momentum l . For protons $g_l = 1$, because neutrons have no electric charge; we can use Eq. (1) to describe the orbital motion of neutrons if we put $g_l = 0$. We have thus been considering only the orbital motion of nucleons. Protons and neutrons, like electrons, as above mentioned also have intrinsic or spin magnetic moments, which have no classical analog but which we write in the same form as Eq (1):

$$\mu = g_s s \mu_N \quad (2),$$

where $s = 1/2$ for protons, neutrons, and electrons (see Table 2). The quantity g_s is known as the spin g - factor and is calculated by solving a relativistic quantum mechanics equation (see, also [12]). For free nucleons, the experimental values are far from the expected value for point particles: proton - $g_s = 5.5856912 \pm 0.0000022$ and neutron - $g_s = 3.8260837 \pm 0.0000018$. Table 3 gives some representative values of nuclear magnetic dipole moments according [58]. The next nonvanishing moment is the electric quadrupole moment. The quadrupole moment eQ of a classical point charge e is of the form $e(3z^2 - r^2)$. If the particle moves with spherical symmetry, then (on the average) $z^2 = x^2 = y^2 = r^2/3$ and the quadrupole moment vanishes (for details, see [11]). Some examples of the values of nuclear electric quadrupole moments are presented in Table 4.

2.1.1. Mass and nuclear binding energy.

Inside a nucleus, neutrons and protons interact with each other and are bound within (as mentioned above) the nuclear volume under the competing influences of attractive nuclear and repulsive electromagnetic forces. This binding energy has a direct effect on the mass of an atom. It is therefore not possible to separate a discussion of nuclear binding energy; if it were, then nucleon would have masses given by $Z_{m_p} + Z_{m_n}$ and the subject would hardly be of interest.

As is well-known, in 1905, Einstein presented the equivalence relationship between mass and energy: $E = mc^2$. From this formula, we see that the speed of light c is very large and so even a small mass is equivalent to a large amount of energy. This is why in nuclear physics it is more convenient to use a much smaller unit called megaelectronvolt ($1\text{MeV} = 1.602 \cdot 10^{-13}\text{J}$). On the atomic scale, $1u$ is equivalent to $931.5 \text{ MeV}/c^2$, which is why energy changes in atoms of a few electron-volt cause insignificant changes in the mass of atom. Nuclear energies, on the other hand, are millions of electron-volts and their effects on atomic mass are easily detectable. For example, the theoretical mass of $^{35}_{17}\text{Cl}$ is $17 \times 1.00782503 + 18 \times 1.00866491 = 35.28899389 \text{ amu}$. Its measured (see below) mass is only 34.96995 amu . therefore, the mass defect and binding energy of $^{35}_{17}\text{Cl}$ are

$$\Delta = 0.32014389 \text{ amu.}$$

$$E_B = \frac{0.32014389 \times 931.5}{35} = 8.520 \text{ MeV/nucleon} \quad (3)$$

and in common sense the binding energy is determined by next relation

$$E_B = Zm_p + Nm_n - B/c^2 \quad (4),$$

where B/c^2 is the actual nuclear mass.

As we can see below, the binding energy of the atoms of most elements have values ranging from about 7.5 to 8.8 MeV [5-10]. The binding energy per nucleon rises slightly with increasing mass number and reaches a maximum value for ^{62}Ni . Thereafter the binding energies decline slowly with increasing mass number. The binding energies of the atoms of H, He, Li and Be are lower than the binding energies of the other elements (see, also Fig. 5 below).

The measurement of nuclear masses occupies an extremely important place in the development of nuclear physics. Mass spectrometry (see, e.g. [59]) was the first technique of high precision available to the experimenter, and since the mass of a nucleus increases in a regular way with the addition of one proton or neutron. In mass spectrometers, a flux of identical nuclei (ions), accelerated (see, e.g. Fig. 3.13 in [17]) to a certain energy, is directed to a screen (photoplate) where it makes a visible mark. Before striking the screen, this flux passes through magnetic field, which is perpendicular to velocity of the nuclei. As a result, the flux is deflected to certain angle. The greater mass, the smaller is the angle. Thus, measuring the displacement of the mark from the center of the screen, we can find the deflection angle and then calculate the mass. The example of a mass-spectrum of a different isotopes of krypton is shown in Fig. 4. From the relative areas of the peaks it can be determine the abundance of the stable of krypton (for details see [58]).

Relative masses of nuclei can also be determined from the results of nuclear reactions or nuclear decay. For example, if a nucleus is radioactive and emits an α - particle, we know from energy conservation that its mass must be greater than that of decay products by the amount of energy released in the decay. Therefore, if we measure the latter, we can determine either of the initial or final nuclear masses if one of them is unknown. An example of this is presented briefly below. At present we shall illustrate some typical reactions, bridging the gap between "classical" methods and the more advanced "high-energy" types of experiments (see, also [10, 57]).

The possible, natural decay processes can also brought into the class of reaction processes with the conditions: no incoming light particle α and $Q > 0$. We list them in the following sequence:

α - decay:

$${}^A_Z X_N \rightarrow {}^{A-4}_{Z-2} Y_{N-2} + {}^4_2 \text{He}_2 \quad (5).$$

β - decay:

$${}^A_Z X_N \rightarrow {}^A_{Z-1} Y_{N+1} + e^+ + \nu_e \quad (\text{p} \rightarrow \text{n} - \text{type}) \quad (6)$$

$${}^A_Z X_N \rightarrow {}^A_{Z+1} Y_{N-1} + e^- + \bar{\nu}_e \quad (\text{n} \rightarrow \text{p} - \text{type}) \quad (6')$$

$${}^A_Z X_N + e^- + e^- \rightarrow {}^A_{Z-1} Y_{N+1} + \nu_e \quad (e^- - \text{capture}) \quad (6'').$$

Here e^- , e^+ , ν_e and $\bar{\nu}_e$ are electron, positron, neutrino and antineutrino.

γ - decay:

$${}^A_Z X_N^* \rightarrow {}^A_Z X_N + h\nu \quad (7).$$

Here X^* is excited nuclei.

Nuclear fission:

$${}^A_Z X_N \rightarrow {}^{A_1}_{Z_1} Y_{N_1} + {}^{A_2}_{Z_2} Y_{N_2} + x \cdot n \quad (8).$$

Since mass and energy are equivalent (see Einstein formula above), in nuclear physics it is customary to measure masses of all particles in the units of energy (MeV). Examples of masses of subatomic particles are given in Table 5.

As was noted above, nuclear binding energy increases with the total number of nucleons A and, therefore, it is common to quote the average binding energy per nucleon (B/A). The variation of B/A with A is shown in Fig. 5. Several remarkable features are immediately apparent. First of all, the curve is relatively constant except for the very light nuclei. The average binding energy of most nuclei is, to within 10%, about 8 MeV per nucleon. Second, we note that the curve reaches peak near $A = 60$, where the nuclei are most tightly bound, light and very heavy nuclei are containing less bound nucleons. Thus, the source of energy production in fusion of light nuclei or fusion of very heavy nuclei can be source of energy [16, 17].

In concluding this paragraph we should remind that it is often stated that ${}^{56}\text{Fe}$ is the most tightly bound nucleus, this is not correct since ${}^{62}\text{Ni}$ is more bound by a difference of 0.005 MeV/nucleon (for details see [61] and references therein). In conclusion, it is very interesting note, that one cubic millimeter of nuclear material, if compressed together, would have a mass around 200 000 tonnes. Neutron stars are composed of such material.

2.1.2. The nuclear radius.

As will be shown in this paragraph nuclei vary from about one to a few fermis in radius. Recall that the Bohr radius of hydrogen is the order 10^{-10} meters, so the nucleus at present time, despite its small size the nucleus has about, as was noted above, 99.9% of the mass of the atom (see, also [5, 6]). Electron scattering off nuclei is, for example, one of the most appropriate methods to deduce radii. The results of this procedure for several different nuclei are shown in Fig. 6. One remarkable conclusion is obvious - the central nuclear charge density is nearly the same for all nuclei. Nucleons do not congregate near the center of the nucleus, but instead have a fairly constant distribution out to the

surface. The conclusion from measurements of the nuclear matter distribution is the same [62]. Under this assumptions of saturation and charge independence each nucleon occupies an almost equal size within the nucleus. Calling r_0 an elementary radius for a nucleon in the nucleus, a most naive estimate gives for the nuclear volume

$$V = 4/3\pi r_0^3 A \quad (9)$$

or

$$R = r_0 A^{1/3} \quad (10).$$

This relation describes the variation of the nuclear radius, with value of $r_0 \simeq 1.2$ fm when deducing a "charge" radius and a "value of $r_0 \simeq 1.4$ fm for the full matter" radius (see also Figs. 3.5 and 3.9 in [8]). In simple way the nuclear radius is defined as the distance at which the effect of the nuclear potential is comparable to that of the Coulomb potential (see Fig. 7).

We should indicate another way to determine the nuclear charge radius is from direct measurement of the Coulomb energy differences of nuclei. Consider, for example, ${}^3_1\text{H}_2$ and ${}^3_2\text{He}_1$. To get from ${}^3\text{He}_1$ to ${}^3\text{H}_1$ we must change a proton into a neutron. As we know, there is strong evidence which suggest that the nuclear force does not distinguish between protons and neutrons. Changing proton into a neutron should therefore not affect the nuclear energy of the three nucleon system: only the Coulomb energy should change, because the two protons in ${}^3\text{He}_1$ experience a repulsion that is not present in ${}^3\text{H}$. The energy difference between ${}^3\text{He}$ and ${}^3\text{H}$ is thus a measure of the Coulomb energy of the second proton, and the usual formula for the Coulomb repulsion energy can be used to calculate the distance between the protons and thus the size of the nucleus.

2.2. The force between nucleons.

The interactions between two nucleons (NN) is one of the central questions in physics and its importance goes beyond the properties of nuclei. Nucleons can combine to make four different few-nucleon systems, the deuteron ($p + n$), the triton ($p + 2n$), the helion ($2p + n$) and the α - particle ($2p + 2n$) (see, e.g. [63 - 65]). These particles are grouped together because they are stable (excluding from the radioactive triton which have a half-life of about twelve years and so may be treated as a stable entity for most practical purpose), have no bound excited states (except the α - particles which has two excited states at about 20 and 22 MeV), and are frequently used as projectiles in nuclear investigations. The absence of stable particles of mass of five provides a natural boundary between few - nucleon systems and heavier nuclei [1, 2, 64]. Few nucleon systems provide the simplest systems to study nuclear structure. The deuteron provides important information about the nucleon-nucleon interaction.

Even before describing any further experimental and theoretical results to study the force between two nucleons, we can already guess at a few of the properties of the N-N force:

1. At short distances it is stronger than the Coulomb force; the nuclear force can overcome the Coulomb repulsion (see also Fig. 7) of protons in the nucleus.

2. At long distances, of the order of atomic sizes, the nuclear force is negligibly feeble. The interaction among nuclei in a molecule can be understood based only on the Coulomb force.

3. Some fundamental particles are immune from the nuclear force. At present time we have not any evidence from atomic structure, for example, that electrons feel the nuclear force at all.

4. The N - N force seems to be nearly independent of whether the nucleons are neutrons or protons. As is well-known this property is called charge independence.

5. The N-N force depends on whether the spins of the nucleons are parallel or antiparallel.

6. The N - N force includes a repulsive term, which keeps the nucleons at a certain average separation.

7. The N - N force has a noncentral or tensor component. This part of the force does not conserve orbital angular momentum, which is a constant of the motion under central forces.

We should add that with knowledge of the N - N interaction provided by $p - p$ and $p - n$ scattering and by the deuteron (see, also [66 - 68]), one can try to calculate the properties of the triton and the helion. The principal properties of few-nucleon systems are summarized in Table 6.

Deuteron. The deuteron is a very unique nucleus in many respects. It is only loosely bound, having a binding energy much less than the average value (≈ 8 MeV [1,2]) between a pair of nucleons in all other stable nuclei. We have seen in Eq. 94) that the binding energy E_B of a nucleus is given by the mass difference between the neutral atom and the sum of the masses of free neutrons and protons in the form of hydrogen atoms. For a deuteron, as we can see from Table 6, the mass M_d is 1876.1244 MeV/ c^2 . The binding energy is then difference between M_d and the sum of those for a neutron m_n and a hydrogen atom m_H ($= m_p$): $m_n c^2 = 939.565$; $m_H c^2 = 938.7833$ MeV and $m_n + m_H = 1878.3489$ MeV. We can write according Eq. (4): $E_B = m_n + m_H - M_d = 2.224$ MeV. A more precise value, $E_B = 2.22457312$ MeV is obtained from radioactive capture of a neutron by hydrogen. In this reaction $p(n, \gamma)d$, a slow neutron is captured by a hydrogen atom followed by the emission of a γ - ray (for details see [69]).

To simplify the analysis of the deuteron binding energy, we will assume that we can represent the N - N potential as three - dimensional square well, as shown in Fig. 8.

$$\begin{aligned} V(r) &= -V_0, \text{ for } r < R (= 2.1 \text{ fm.}) \\ &= 0, \text{ for } r > R \end{aligned} \quad (11).$$

This is of course an oversimplification, but is sufficient for at last some qualitative conclusions. In Eq. (11) r represents the separation between the proton and the neutron, so R is in effect a measure of the diameter of the deuteron (Fig. 9). If we express the energy, corresponding to the ground state value $E = -E_B$, the Schrodinger equation becomes for the one-dimensional, radial problem with zero angular moment, just like the lowest energy state of hydrogen atom.

$$\begin{aligned} \frac{d^2 u}{dr^2} + k^2 u &= 0, \quad r < R \text{ (see, Fig. 10)} \\ \frac{d^2 u}{dr^2} - \alpha^2 u &= 0, \quad r > b \end{aligned} \quad (12),$$

defining

$$k^2 = \frac{m_p}{\hbar^2} (u - E_B), \quad \alpha^2 = \frac{m_p}{\hbar^2} E_B \quad (13)$$

and using the radial solution

$$u(r) = rR(r). \quad (14).$$

Approximate solutions in the two regions became

$$\begin{aligned} u(r) &= A \sin kr, & r < R \text{ and} \\ u(r) &= B e^{-\alpha(r-R)}, & r > b \end{aligned} \quad (15).$$

Matching the logarithmic derivatives at $r = R$ gives

$$k \cot kR = -\alpha \quad (16)$$

and matching the wave functions at $r = R$ gives

$$A \sin kR = B \quad (17).$$

These two relations lead to the condition

$$k^2 A^2 = (k^2 + \alpha^2) B^2 \quad (18).$$

The normalization of the wave function $4\pi \int u^2(r) dr = 1$ becomes

$$\frac{A^2}{2k} (2kR - \sin 2kR) + \frac{B^2}{\alpha} = \frac{1}{2\pi} \quad (19).$$

Eliminating A^2 from the last two equations, gives the value for B as

$$B \simeq \sqrt{\frac{\alpha}{2\pi}} e^{-\alpha R/2} \quad (20).$$

Knowing the binding energy E_B (see, Eq. (13)), we can determine the value $\alpha = 0.232 \text{ fm}^{-1}$. A best value for R can be determined from proton - neutron scattering (see, e.g. [63, 64]) as $R = 1.93 \text{ fm}$. This then gives $u = 38.5 \text{ MeV}$. One can show that this value of u and the value for R just give rise to a single, bound $1s$ state, all other higher-lying $1p$, $1d$, $2s$ being unbound. Since we also have

$$A \simeq B \quad (21)$$

we obtain the final wave functions

$$\begin{aligned} u(r) &= \sqrt{\frac{\alpha}{2\pi}} e^{-\alpha R/2} \sin kr, & r < R \text{ and} \\ u(r) &= \sqrt{\frac{\alpha}{2\pi}} e^{-\alpha R/2} e^{-\alpha r} & r > b \end{aligned} \quad (22).$$

A potential which gives a satisfactory account of the properties of the deuteron given in Table 6 is shown in Fig. 1o. We should add that in all deuteron potentials the tensor term is very sizeable part of the two-nucleon potential, and is characterized by a somewhat larger range than the central potential (see Fig. 10) being appreciably different from zero even when the central potential is already negligible.

Proton - proton and proton - neutron interactions. Most of the present theories (see, also [64] and references therein) of nuclear structure and nuclear reactions are based on the assumption that nuclear properties depend mainly on two-body interactions between its constituents. Three-body forces or many-body forces are expected to play only a minor role^{3*)}. It is thus of paramount importance to describe as accurately as possible the two-nucleon interaction. At the fundamental level this interaction is a consequence of the quark structure of the nucleons and should be described by QCD [65] in terms of the quark-gluon field (see, also [39, 47, 83]).

3*) If the two-body potential has an average strength of 20 MeV, then the three-body one would have a strength of about 1 MeV. We should add that all models have a one-pion exchange character at long range, which gives rise to a spin-spin central potential and a tensor term (for details see [56, 92]).

However this approach is still in its infancy and therefore we are still far from solution. There are also many indications [63] that at interaction energies below a few hundred MeV it is possible to describe the N - N interaction in terms of the exchange of various types of mesons [71 - 73].

In principle there are four types of scattering measurements involving two nucleons that can be carried out. The scattering of an incident proton off a proton (pp - scattering) is the simplest one of the four from an experimental point of view, as it is relatively easy to accelerate protons and to construct targets containing hydrogen. For neutron scattering, there are two major sources for incident beam. At low energies, neutrons from nuclear reactors may be used. At higher energies, one can make use of neutrons produced by a beam of protons, for instance, through a (p,n) reaction on a ${}^7\text{Li}$ target. However, both the intensity and the energy resolution of neutron beams obtained in these ways are much more limited than those for proton beams. As a result, neutron scattering is, in general, a more difficult experiment than those with protons. In addition to pp - and np - measurements, one can, in principle, carry out pn - and nn - scattering experiments as well. Here, instead of using protons as the target,, a neutron target is used. As we know, free neutrons are unstable (see above), with a half-life on the order of 10 min. It is therefore impossible to construct a fixed neutron target, in contrast to protons where material consisting of hydrogen may used.. There are, in principle [72], two methods of getting around this limitations. One way is to carry out a colliding beam experiment. In place of a target fixed in the laboratory, a second neutron beam is used and, instead of having an incident beam scattering from a fixed target, two beams of particles are directed toward each other. Scattering takes place when the particles in the two beam collide. To be practical, such an experiment requires high intensities in both beams, and currently highly intense beams of neutrons are not easily available. The other way is to simulate a fixed neutron target using deuterium. Since the deuteron is a loosely bound system of a neutron and a proton, the desired pn - or nn - scattering results can be obtained by carrying out the corresponding pd - or nd - scattering experiments. The contribution due to protons in the deuterium target may be removed by subtracting from the measured values the corresponding results obtained in pp - or np - scattering. The information obtained from pn - and nn - scattering may not be any different from that in np and pp - scattering. For example, the only difference between pn - and np - scattering is whether the neutron or the proton is the target. Under time-reversal invariance, these two arrangements are expected to give identical results. As early to simplify the notation, we shall use the symbol NN from now on to represent a system of two nucleons, as early, when there is no need to differentiate between neutrons and protons and the symbol np to represent both np - and pn - unless further distinction is required by the occasion. Further

more, we shall assume that Coulomb contribution, where present, has already been taken out and we can therefore ignore it in the discussion.

The quantity measured in a scattering experiment is the number of counts registered by a detector (θ, φ) (see, e.g. [60]). The counting rate depends on the solid angle subtended by the detector at the scattering center, the intensity of the incident beam, the number of target nuclei involved, and the differential cross-section $d\sigma/d\Omega$. Naturally our primary interest is in $d\sigma/d\Omega$, a function of the bombarding energy as well as the scattering angle. For simplicity we shall consider first only elastic scattering, and as a result, the wave number k in the center of mass of the two particles has the same magnitude before and after the scattering. The differential scattering cross-section at angles (θ, φ) is given by next equation

$$\frac{d\sigma}{d\Omega}(\theta, \varphi) = |f(\theta, \varphi)|^2 \quad (23).$$

Here $f(\theta, \varphi)$ is the scattering amplitude. As shown in Fig. 11 the geometry of 0 - scattering arrangement is such that it is coordinate system at the center of the scattering region and take the direction of the incident beam as the positive direction along the z -axis. The incident wave vector \vec{k} and the scattered vector \vec{k}' define a plane, the scattering plane.

For a central potential, the relative angular momentum \vec{l} between the two scattering nucleons is a conserved quantity. Under such conditions, it is useful to expand the wave function as a sum over the contributions from different partial waves, each with a definite l - value

$$\Psi(r, \theta) = \sum_{l=0}^{\infty} a_l Y_{l0}(\theta) R_l(k, r) \quad (24).$$

Here a_l are the expansion coefficients. Only spherical harmonics $Y_{lm}(\theta, \varphi)$ with $m = 0$ appears in the expansion since, in the absence of polarization, the wave functions is independent of the azimuthal angle Φ . We have explicitly included the wave number k have in the arrangement of the radial wave function $R_l(k, r)$ so as to emphasize the dependence of energy.

For a free particle, $V = 0$, and the radial wave function reduces to

$$R_l(k, r) \rightarrow \frac{1}{kr} \sin(kr - \frac{1}{2}l\pi), \quad (25)$$

where $k = \sqrt{2\mu E}/\hbar$ and $j_l(\rho)$ is the spherical Bessel function of order l . If only elastic scattering is allowed by the potential, the probability current density in each partial-wave channel is conserved. The only effect the potential can have on the wave function is a change in the phase angle. In other words

$$R_l(k, r) \text{ (scatt/} r \rightarrow \infty) \rightarrow \frac{1}{kr} \sin(kr - \frac{1}{2}l\pi + \delta_l), \quad (26)$$

where δ_l is the phase shift in the l -th partial - wave channel.

After that, the scattering amplitude may be expressed in terms of δ_l as

$$f(\theta) = \frac{\sqrt{4\pi}}{k} \sum_{l=0}^{\infty} \sqrt{2l+1} e^{i\delta_l} \sin\delta_l Y_{l0}(\theta) \quad (27).$$

In such case the differential scattering cross-section may be written in terms of the phase shift

$$\frac{d\sigma}{d\Omega} = \frac{4\pi}{k^2} \left| \sum_{l=0}^{\infty} \sqrt{2l+1} e^{i\delta_l} \sin\delta_l Y_{l0}(\theta) \right|^2 \quad (28).$$

The scattering cross-section, the integral of $\frac{d\sigma}{d\Omega}$ over all solid angles, becomes

$$\sigma = \int \frac{d\sigma}{d\Omega} d\Omega = \frac{4\pi}{k^2} \sum_{l=0}^{\infty} (2l+1) \sin^2 \delta_l(k) \quad (29).$$

Decomposition into partial waves is a useful way to analyze the scattering results for a given bombarding energy. In particular, only a few of the low-order partial waves can contribute to the scattering at low energies, as shown in Fig. 12. For realistic nuclear potential, the orbital angular momentum is not conserved.

Since we are dealing with identical fermions, the scattering of two nucleons can take place only in a state that is totally antisymmetric with respect to a permutation of the two particles, in the same way as for deuteron. For pp - scattering, we have $T = 1^{4*})$ and the two nucleons are symmetric, as for as their total isospin wave function [56] is concerned. If the intrinsic spins of the two protons are coupled together to $S = 0$ (antisymmetric state) and, as a result, only even l -values are allowed. For $S = 0$, we have $J = l$ (we remind that $\vec{J} = \vec{l} + \vec{S}$), and the partial waves for the lowest two orders of pp - scattering are 1S_0 ($l = 0$) and 1D_2 ($l = 2$). The phase shifts extracted from measured pp - scattering data for these two partial waves of bombarding energy less than 300 MeV, in the laboratory are shown in Fig. 13 as illustrative examples (for details see [74]). Only the real part of the phase shift are given. At laboratory energy less than 300 MeV, contributions from inelastic scattering are still relatively unimportant and the imaginary parts of the phase shifts extracted from measured scattering cross-section are small.

4*) In 1932 Heisenberg suggested [77] on the basis of the approximate of the proton and neutron mass (see also Table 2) that these particles might be considered as two different charge states of a single entity, the nucleon, formally equivalent to the up and down states of a spin 1/2 particle. To exploit this hypothesis the nucleon wave function in addition to a space and a spin component also has an isotopic spin (isospin) component (see, also e.g. [10]).

By the same token, partial waves for triplet ($S = 1$) pp - scattering have odd l - values. The lowest order in this case is a p - wave ($l = 1$). When $l = 1$ is coupled with $S = 1$, three states, with $J = 0, 1, 2$ are produced. The phase shifts for two of the triplet of states, 3P_0 and 3P_1 , are also shown in Fig. 13^a. There is no admixture between the two $J = 0$ states, 3P_0 and 1S_0 as they are of different parity. As a result, we find that both l and S are good quantum numbers here by default (for details see [76] and references therein).

The np - system may be coupled together to either isospin $T = 0$ or $T = 1$. For $T = 0$ the two nucleons are antisymmetric in isospin. In this case the $S = 0$ states must have odd l - values in order to be antisymmetric in the total wave function. The lowest order partial wave here is $l = 1$ and the phase shifts for 1P_1 - scattering extracted from experimental data are shown in Fig. 13^c. In order for p - wave np - scattering to be in the $S = 1$ state, it is necessary for the total isospin to be $T = 1$. The phase shift in this case are expected to be

identical to those found in pp - scattering, if nuclear force is charge independent and Coulomb effects are removed. An examination of the two sets of empirical p - wave phase shifts, 3P_0 and 3P_1 given in Fig.14^b, shows that they are only slightly different from corresponding values given in Fig. 14^a for pp - scattering. It is not clear whether the small differences come from the way the phase shifts are extracted from experimental scattering cross - section or they are indications of a weak charge dependence in the nuclear force.

The other $T = 0$ phase shift in the np - system, shown in Fig. 14^c, are for triplet ($S = 1$), even l - scattering. This is the first time we encounter a mixing of different l - partial waves. Up to now, each phase shift has been characterized by a definite l - value (as well as J - and S - values) even though the orbital angular momentum is not fundamentally a good quantum number. Mixing of different l - partial waves has not taken place because of parity and other invariance conditions, however the tensor force can mix two triplet of the same J but different in l by two units ($l = J \pm 1$) (see also [76]).

2.3. Nucleon structure.

Our present knowledge of nuclear physics suggests that there are two main families of particles leptons and hadrons (baryons and mesons). The hadrons were first thought to be elementary like the leptons, but soon a very large number of hadrons were discovered, which suggests that they are not elementary (see, also 8, 62, 78]). As we can see from Table 6 the leptons are fundamental particles, but hadrons are not. They are made up of quarks [79, 80] (for details see below). The only hadrons found in normal matter are the proton and the neutron. Quarks are one of the two basic constituents of matter which is described QCD. QCD [47, 81, 82] is the theory of the strong interaction, a fundamental force describing the interactions of the quarks and gluons found in nucleons such as the proton and the neutron. QCD is an important part of the Standard Model (SM)^{5*)} of particle physics (see, also [81, 82]). In the present SM [47] there are six "flowers" of quarks (see, below Table 9) most familiar baryons are the proton and neutron, which are each constructed up and down quarks [83 - 85]. Quarks are observed to occur only in combinations of two quarks (mesons), three quarks (baryons), and the recently discovered with five quarks (penti-quarks [83]).

5*) As is well-known, the Standard Model [45, 47, 82, 92, 93] is a unified gauge theory of the strong, weak and electromagnetic interactions, the content of which is summarized by the group structure $SU(3) \times SU(2) \times U(1)$, where $SU(3)$ refers to the theory of strong interactions, QCD, and latter two factors $[SU(2) \times U(1)]$ describe the theory of electroweak interactions. Although the theory remains incomplete, its development represents a triumph for modern physics (for details see [93] and below).

2.3.1. Quarks and leptons.

a) **Quarks.** We now know that all the known properties of the hadrons (their quantum numbers, mass, charge, magnetic moment), their excited states and their decay properties (see, also below) may be explained by assuming that the mesons are made of quark - antiquark pairs, the baryons of three quarks and the antibaryons of three antiquarks [81 - 83]. To obtain this picture we need six quarks: up (u), down (d), charm (c), strange (s), top (t) and bottom (beauty) (b) (see Table 9). These six particles may be arranged according to their masses into three pairs, with one number of each pair having a charge $+2/3e$ and the other $-1/3e$ as shown in Table 9. Since quarks have not been observed in isolation - they appear either as bound quark - antiquark^{6*)} pairs in the form of mesons or bound groups in the form of baryons (see, also Fig. 15 below) - the name assigned to them, up, down, strange, etc., are only mnemonic symbols to identify of different species. The word "flavor" is used, for convenience, to distinguish between different types of quark. Besides flavor, quarks also come in three different color, for example,

6*) The first question that occur is whether the quarks actually exist inside the hadrons or whether they are merely a convenient mathematical ingredient leading to the geometrical symmetry [10]. A substantial clue in this direction is obtained in deep inelastic scattering from nucleons [14 - 16]. The nucleon appears to be made up of to regions in the asymptotic free regime [86 - 88], and the outer region of the meson cloud where pions and other heavy mesons can exist (see, also [89]). A number of early results on the internal proton structure became accessible through highly inelastic electron scattering carried out at the Stanford Linear Accelerator Center (SLAC). Later work of Kendell et al. [14 -16] helped to identify these structures with quarks inside the proton (for details see also [90]).

red, green, and blue. Color and flavor are quantum - mechanical labels, or in other words, quantum numbers, very similar to spin and parity. Since there are no classical analogues to flavor and color degrees of freedom, there are no observables that can be directly associated with them. In this respect, they are similar to the parity label of a state which must be <observed> through indirect evidence.

At now we know that color charge is the charge associated with strong interaction. Color is whimsically named attribute of quarks and gluons [90] that cannot be seen. Gluons have one color and one anticoulour [91]. There are, however, only eight types of gluons [8], not the nine as we might expect. Quarks and gluons are only found inside hadrons. The quarks inside a hadron are bathed in a sea of gluons (and additional quark-antiquark pairs) that are responsible for the binding forces in the hadron. Quarks continually emit and absorb gluons. Color charge is conserved in every such process. The color - mathematics always work out so that at any instant the entire hadron system is color neutral.

For quarks, the interaction is very strong at low energies where nuclear physics operates and where most of the experimental observations are made.

Because of what is generally known as asymptotic freedom [86 - 88], the quark - quark interaction is weak only at extremely high energies. As a result, perturbational techniques apply to QCD only at such extremes, far beyond the realm of nuclear physics and low-lying hadron spectroscopy. Since quarks are not observed in isolation, their mutual interaction must have a component that grows stronger as the distance of separation between them increases. This is opposite to our experience in the macroscopic world, where interactions, such as gravitational and electromagnetic, grow weaker as the distance of separation between the interacting objects is increased (and the relation is given by the inverse square law).

From the above text it has become clear that protons and neutrons are no longer considered as elementary (see, also Fig 15) but are composed of quarks in a bound state. The binding forces are quite distinct from electromagnetic, gravitational forces: at very short distance, the quarks appear to move freely but, with increasing separation, the binding forces increase in strength too. So it is not possible to separate the nucleon into its constituent quarks^{7*)}. From this picture it is followed that quarks are to be able to exist only in combination with other quarks (baryons) or with antiquarks (mesons) [56, 90]. This picture has also modified our ultimate view of a system of densely packed nucleons. For composite

7*) As we know, nonrelativistic quark model use constituent quark masses, which are of order 350 MeV for u- and d-quarks. Constituent quark masses model the effect of dynamical chiral symmetry breaking are not related to the quark mass parameters m_q of the QCD Lagrangian.

nucleons, interpenetration will occur if the density is increased high enough and each quark will find many other quarks in its immediate vicinity (see Fig. 16). The concepts of a nucleon and of nuclear matter become ill - defined at this high - energy limit and a new state of matter might eventually be formed: a quark plasma whose basic constituents are unbound quarks [91; 92]. Starting with matter of vanishing baryon density, the energy density of a non - interacting gas of massless quarks and gluons is (see, also [92])

$$E \simeq 12T^4 \quad (30),$$

here T is temperature. Just like in the Stefan - Boltzman for a proton gas, the numerical factor in (30) is determined by the number of degrees of freedom of the constituent particles: their spins, colors, and flavors. The energy density for quarks plasma via computer simulations obtained in [92]. The transition temperature from the mesonic regime to the plasma regime is around 200 MeV which means an energy density of at least 2.5 GeVfm^{-3} in order to create a quark - gluon plasma.

b) **Leptons.** Leptons are fundamental particles that have no strong interactions. The six known types of leptons are shown in the Table 10. The family of leptons is further subdivided into three generations; the electron and the electron neutrino (e, ν_e), the muon and the muon neutrino (μ, ν_μ), the τ and the τ - neutrino (τ, ν_τ). There are also six antilepton types, one for each lepton [60,

78, 80, 83]. Leptons, or light particle (from greek), are not made of quarks. They, as is indicated above, in electromagnetic and weak interactions but not in strong interaction. As we can see from Table 10 the neutrinos are known to be much lighter and their rest masses may even be zero. A large amount of effort has been devoted in recent years to measuring the mass ν_e . The best estimate at the moment is that it is a few eV or less, although much larger values for the upper limit have also been reported. As we can see from Table 10 for the other two types of neutrinos, only the upper limits of their masses are known: $m_{\nu_\mu} < 0.25$ MeV and $m_{\nu_\tau} < 30$ MeV. In nuclear physics, leptons make their presence felt through nuclear β - decay and other weak transition. In general, only electrons and electron neutrinos are involved; occasionally muons may enter, such as in the case of a muonic atom where a muon replace one of the electrons in atom.

In addition to the properties listed in Table 10, each lepton has a lepton number $L = 1$ (-1 for the corresponding antilepton) and the numbers of each generation are further characterized by a new number, the electron - lepton $L_e = 1$, the muon - lepton number $L_\mu = 1$, and the tau - lepton number $L_\tau = 1$, respectively. Within each generation the antilepton have $L_e = -1$, $L_\mu = -1$, $L_\tau = -1$. These numbers, the lepton number and the lepton number generation, are conserved in all reactions involving leptons (see, e.g. 83, 90)].

The leptons are often produced in hadron decay, that is when a heavier particle subject to the strong interaction spontaneously transforms into lower mass particles. When this occurs, the decay is due to the weak interaction and the corresponding particle life - time is enormously longer than that corresponding to a strong interaction decay. The first of these decays to be discovered was the transformation of a neutron into a proton (Fig. 17). Charge conservation requires that together with proton a negatively charged particle be produced, and conservation of the energy requires that this particle be an electron. However, this is not sufficient to conserve angular momentum because the three particles are all fermions with spin 1/2 and a system made by a proton and an electron alone has integer spin. The decay into a proton and an electron alone also disagrees with the observation that the proton and the electron do not have definite energies as would happen in a two - body decay. It was then postulated by Pauli [see, e.g.[5)] principle that another particle very difficult to observe is emitted at the same time. It is fermion with spin 1/2, which was called the neutrino. The neutron decay was thus written

$$n \rightarrow p + e^- + \tilde{\nu}_e \quad (31),$$

where $\tilde{\nu}_e$ is an electron antineutrino. This decay illustrates some of this conservation laws which govern particle decays.

The proton in the product satisfies the conservation of baryon number, but the emergence of the electron unaccompanied would violate conservation of lepton number. The third particle must be an electron antineutrino to allow the decay to satisfy lepton number conservation. The electron has lepton number 1 and the antineutrino has lepton number -1. However a proton bound in a nucleus may also transform into neutron by emitting a positron and a neutrino. This process is a bound as β^+ - decay and discussed in any textbooks (see,

e.g. [9, 10]). Also for this transformation the above consideration hold and the proton transformation into a neutron was written

$$p_{bound} \rightarrow n + e^+ + \nu_e \quad (32),$$

where ν_e is an electron neutrino. In conclusion of this part, we should note, that the lepton number conservation rule is applied to all cases it is found to work.

As we well-known at present time all hadrons are subdivided into two classes, baryons and mesons (see Fig. 15). Baryons are distinguished by the fact that they are fermions, particles that obey Fermi - Dirac statistics. Because of this property, two baryons cannot occupy the same quantum - mechanical state. The fact that baryons are fermions implies that quarks must also be fermions, as it is impossible to construct fermions except from odd numbers of fermions. Furthermore, if we accept that a quark cannot exist as a free particle, the lightest fermion in the hadron family must be made of three quarks (see also Fig. 15). Among the baryons, we are mostly concerned with the lightest pair, the neutron and the proton. From charge conservation alone, it can be deduced that a proton carrying a charge $+e$, must be made of two u - quarks, each having a charge of $2/3e$ (Table 9), and one d - quark, $-1/3e$. The quark wave function of a proton may be represented as

$$|p\rangle = |uud\rangle \quad (33).$$

Similarly, the quark wave function of a neutron is

$$|n\rangle = |udd\rangle \quad (34)$$

so that the total charge of a neutron in units of e is $2/3 - 1/3 - 1/3 = 0$.

Boson particles obeying Bose - Einstein statistics may be made from even number of fermions. This means that mesons are constructed of an even of quarks. Since, on the one hand, bosons can be created or annihilated under suitable conditions and, on the other hand, the number of quarks is conserved in strong interaction processes, a meson must be made of an equal number of quarks (see, also Fig. 15). The simplest meson is, therefore made of quark - antiquark. For example, pions (π), the lightest members among the mesons, are made of a quark, either u or d and an antiquark, either \bar{u} or \bar{d} (see, e.g. [90]).

2.3.2. Strong and weak interactions.

As was indicated above, our present knowledge of physical phenomena suggests that there are four types of forces between physical bodies:

- 1) gravitational;
- 2) electromagnetic;
- 3) strong;
- 4) weak.

The gravitational and the electromagnetic forces vary in strength as the inverse square of the distance and so are able to influence the state of an object even at very large distances whereas the strong and weak forces fall off exponentially and so act only at extremely short distances.

One common feature of the nuclear interactions is their exchange and tensor character: they occur through exchange of quanta, virtual particles that exist only for a very short time and cannot be detected experimentally. As we know the short range character of the strong and weak interactions is due to the finite mass (in opposite of electrodynamics with massless photon) of the quanta of the respective fields. These are various kind of meson in the case of the strong force and W^\pm and Z particles in the case of the weak interaction. In fact if the exchanged virtual particle has a mass m , its minimum energy is rest mass energy mc^2 . Thus

$$\Delta t \leq \frac{\hbar}{mc^2} \quad (35)$$

and the range of the interaction is always smaller than

$$R \leq \frac{\hbar c}{mc^2} = \frac{\hbar}{mc} \quad (36).$$

In the case of the strong interaction $R \simeq 1.4$ fm, so that the quanta of the field have a mass $m \geq 140$ MeV/ c^2 [47; 72; 75; 92]. In the case of the weak interaction, the high mass of the W^\pm and Z particles ($m_{W^\pm} = 80$ MeV/ c^2 and $m_Z = 91$ MeV/ c^2) makes $R \simeq 10^{-3}$ fm. As already mentioned the basic interactions (four forces) have different strength. Loosely speaking this means that when two of these interactions act together the stronger dominates. A simple criterion to judge the relative strengths is the value of the coupling constants which characterize the corresponding fields, which are of the order of unity for the strong, 10^{-2} for electromagnetic, 10^{-5} for the weak and 10^{-39} for the gravitational forces (see Table 1). However, this does not mean that, for instance, the strong interaction is more effective than the electromagnetic interaction in producing bound states between two interacting particles. For example, the hydrogen atom comprising a proton and an electron bound by the electromagnetic force has an infinity of bound states, whereas the deuteron, the bound system formed by a proton and a neutron interacting through the strong force, has only one bound state.

Nuclear β - decay is one and the oldest of the example of weak interactions. The basic reaction involving weak interaction in nuclei may be characterized by the decay of a neutron and a (bound) proton (see (31, 32) above). on a more fundamental level, β - decay of hadrons may be viewed as the transformation of one type of quark to another through the exchange of charged weak currents [72, 78, 95]. In a proton, the quark takes about 300 MeV to flip the spin of a quark (for example $u \rightarrow d$ quarks transformations). The flavor of quarks is conserved in strong interactions [92, 94]. However, through weak interactions, it is possible for quarks to change flavor, for example, by transforming from d - quark to a u - quark:

$$d \rightarrow u + e^- + \bar{\nu}_e \quad (37).$$

This is what takes place in the β - decay of a neutrons. In terms of quarks, Eq. (31) may be written

$$(udd) \rightarrow (uud) + e^- + \bar{\nu}_e \quad (38).$$

Similarly, the β^+ - decay of a bound proton to a neutron involves the transformation of u -quark to a d - quark

$$u \rightarrow d + e^+ + \nu_e \quad (39).$$

Diagrammatically the processes given by Eqs. (31, 32) are represented by diagrams such as those shown in Fig. 17.

Now QCD is known to be the theory of the strong interaction, classification of the strongly - interacting particles by their transformations properties under the flavor group $SU(3)$ (and the isospin subgroup $SU(2)$) follows naturally [45]. Of course, the flavor symmetries are only approximate (see e.g. [96]), as they are broken by the differences in the quark masses (see Table 9). The impact that these mass differences have on hadronic spectra and interactions is determined by how they compare to the scale of strong interactions. The $SU(2)$ symmetry for isospin is a very good symmetry of nature, being violated only at the percent level by both the electromagnetic interactions and the mass difference between the up and down quarks. The approximate $SU(3)$ symmetry is violated typically at the $\sim 30\%$ level due to the large mass difference between the strange quark and the up and down quarks as compared to the scale of the strong interaction ($\sim 1\text{GeV}$). Owing to QCD asymptotic-free nature (see [86 - 88] and references therein), perturbation theory can be applied at short distances; the resulting predictions have achieved a remarkable success, explaining a wide range of phenomena where large momentum transfers are involved. In the low - energy domain (see, for example Fig. 1 in Weise paper [96]), however the growing of the running QCD coupling and the associated confinement of quarks and gluons make very difficult to perform a thorough analysis of the QCD dynamics in terms of these fundamental degrees of freedom. A description in terms of the hadronic states seems more adequate; unfortunately, given the richness of the hadronic spectrum, this is also a formidable task.

At very low energies, a great simplification of the strong - interaction dynamics occurs. In this energy domain, this simplification allowed the development of a powerful theoretical framework, Chiral Perturbation Theory (ChPT) [96], to systematically analyze the low - energy implications of the QCD symmetries. This formalism is based on two key ingredients: the chiral symmetry properties of QCD and the concept of effective field theory (for details see [96]).

So, Yukawa's original paper [97] which then became the pion is still, more than seventy years after its first release, a generic starting point for our understanding of nuclear systems and interactions. Indications of ChPT so far are promising that this framework, constrained by the symmetry breaking pattern of low - energy QCD, can serve as foundation for a modern theory of the nucleus.

Thus, the gauge theory of the electroweak interaction has made it clear that the quark and lepton masses do not have the status of basic constant of nature: the masses of, say, the electron do not occur in the Lagrangian of the theory (for details see [95, 96]).

2.4. Isotope effect in nuclear physics.

In this paragraph we'll describe the influence of neutrons on the charge distribution. This influence has been studied using isotopic shift, the difference in the charge distributions of nuclei with the same number of protons but a

different number of neutrons. If charge distribution in a nucleus is independent of neutrons, we expect the isotopic difference to be negligible. The measured results (see, e.g. [98-100]) indicate that, in general, the shifts are small but nonzero. Isotope shift (of spectral lines) can be divided into two classes, that caused by the mass effect and that resulting from the field effect. The mass effect consists of two parts, normal and specific, and results from the nucleus having a finite mass. The normal mass effect can be calculated exactly, while the specific (for details see, also Chapter 3) mass effect present in spectra of atoms with more than one electron, is very difficult to calculate precisely. Both of these effects decrease with increasing Z . The field effect, which increases with increasing Z , arises because of the deviation of the nuclear electric field from a Coulomb field and can be used to study details of nuclear structure. This is probably the most important consequence of isotope shift studies.

In the very light elements the mass effect dominates and can account qualitatively for the observed shifts. In the heaviest elements the mass effect is negligible and the field effect can roughly account for the observed shift. In the element of intermediate mass the two effects are comparable. As a result, the shifts observed are small because the mass and field effects within the levels are often in such a direction as to oppose one another. In order to use the field effect in the demonstration of nuclear properties, it is necessary that the contribution of the mass and field effects to be observed shifts be known.

Isotope effect in calcium isotopes. The isotopic shift data [98], obtained from electron scattering are summarized in Table 11. As we can see, the difference in the root-mean-square radius $\langle r^2 \rangle^{1/2}$ between the isotopes given in Table 11 are quite small. However, the good accuracies achieved in the measured values indicate a genuine difference among them. Since the radius decreases by 0.01 fm in going from ^{40}Ca to ^{48}Ca , it means that the addition of neutrons to calcium isotopes reduces the size of the charge distribution of the same 20 protons when neutron number is increased from 20 to 28. If we take the simple view that charges were distributed eventually throughout the nuclear volume, the charge radius should have increased by 6% based on simple $R = r_0 A^{1/3}$ relation. This is found to be true in the case of ^{48}Ti [98], a nucleus with two more protons and six more neutrons than ^{40}Ca . Here, the size of the charge distribution is increased by 0.1 fm for ^{48}Ti not far from the expectation of an $A^{1/3}$ dependence, instead of decreasing for ^{48}Ca . There are two possible explanations for the decrease in the charge radius with increasing neutron number among even calcium isotopes. The first is that addition of neutrons makes the protons more tightly bound and, hence, the charge radius is smaller. This is, however, not true for nuclei in general (see, e.g. [8, 12]). A second explanation is based on the charge distribution within a neutron (see, Fig. 3). One possible model for the charge distribution in a neutron is that the central part is positive and the region near the surface is negative, as shown in Fig. 3. The detailed charge distribution is not well known, because of the difficulty in measuring the small charge for factor (see, also [99]). However, a small excess of negative charge in the surface region can produce about a third of decrease in the charge radius in

going from ^{40}Ca to ^{48}Ca , as suggested by the authors of paper [104]. The other two-thirds may be attributed to the spin dependence in interactions of protons with other nucleons in the nucleus (see, e.g. [63, 72]). Regardless of the exact cause of the isotopic shift among calcium isotopes, it is clear that neutrons have a definite influence on the measured charge distribution of a nucleus (for details see [98, 99]). The same effect can also be observed in other measurements, for example, such as the energy scattering of x-rays from muonic atoms [101-103].

Isotopic shift in muonic atoms. As was shown above, a muon is a lepton with properties very similar to an electron. For this reason, it is possible to replace one of the electrons on an atom by a (negative) muon to form a muonic atom. However, since the mass of a muon is 207 times larger than that of an electron, the radii of the muonic orbits are much smaller than those of electrons.

According to atomic physics (see, e.g. [101]) a hydrogen-like atom with Z protons in the nucleus and only a single electron outside, the radius of the n -th orbit is given by

$$r_n(e^-) = \frac{n^2 \hbar^2}{\alpha \hbar c Z m_e} \quad (40)$$

here, m_e is the mass of an electron, α is the fine structure constant. For a hydrogen atom ($Z = 1$), the ground state ($n = 1$) radius is the well-known Bohr radius (see, also [101]);

$$a_0 = \frac{\hbar^2}{\alpha m_e} = 5.29 \cdot 10^{-11} \text{m} \quad (41).$$

Using (40), we can obtain the analogous results for a muonic atom by replacing m_e by m_μ

$$r_n(\mu^-) = a_0 \frac{n^2 m_e}{Z m_\mu} \quad (42).$$

Using a muon mass $m_\mu = 106 \text{ MeV}/c^2$, we obtain for a heavy nucleus, such as ^{208}Pb ($Z = 82$) the radius of the lowest muonic orbit

$$r_1(\mu^-) \simeq 3.1 \cdot 10^{-15} \text{m} \quad (43)$$

or 3.1 fm. This is actually smaller than the value of 7.1 fm for the radius of ^{208}Pb , estimated using $R = r_0 A^{1/3}$ with $r_0 = 1.2 \text{ fm}$ [11]. A more elaborate calculation [102] shows that the muon spends most of its time inside a heavy nucleus. Being very close to the nuclear surface, the low-lying muonic orbits are sensitive to the detailed charge distribution of the different isotopes. The resulting changes in the energy levels may be observed as shifts in the position of lines. Detailed investigation of isotopic shift was done on the different isotopes of Fe in a paper by Shera et al. [102]. Muonic x-ray spectra from three isotopes of Fe obtained in this paper are shown in Fig. 18. The isotope shift is large compared with the isotope shift of electronic x-rays, which is typically 10^{-2} eV per unit change in A .

2.5. The origin of the mass.

As we well know, that in a nucleus the protons and neutrons, collectively known as nucleons, are bound together by the strong nuclear force. At a fundamental level these interactions are described by Quantum Chromodynamics (QCD), a theory of quarks and gluons carrying color charges that are asymptotically-free at short distances. However, the quarks and gluons in a

nucleus are very far from being asymptotically-free. Instead they comprise individual, colorless, nucleons, which largely retain their identity in the many-body system. The color-singlet nucleons are then bound to each other by what can be thought of as 'residual' QCD strong interactions. This sketch of nuclear dynamics from the QCD point of view - brief as it is - makes it clear that from this standpoint the nucleus is an incredibly complicated, nonperturbative, quantum-field-theoretic, infinite-body problem.

Understanding the nucleon mass and its dependence of light quark masses is clearly one of the most fundamental issues [40; 44; 94] in nuclear and particle physics (see, also [105-110]). A key question concerns the origin of the nucleon mass: how do almost massless u and d quarks and massless gluons cooperate dynamically to form a localized baryonic compound with a mass of almost 1 GeV? An equally fundamental issue is the origin of the nucleon spin: how is the total angular momentum of the nucleon in its rest frame distributed between its quarks and gluons and in turn between their spin and orbital angular momentum? We will not discuss the last question here further (for details, see e.g. [110-111]).

As we all know, almost all of the mass of the visible Universe is determined by the mass of the sum of the masses of nucleons in the cosmos. The gluonic energy density in the presence of three localized valence quarks obviously plays a decisive role in generating the nucleon mass [44, 108]. Basic QCD symmetries and the corresponding conserved currents as a guiding principle to construct effective Lagrangians which represent QCD at low energies and momenta. A rapidly advancing approach to deal with non-perturbative QCD is Lattice Gauge Field Theory (see, e.g. [96, 112]). Considerable progress is being made solving QCD on a discretised Euclidean space-time lattice using powerful computers (for details, see [109] and references therein). Lattice QCD has progressed to the joint that it can give reliable results concerning this issue, but with input quark masses still typically an order of magnitude larger than the actual current quark masses entering the QCD Lagrangian. Combining CHPT with lattice QCD has thus become a widely used routine in recent years (see, e.g. Fig. 1 in [109]).

For better understand the origin of the mass we should analyze the QCD condensates. In QCD by condensates there are called the vacuum mean values $\langle 0 | Q | 0 \rangle$ of the local (i.e. taken at a single point of space-time) of the operator $Q_i(x)$ which are due to non-perturbative effects. When determining vacuum condensates one implies the averaging only over non-perturbative fluctuations. If for some operator Q_i the non-zero vacuum mean value appears also in the perturbation theory, it should not be taken into account in determination of the condensate. In other words when determining condensates the perturbative vacuum mean values should be subtracted in calculation of the vacuum averages. As we know, the perturbation theory series in QCD are asymptotic series. So, vacuum mean operator values appear due to one or another summing of asymptotic series. The vacuum mean values of such kind are commonly to be referred to vacuum condensates [113]. The non-zero value of quark condensate means the transition of left-hand quark fields into right-hand ones and is not small value would mean to chiral symmetry violation in QCD. Quark condensate

may be considered as an order parameter in QCD corresponding to spontaneous violation of the chiral symmetry [96, 112].

For quark condensate $\langle 0 | \bar{q}q | 0 \rangle$ ($q = u, d$ are the fields of u and d quarks) there holds the Gell-Mann-Oakes-Renner (GMOR) relation [114]

$$\langle 0 | \bar{q}q | 0 \rangle = -\frac{1}{2} \frac{m_\pi^2 f_\pi^2}{m_u + m_d} \quad (44).$$

Here m_π, f_π are the mass and constant of π^+ - meson decay ($m_\pi = 140$ MeV, $f_\pi = 92 - 131$ MeV for different authors), m_u and m_d are the masses of u - and d - quarks. Relation (44) is obtained in the first order of m_u, m_d, m_s (for its derivation see, e.g. [44]). To estimate the value of quark condensate one may use the values of quark masses $m_u + m_d = 13$ MeV [115]. Substituting these values into (44) we get for quark condensate

$$\langle 0 | \bar{q}q | 0 \rangle = - (0.23 \text{ GeV})^3 \simeq - 1.6 \text{ fm}^{-3} \quad (45).$$

This condensate is a measure, as note above, of spontaneous chiral symmetry breaking. The non-zero pion mass, on the other hand, reflects the explicit symmetry breaking by the small quark masses, with $m_\pi^2 \sim m_q$. It is important to note that m_q and $\langle 0 | \bar{q}q | 0 \rangle$ are both scale dependent quantities. Only their product $m_q \langle 0 | \bar{q}q | 0 \rangle$ is scale independent, i.e. invariant under the renormalization group.

The appearance of the mass gap $\Gamma \sim 1$ GeV in the hadron spectrum is thought to be closely linked to the presence of chiral condensate $\langle 0 | \bar{q}q | 0 \rangle$ in the QCD ground state. Ioffe formula [116], based on QCD sum rules, connects the nucleon mass M_N directly with quark condensate in leading order

$$M_N = - \left[\frac{8\pi^2}{\Lambda_B^2} \langle 0 | \bar{q}q | 0 \rangle \right]^{1/3} + \dots \quad (46),$$

where $\Delta_B \sim 1$ GeV is an auxiliary scale (the Borel mass [109]) which separates "short" and "long" distance in the QCD sum rule analysis. While Ioffe's formula needs to be improved by including condensates of higher dimensions, it nevertheless demonstrates the close connection between dynamical mass generation and spontaneous chiral symmetry breaking in QCD. Taking into account the value of quark condensate from Eq. (45) we get for M_N

$$M_N = 986.4 \text{ MeV} \quad (47).$$

The obtained value of M_N differs from experimental meaning of $M_N = 940$ MeV on the 5%. For nuclear physics, Eqs. (46-47) give important hint: the change of the quark condensate with increasing baryon density implies a significant reduction of the nucleon mass in the nuclear medium.

In the chiral effective theory, the quark mass dependence of M_N translates into dependence on the pion mass at leading order. The systematic chiral expansion [96] of the nucleon mass gives an expression of the form

$$M_N = M_0 + cm_\pi^2 + dm_\pi^4 - \frac{3\pi}{2} g_A^2 m_\pi \left(\frac{m_\pi}{4\pi f_\pi} \right)^2 \left(1 - \frac{m_\pi^2}{8M_0^2} \right) + \dots \quad (48),$$

where the coefficients c and d multiplying even powers of the pion mass include low-energy constants constrained by pion - nucleon scattering. Note, that the coefficient d also involves a $\log m_\pi$ term.

In conclusion of this paragraph we should note, that the fact m_d is larger than m_u by a few MeV implies, that the neutron is heavier than the proton by a few MeV. As is well-known, the experimental neutron-proton mass difference of $M_n -$

$M_p = 1.2933317 \pm 0.0000005$ MeV [60, 79] receives an estimated electromagnetic contribution of [105] $M_n - M_p |^{em} = -0.76 \pm 0.30$ MeV and the remaining mass difference is due to a strong isospin breaking contribution $M_n - M_p |^{d-u} = 2.05 \pm 0.30$ MeV. Recently Bean et al. [110] have performed the first lattice calculation of the neutron-proton mass difference arising from the difference between the mass of the up and down quarks (see, also [95] and find $M_n - M_p |^{d-u} = 2.26 \pm 0.57$ MeV. This value is in good agreement with the experimental result quoted above. Concluding we should note, that we do not know why the observed mass pattern (M_n , M_p , m_u , m_d etc.) looks like this, but nuclear physics can analyze the consequence of this empirical fact.

2.6. New physics beyond the Standard Model.

A major challenge for physics today is to find the fundamental theory beyond the Standard Model [45] (the "Theory of everything"). In a nutshell, the Standard Model (SM) is a unified gauge theory of the strong, weak and electromagnetic interactions, the content which is summarized by the group theory

$$SU(3)_C \times SU(2)_L \times U(1)_Y \quad (49),$$

where the first factor refers to the theory of strong interactions, or Quantum Chromodynamics (QCD) [96, 108], and the latter two factors describe the theory of electroweak interactions (see, also [39, 45, 85, 117, 118, 119, 120, 121]). However, we have the difficulty that the vast majority of the available experimental information, at least in principle [118 - 121], explained by the SM. Also, until now, there has been no convincing evidence for existence of any particles other than those of the SM and states composed of SM particles. All accelerator physics seems to fit well with the SM, except for neutrino oscillations [39]. Apart from neutrino masses and mixing angles the only phenomenological evidence for going beyond the SM comes from cosmology and astrophysics [122]. It is well-known that the pure SM predicts a too low value for the baryon number resulting from the Big Bang [1]. Apart from these astrophysical problems, there is only very weak experimental evidence for effects which do not match the SM extended to include neutrino mass as well as hierarchy of elementary particles mass etc. From these standpoints, the SM has been an enormously successful theory. Nevertheless, there exist many reasons for believing that the SM is not the end of the story. Perhaps the most obvious is the number of independent parameters that must be put in by hand. For example, the minimal version of the SM has 21 free parameters, assuming massless neutrinos and not accounting electric charge assignments [45]. Most physicists believe that this is just too much for the fundamental theory. The complications of the SM can also be described in terms of a number of problems, which we list briefly below.

1. Coupling Unification.

There exists a strongly held belief among particle physicists and cosmologists that in the first moments of the life of the Universe, all forces of nature were "unified", that is they all fit into a single gauge group structure whose interaction strengths were described by a single coupling parameter, g_u (see, Fig. 2. in

[40]). As we can see from this Fig., that the three SM coupling almost meet at a common point around $3 \cdot 10^{16}$ GeV.

2. The Hierarchy Problem.

As we know, all matter under ordinary terrestrial conditions can be constructed out of the fermions (ν_e , e^- , u , d) of the first family (see Table 9). Yet we know also from laboratory studies that there are two families (ν_μ , μ^- , c , s) and (ν_τ , τ^- , t , b) are heavier copies of the first family with no obvious role in nature. The SM gives no explanation for the existence of these heavy families. Further more, there is no explanation or prediction of the fermion masses, which over at least five orders of magnitude:

$$m_{W,Z} \sim m_{top} \gg m_b \gg m_\tau \gg m_e \gg m_\nu \quad (50).$$

How does one explain this hierarchy of masses? The SM gives us no clue as to how to explain the hierarchy problem.. Really, the problem is just too complicated. Simple grand unified theory (GUT) don't help very much with this (for details see e.g. [45] and references therein). We should repeat that the non-vanishing neutrino masses and mixings are direct evidence for new physics beyond the SM.

3. Discrete Symmetry Violation.

By construction, the SM is maximally parity-violating, it was built to account for observations that weak c.c. processes involve left-handed particles (or right-handed antiparticles). But why this mismatch between right-handedness and left-handedness? Again no deeper reason for the violation of parity is apparent from the SM. It would be desirable to have answer to this question, but it will take some new framework to provide them.

4. Baryon Asymmetry of the Universe.

Why do we observe more matter than anti-matter? This is problem for both cosmology and the SM.

5. Graviton Problem.

Gravity is not fundamentally unified with other interactions in the SM, although it is possible to graft on classical general relativity by hand. However, this is not a quantum theory, and there is no obvious way to generate one within the SM context. In addition to the fact that gravity is not unified and not quantized there is another difficulty, namely the cosmological constant (for details, see [122] and references therein). The cosmological constant can be thought of as energy of the vacuum. The energy density induced by spontaneous symmetry breaking is some ~ 120 orders of magnitude larger than the observational upper limit. This implies the necessity of severe fine-tuning between the generated and bare pieces, which do not have any a priori reason to be related (see, also [123]).

6. Quantization of Electric Charge.

The SM does not motivate electromagnetic charge quantization (for example, for quarks), but simply takes it as an input. The deeper origin of charge quantization is not apparent from the SM.

To summarize, despite the triumphant success of the SM, there exist conceptual motivations for believing that there is something more, that the high energy desert is not so barren after all.

3. Isotopes in atomic and molecular physics.

3.1. Some general remarks.

The interpretation of atomic isotope shifts relies partly on the knowledge of nuclear structure. Conversely it can provide some information on the structure nuclei. This relation between the two fields has been for many years the main reason for the interest in isotope shifts of optical (electronic) transitions (see, e.g. reviews and monographs [19, 21, 22, 62, 99, 124, 125, 126]).

The word "atom" introduced by Democritus more than 2400 years ago in Greek means "inseparable". Atomism as understood by modern science was first discovered for matter, then for electricity and finally for energies. The atomism of matter, the recognition of the fact that all the chemical elements are composed of atoms, followed from chemical investigations. Only whole atoms react with one another. The first atomic model (at the beginning of 19 century) assumed that the atoms of all elements are put together out of hydrogen atoms. As a heuristic principle this hypothesis finally led to a scheme for ordering the elements based on their chemical properties, the periodic system of D.I. Mendeleev. More about this subject may be found in introductory textbooks on chemistry [127]. Continuous investigations of gases in the course of the 19 century led to the atomism of heat, that is, to the explanation of heat in general and of the thermodynamic laws in particular as consequences of atomic motion and collisions. The atomism of electricity was discovered in 19 century by the English scientist M. Faraday. Based on the quantitative evaluation of exceedingly careful measurements of the electrolysis of liquid, M. Faraday concluded "There are "atoms" of electricity". These "atoms" of electricity - the electrons are bound to atoms in matter.

The discovery of the atomism of energy can be dated exactly: on December 14, 1900 (see, e.g. [128]) M. Planck announced the derivation of his laws for black body radiation in a lecture before the Physical Society in Berlin. In order to derive these laws, M. Planck assumed that the energy of harmonic oscillators can only take on discrete values - quite contradictory to the classical view, in which the energy values form a continuum. This date can be called the birth date of quantum theory [49].

Our knowledge of the structure of atoms was influenced strongly by the investigation of optical spectra [129, 130]. The most important sources of information about the electronic structure and composition of atoms are spectra in the visible, infrared (IR), ultraviolet (UV) frequency ranges [101]. Optical spectra are further categorized as line, band and continuous spectra [129]. Continuous spectra are emitted by radiant solids or high - density gases. Band spectra consist of groups of large numbers of spectral lines which are very close to one another. They are generally associated with molecules [23 - 25]. Line spectra, on the other hand, are typical of atoms (see, also [20 - 22]). They consist of single lines, which can be ordered in characteristic series.

The founders of spectroscopic analysis, Kirchhoff and Bunsen, were the first to discover in the mid - 19th century that each element possesses its own characteristic spectrum. Hydrogen is the lightest element, and the hydrogen atom

is the simplest atom, consisting of a proton and an electron. The spectra of hydrogen atom have played an important role again and again over the last (20th) century in the development of our understanding of the laws of atomic structure and the structure of matter.

The emission spectrum of atomic hydrogen (Fig. 19) shows three characteristic lines in the visible region at 6563, 4861 and 4340 Å (H_α , H_β , H_γ , respectively). As we can see from Fig. 19, the most intense of these lines was discovered in 1853 by Angström; it is now called the H_α line. In the near UV region, these three lines are followed by a whole series of further lines, which fall closer together in a regular way as they approach a short - wavelength limit (H_∞). During this period empirical regularities in line spectra were being found. The best known of these was Balmer's simple formula (1885) for the wavelengths of the visible lines of the hydrogen spectrum. For the wavenumbers ($\nu = 1/\lambda$) of the lines we write the Balmer formula

$$\nu = R_H \left(\frac{1}{2^2} - \frac{1}{n^2} \right) \quad (51),$$

where n - integer and equals $n = 3, 4, 5, \dots$. The quantity R_H is called the Rydberg constant and has the numerical value $R_H = 109677.581 \text{ cm}^{-1}$ [101]. The series limit is found for $n \rightarrow \infty$ to be $\nu = R_H/4$. This empirical discoveries of spectral regularities reach their culmination in the clear establishment of the Ritz combination principle. This came in 1898 after a decade of important work on the study of spectral series [130]. According to this result each atom may be characterized by a set of numbers called terms ($R_H/4$), dimensionally like wavenumbers, such that the actual wavenumbers of the spectral lines are given by the differences between these terms. A comparison of the calculated obtained from the Balmer formula (Eq. (51)) with the observed lines [130] shows that the formula is not just a good approximation: the series is described with great precision. The combination principle suggests the existence of lines given more generally by

$$\nu = R_H \left(\frac{1}{m^2} - \frac{1}{n^2} \right) \quad (52),$$

where $m < n$ being integer. The numbers m and n are called principal quantum numbers. For $m = 3$ and $n = 4, 5, 6, \dots$ the lines fall in the IR. Paschen found them at the predicted places. Lyman also found in the UV three lines corresponding to $m = 1$ and $n = 2, 3, 4, \dots$. Table 12 contains some of the lines from the first four series and thus illustrates the Ritz Combination Principle. As we can see, the difference of the frequencies of two lines in a spectral series is equal to the frequency of a spectral line which actually occurs in another series from the same atomic spectrum. For example, the frequency difference of the first two terms in the Lyman series is equal to the frequency of the first line of the Balmer series. To concluding this paragraph we should repeat that the frequencies (or wavenumbers) of all spectral lines can be represented as differences of two terms of form R/n^2 . These are just the energy levels of the electron in a hydrogen atom. The model of the hydrogen atom consisted of an electron and proton describing orbits about their centre of mass according to classical mechanics under their mutual attraction as given by the Coulomb inverse - square law. The allowed circular orbits were determined simply by the requirement (an additional postulate of quantum theory [49]) that the angular

momentum of the system be an integral multiple of $\hbar = h/2\pi$. This condition yields an equation from which R_∞ can be calculated (for details see [101])

$$R_\infty = \frac{m_0 e^4}{8\varepsilon_0^2 \hbar^3 c}. \quad (53)$$

From (53) we can find for the Rydberg constant R_∞ the numerical value

$$R_\infty = (109737.318 \pm 0.012) \text{cm}^{-1}. \quad (54)$$

This may be compared with empirical value in (51). In hydrogen model R is just the ionization energy of the ground state of the atom with $n = 1$. Next part of our review gives an account of what can be understood in experimental isotope shifts before (or without) separating the two types of contributions (mass - and field - shift), in other words, the way in which the isotopes shift changes from one level to the other in a given spectrum. As will be shown below the latter problem is purely problem of atomic structure.

3.2. Motion of the nucleus - atomic isotope shift.

The spectroscopically measured quantity R_H (see paragraph 3.1) does not agree exactly with the theoretical quantity R_∞ (see [54]). The difference is about 60 cm^{-1} [130]. The reason for this is the motion of the nucleus during revolution of the electron, which was neglected in the above model calculation. As we remember, this calculation was made on the basis of an infinitely massive nucleus. Now we must take the finite mass of nucleus into account [129].

As we know from classical mechanics, the motion of two particles, of masses m and M and at distance r from one another, takes place around the common centre of gravity. If the centre of gravity is at rest, the total energy of both particles is that of a fictitious particle which orbits about the centre of gravity at a distance r and has the mass

$$\frac{1}{\mu} = \frac{1}{m} + \frac{1}{M}; \quad \mu = \frac{mM}{m+M}, \quad (55)$$

referred to as the reduced mass. Replace the mass of the orbiting electron, m_0 by μ and obtain, in agreement with experiment

$$R = R_\infty \left(\frac{1}{1 + m/M} \right). \quad (56)$$

Here $m = m_0$ - the mass of the orbiting electron, and M , the mass of the nucleus. The energy corrections due to motion of the nucleus decrease rapidly with increasing nuclear mass (see Table 13). This observation makes possible a spectroscopic determination of the mass ratio M/m_0

$$M_{\text{proton}}/m_{\text{electron}} = 1836.15 \quad (57)$$

Due to the motion of the nucleus, different isotopes of the same element have slightly different the frequency of spectral line. This so - called isotope displacement led to the discovery of heavy hydrogen with the mass number $A = 2$ (deuterium). It was found that each line in the spectrum of hydrogen was actually double. The intensity of the second line of each pair was proportional to the content of deuterium [19, 131]. Fig. 20 shows the H_β line with the accompanying D_β at a distance of about 1 \AA in a 1;1 mixture of the two gases. The nucleus of deuterium contains a neutron in addition to the proton. There are easily measurable differences in the corresponding lines of the H and D Lyman series:

$$R_H = 109677.584 \text{ cm}^{-1}; \quad R_D = 109707.419 \text{ cm}^{-1} \quad (58).$$

The more precisely the differences in hydrogen - deuterium 1s - 2s isotope shift was done recently by Huber et al. [132]. These authors exceeds the accuracy of earlier experiment by more than 2 orders of magnitude. Fig. 21 shows the frequency chain that has been described in part in [133], where an absolute measurement of the 1s - 2s frequency has been reported. Authors [132, 133] determine the isotope shift by fitting a pair of parallel lines to the hydrogen and deuterium data, thus accounting for a linear frequency drift of the standard. After averaging of 10 measurements line the one shown in Fig. 22, these authors obtained the experimental result for the 1s - 2s H - D isotope shift

$$\Delta f_{\text{exp}} = 670994334.64 (15) \text{ kHz} \quad (59).$$

The uncertainty of 150 kHz is dominated by the frequency fluctuations of the CH₄ - stabilized He - Ne standard. At the precision level the theoretical contributions to the isotope shift must be reanalyzed. Most of the H - D isotope shift of the 1s - 2s interval is caused by the different masses of the nuclei (for details see, also [132]).

3.3. Separation of mass- and field-shift contributions.

Before the early sixties, for scientists interested in atomic isotope shift, the Periodic Table was implicitly divided into three regions (see, e.g. [19,22]):

- 1) the light elements, with approximately $Z \leq 30$, where mass isotope shift only was considered to be present;
- 2) the heavy elements ($Z \geq 58$), with field isotope shift only, and;
- 3) between these two regions, namely, beyond the 3d series and before the 4f series, medium - weight elements with small isotope shifts, difficult to measure accurately.

Thus mass - and field - shift effects were considered almost independently. For mass - shift effects, the paper by Vinti [134] was a reference: it essentially indicates the formal way in which the mass isotope shift changes from one pure Russel - Saunders (RS) term to another [129]. For field isotope shift, the basic papers were by Rosenthal and Breit [135] and Racah [136], both of which considered the case of multielectronic atom: in the case of multielectronic spectra, the field - shift was considered inside a given configuration, and the way it changes from one configuration to another was described through the use of "screening factor" introduced by authors of paper [137].

So, the isotope shift of an optical transition is the sum of two terms: the mass effect and the field effect. If only one isotope pair is available, the experiment only yields this sum but not the respective contributions of the two effects. The situation is then much less favorable than for hyperfine structure (see, e.g. [20, 21]), because, in this latter case, the Casimir formula allows a separation of the magnetic - dipole and electric - quadrupole contributions [138]. Unfortunately, if the mass effect and field effect contributions cannot be separated, the theoretical interpretations of experimental result necessary remain rather crude (compare [139]).

3.3.1. Mass isotope shift.

The theory for a nucleus of finite mass in an N - electrons has been considered for the first time by Hughes and Eckart [140]. The correction to the atomic energy levels due to the nuclear mass motion is given in the non - relativistic limit by the kinetic energy of the nucleus due to its motion about the centre of mass of the atom [129]

$$\Delta E = \frac{1}{2M} \left(\sum_i \vec{p}_i^2 + \sum_{i \neq j} \vec{p}_i \cdot \vec{p}_j \right) \quad (60)$$

Here M is the nuclear mass and \vec{p}_i - the momentum of the i -th electron. The sum is over all the electrons in the atom. The effect of the square terms on the total energy can be evaluated exactly by taking them together with the corresponding kinetic energy terms of the electrons, giving the well - known reduced mass correction (see Eq. (55)). The consequent term and line shifts can be simply calculated, and are referred to as "normal mass shifts" (NMS) [19]. It is usually it will be assumed that the normal effect has been allowed for in all shifts discussed (see, e.g. [62]). Shifts arising from the second term are called "specific mass shifts" (SMS) [140]. The term contains cross products of the momenta of different electrons and is not susceptible of exact calculation, though in light elements results in moderate agreement with experiment have been obtained [19, 22]. For the heavier elements, many electrons are involved and the calculations become rapidly more complex [125]; no simple rules appear to exist which would allow even the crudest estimates of SMS for such elements. Generally, therefore plausibility arguments or semi - empirical methods are used (see, also [22]).

In the region of the medium - heavy elements, semi - empirical methods for SMS have been applied, though it appears that such allowance should often be made also in heavier elements [125]. The total observed shift can be written

$$\Delta E_{total} = \Delta E_{NMS} + \Delta E_{SMS} + \Delta E_{FS}, \quad (61)$$

where the values of ΔE apply to the differences in the upper and lower levels involved in a transitions, i.e. they refer to line shifts. From (61), a relation between the mass shifts in different lines of an element may be obtained. We use the symbol m for the SMS in a line on the addition of one neutron and put $\Delta E_{total} - \Delta E_{NMS} = T$. Then the values of T between two isotopes with neutron numbers N and N' for two spectral lines (suffixes 1 and 2) are given by

$$\begin{aligned} T_1^{N,N'} &= (N' - N)m_1 + F_1 C^{N,N'}; \\ T_2^{N,N'} &= (N' - N)m_2 + F_2 C^{N,N'}. \end{aligned} \quad (62)$$

Here F ; C are positive constant and functions of size and shape of the nucleus [62]. In the last equations it was assumed that m for a heavy elements independent of N . We should not, that the slight dependence can, of course, be taken into account, but (62) is sufficiently accurate for most purposes [125]. The superscript N,N ; denotes dependence on these quantities, the Z dependence has been omitted to make the formulae less cumbersome, since the argument concerns only one element. From (62) we have

$$T_1^{N,N'} = T_2^{N,N'} \frac{F_1}{F_2} + (N' - N)(m_1 - m_2 \frac{F_1}{F_2}). \quad (63)$$

Thus, if two or more corresponding shifts are measured in each of two lines of an element, F_1/F_2 can be found and also $(N' - N)(m_1 - m_2 \frac{F_1}{F_2})$. King [22] suggested simply plotting the shifts in one line against the corresponding shifts in another, first dividing each shift by $(N' - N)$. Then the points should lie on a straight line (see, for example Figs. 2 - 3 in [125]), and the slope and intercept are F_1/F_2 and $(m_1 - m_2 \frac{F_1}{F_2})$ respectively. Whatever the number of lines for which results are available, it is, of course, impossible by this method to determine any of the mass shift uniquely, however, plausibility arguments based on the nature of the specific mass effect can be used to make estimates, and the greater the number of lines for which the total shifts are known, the more restricted becomes the range of reasonable values of the contributions of the specific shifts. Further, as King [22] pointed out, if the mass shift could be computed for one line, the procedure described enables it to be found for the others from the experimental results [125].

3.3.2. Field isotope shift.

In optical and electronic x - ray transitions the field shift is very nearly proportional^{8*)} $\langle r^2 \rangle^{1/2}$ and it is convenient to express this in terms of a "standard shift" based on an equivalent uniform charge density of radius $R_{eq} = r_0 A^{1/3}$ fm. This standard unit of isotope shift does not have a fundamental significance but does represent approximately the overall variation of R_{eq} for stable nuclei. Because a change in neutron number is either a move towards or away from the region of stability there is no reason to expect isotope shifts to be the same as the standard shift and in fact they are usually smaller [62].

8*) The standard shift calculated on the basis of $\langle r^2 \rangle^{1/2}$ dependence can be corrected by dividing by the quantity $[1 + 1.2 \cdot 10^{-5} Z^2]$. This correction takes into account the effect of $\langle r^4 \rangle$ and $\langle r^6 \rangle$ terms and is based on the results of Seltzer [141].

a) isotope shift in optical spectra. The nuclear electrostatic potential acting on the electron depends on the nuclear charge distribution; if this changes from one isotope to another, the energy of an electron which penetrates the nucleus will also change in the two cases. In the early works [135, 136], spherically symmetrical nuclear charge distributions of simple form were assumed, and the values E_{field} and ΔE_{field} were calculated by perturbation treatment, recognized and allowed for to some extent the results of [135], led to evaluation of ΔE_{field} by more rigorous methods (see, also [19]). The foundation for this latter work were laid by author of paper [142]. He considered the solutions to the radial Dirac equation for the electron: 1) with the nuclear charge assumed concentrated at a point, and 2) with extended nuclear charge distribution (for details see [130]). The modern description of the field isotope shift have the next form:

$$\Delta E_{field}^{N,N'} = F_i \lambda^{N,N'} \quad (64)$$

$$\lambda^{N,N'} = \delta \langle r^2 \rangle^{N,N'} + \frac{C_2}{C_1} \delta \langle r^4 \rangle^{N,N'} + \frac{C_3}{C_1} \delta \langle r^6 \rangle^{N,N'} + \dots \quad (65)$$

λ is the nuclear parameter [99] and $F_i = E_i f(z)$ - electronic factor. Values of $f(z)$ calculated from the isotope shift constants are given in Table II of [99]. The ratios C_n/C_1 have been calculated by Seltzer [141]. The procedure of the evaluation of λ was as follows[99]: first the SMS were estimated, either according above formula or from King plots [22] of the optical isotope versus results from muonic isotope shifts [143] or electronic x - ray shifts [19, 124, 125].

b) x - ray isotope shift. As was shown above, atomic isotope shifts are measured in both optical and x - ray spectra (see Fig. 18). Since the Coulomb potential at the nucleus is so much larger than the binding energy, the s - wave function is largely independent of the principal quantum number. For instance, as was shown by Seltzer [141], the change in C_2/C_1 (Eq.(65)) is going from 1s to 2s amounts to only a few tenths of percent. Beyond the 2s level, there is very little further change. C_2/C_1 for a $p_{1/2}$ level is within a few percent of C_2/C_1 for a $s_{1/2}$ level (4% for $Z = 80$ [141]). This means that both atomic optical and x - ray isotope shifts measure the same parameter λ . Moreover, the largest contributions in heavy atoms to the energy shift observed on going from one isotope to another comes from the modification of the nuclear charge distribution. The total mass shift for K x - ray transitions is usually less than a few percent of the total isotope shift [144]. The SMS for optical transitions in heavy atoms is usually neglected. Unlike the x - ray case, the SMS in optical transitions can be a large part of the total isotope shift. (for details see [144]).

3.4. Vibrations in a diatomic molecule.

Since a diatomic molecule has two atoms and must be linear, it has one degree of vibrational freedom. By convention the z - axis is placed coincident with the molecular axis. Movement of the atoms in the x - and y - directions can then be dismissed as molecule rotations. Let us choose a diatomic molecule AB whose atoms have mass m_A (coordinate z_A) and m_B (z_B). Moreover, let us now suppose that the atoms are like metal balls and the bond between them is like a simple spiral spring. If we then allow the distance between A and B to change by a quantity $q = (z'_A - z'_B) - (z_A - z_B)$, while keeping the centre of mass at the origin of axes, we could say that the force (F) exerted by the spring on the particles is related to q by (see, e.g. [26])

$$F = fq \quad (66).$$

This is to say the spring obeys Hook's law (linear approximation), and we shall see that this analogy is a good one. The force exerted by the spring will cause the atoms to return to their original positions. If we denote the velocity with which do so by dq/dt and the acceleration d^2q/dt^2 we may apply Newton's second law of motion and equate the force with mass times an acceleration. At this point we shall write the reduced mass M ($M = \frac{m_A m_B}{m_A + m_B}$)

$$-fq = M \frac{d^2q}{dt^2}. \quad (67)$$

This is a second order differential equation which may be solved by making the substitution

$$q = A \cos(2\pi\nu t + \rho), \quad (68)$$

where ν is a frequency, ρ is a phase factor and A - a maximum vibration amplitude. Then we have

$$\frac{d^2q}{dt^2} = -4A\pi^2\nu^2 \cos(2\pi\nu t + \rho) = -4\pi^2\nu^2 q. \quad (69).$$

Substituting this back into Equation (67) we obtain

$$(-4\pi^2\nu^2 M + f)q = 0 \quad (70)$$

and assuming $q \neq 0$, we have

$$\nu = \frac{1}{2\pi} \sqrt{\frac{f}{M}} \quad (71)$$

This equation is the equations of simple harmonic oscillators.

In the last equation (71) f is proportionality constant. This proportionality constant is known as a force constant. It could be defined in terms of Hook's law (Eq. (66)), but this is not convenient. Alternatively it may be defined in terms of the vibrational potential energy [23]. Before considering the quantum mechanics of the vibrations in a diatomic molecule, we must first discuss two assumptions that are implicit in the treatment so far: that classical mechanics provides an adequate description of a vibrating molecule, and that Hook's law is valid. The term molecular coordinate is one which we shall meet below in various form. Unlike the Cartesian coordinates a molecular coordinate does not define the position of the atoms absolutely, but defines the change in coordinates from some initial position. Thus, q defined the change in bond length in the diatomic molecule, but did not define the actual bond length. The term coordinate will be understood to define some change in the molecular configuration. the origin of this coordinate system is given by the average or equilibrium position of the atoms in the molecule, ignoring translation and rotation (for details see, e.g. [25]).

Perhaps the most surprising thing about molecular vibrations is that the frequencies of vibration may be correctly calculated by means of classical mechanics. Intuitively one feels that this is due to the wave nature of the vibrations. However, quantum mechanics does provide greater insight into aspect other than the frequencies. To simplify our discussion we will only consider the simplest case, the harmonic oscillator (see, also [145]).

The wave equation for a one - dimensional oscillator such as a diatomic molecule is [146]

$$\frac{d^2\Psi}{dq^2} + \frac{8\pi^2M}{h^2} (E - V)\Psi = 0, \quad (72)$$

where E is the total vibration energy. In the harmonic oscillator the potential energy V is given as $\frac{1}{2}fq^2$ and the wave equation becomes

$$\frac{d^2\Psi}{dq^2} + \frac{8\pi^2M}{h^2} (E - \frac{1}{2}fq^2)\Psi = 0. \quad (73)$$

The solution of this equation are given in most texts on quantum mechanics (see, e.g [49]). Thus the energy E is given as

$$E = (n + \frac{1}{2}) \frac{h}{2\pi} \sqrt{\frac{f}{M}}, \quad (74)$$

where n is a quantum number that may take the values 0, 1, 2, 3, Therefore when the molecule changes from one vibrational state to the next nearest by one the change in energy is given by

$$\Delta E = \frac{h}{2\pi} \sqrt{\frac{f}{M}}, \quad (75)$$

and since $\Delta E = h\nu$, the frequency of a photon associated with this change is

$$\nu = \frac{1}{2\pi} \sqrt{\frac{f}{M}}, \quad (76)$$

which is the same result as given by classical mechanics. It can then be shown that in the general case classical and quantum mechanics give the same answer for the vibration frequencies; hence we are fully justified in using classical mechanics to calculate them (see, also [24]). If $n = 0$ in equation (74) the molecule has an energy of $\frac{h}{4\pi} \sqrt{\frac{f}{M}}$. This energy is known as the zero point energy and has no counterpart in classical mechanics [49].

For a diatomic molecule we may expand the vibrational potential energy as a Maclaurin series about the position of minimum energy, V_0 [147,148]

$$V = V_0 + \left(\frac{dV}{dq}\right)_0 q + \frac{1}{2} \left(\frac{d^2V}{dq^2}\right)_0 q^2 + \frac{1}{6} \left(\frac{d^3V}{dq^3}\right)_0 q^3 + \frac{1}{24} \left(\frac{d^4V}{dq^4}\right)_0 q^4 + \dots \quad (77)$$

The subscript zero indicates the position of minimum potential energy, so that $\left(\frac{dV}{dq}\right)_0 = 0$. The quantity V_0 is a constant independent of q and may be ignored since it does not affect the vibrational frequencies. We have already met the force constant definition $f = \frac{d^2V}{dq^2}$, so we may rewrite the potential energy as

$$V = \frac{1}{2} f q^2 + \frac{1}{6} \left(\frac{d^3V}{dq^3}\right)_0 q^3 + \frac{1}{24} \left(\frac{d^4V}{dq^4}\right)_0 q^4 + \dots \quad (78)$$

The calculations in the previous text were based on the approximation that the terms in power of q higher than two may be ignored. Of course the true potential energy of a molecule must be more complex, if only because for large values of q the molecules must dissociate. Fig 23 shows scheme of the potential energy of typical diatomic molecule as a function of q , while the dotted line is the parabola calculated for $V = \frac{1}{2} f q^2$. The true curve is steeper than the parabola at small internuclear distances, because of the interatomic repulsion energy but at large internuclear distance the true potential energy tends asymptotically to a constant value, the dissociation energy Q . Near the equilibrium internuclear separation ($q = 0$) the parabola is quite a good approximation to the potential energy. For this reason, the approximation $V = \frac{1}{2} f q^2$ is quite good. Taking $V = \frac{1}{2} f q^2$ is known as the harmonic approximation [24], and the potential energy is said to be quadratic. The force constant f defined as $\frac{d^2V}{dq^2}$ is said to be quadratic force constant. The addition of the cubic term in Eq. (77) gives a better fit with the true potential energy curve at the minimum and may be used in accurate work. However, the equations of motion obtained by using a cubic term in potential energy are not easy to handle.

One approximate solution to the Schrödinger equation that may be found expresses the energy in terms of the harmonic frequency ν_e and an anharmonic constant x_e , thus (see, e.g [148])

$$E = h\nu_e \left(n + \frac{1}{2}\right) - h\nu_e x_e \left(n + \frac{1}{2}\right)^2 \quad (79)$$

Therefore if two transitions corresponding, to $\Delta n = 1$ and $\Delta n = 2$, can be observed both ν_e and x_e may be calculated. The quantity ν_e may be regarded as the frequency the molecule would have if it was a harmonic oscillator, so that x_e supplies a means of adjusting the observed frequency. In practice, then, the observed frequencies are adjusted to give the harmonic frequencies and the

theory of the harmonic oscillator is then applied [23, 147]. It is conventional to express harmonic frequencies cm^{-1} , and to give them the symbol ω_e , where $\omega_e = \nu_e/c$ and c is the velocity of light. Anharmonic affects molecular vibrations in two important ways [24]. Firstly, the selection rule (see, also below) derived for the harmonic oscillator, $\Delta n = \pm 1$, ceases to be a rigorous selection rule, and transitions with, for example, $\Delta n = \pm 2$ become allowed. Secondly, the vibrational energy levels are not spaced apart equally by the quantity $h\nu$. Thus, not only may it be possible to observe a transitions with $\Delta n = \pm 2$, but this transitions will not have exactly double the frequency of the transition for which $\Delta n = \pm 1$ (see, e.g. Fig. 48 in [24]).

3.4.1. Raman and IR spectra of molecules.

Vibrational spectroscopy involves the use of light to probe the vibrational behavior of molecular systems, usually via an absorption and light scattering experiment. When light interacts with matter, the photons which make up the light may be absorbed or scattered, or may not interact with the material and may pass straight through it. If the energy of an incident photon corresponds to the energy gap between the ground state of a molecule and an excited state, the photon may be absorbed and the molecule promoted to the higher energy excited state. It is this change which is measured in absorption spectroscopy by the detection of the loss of that energy of radiation from the light. however, it is also possible for the photon to interact with the molecule and scatter from it. In this case there is no need for the photon to have an energy which matches the difference between two energy levels of the molecule. The scattered photons can be observed by collecting light at an angle to the incident light beam, and provided there is no absorption from any electronic transitions which we have similar energies to that of the incident light. This process is called the process of Raman scattering.

Fig. 24 illustrates one key difference between IR and Raman scattering. As described above< IR absorption would involve direct excitation of the molecule from state m to state n by a photon of exactly the energy difference between them. In contrast< Raman scattering uses much higher energy radiation and measures the difference in energy between n and m by subtracting the energy of the scattered photon from that of the beam.

Before it will demonstrate IR and Raman spectra of some molecules, we should say about selection rule for these processes. As we all know, a triatomic molecule will have three modes of vibrations. They are symmetrical stretch, a bending or deformation mode and an asymmetrical of water (H_2O) shown in Fig. 25. These diagrams use spring and ball models. The spring represents the bond or bonds between the atoms. The stronger the bod has the higher frequency. The balls represent the atoms and the heavier they are the lower the frequency (see Eq. (71)). Thus, it is clear that strong bonds and light atoms will give higher frequencies of vibration and heavy atoms and weak bonds will give lower ones. This simple model is widely used to interpret vibrational spectra. If either molecule vibrates, the electron cloud will alter as the positive nuclei change position and depending on the nature of the change, this can cause a

change of dipole moment or polarization. In these triatomic molecules, the symmetrical stretch causes large polarization changes and hence strong Raman scattering with weak or no dipole change and hence weak or no IR absorption. The deformation mode cause a dipole change but little polarization change and hence strong IR absorption and weak or non-existent Raman scattering.

Figure 26 shows a comparison of the IR and Raman spectra for benzoic acid (see, e.g. [149] and references therein). The x - axis is given in wavenumbers for which the unit is cm^{-1} . For IR absorption each peak represents an energy of radiation absorbed by the molecule. The y - axis gives the amount of the light absorbed (% - unit) and is usually shown with the maximum absorbance as the lowest point on the trace. Raman scattering is presented only as the Stokes spectrum and is given as a shift in energy from the energy of the laser beam. This is obtained by subtracting the scattered energy from the laser energy. In this way the difference in energy corresponding to the ground and excited vibrational states (n and m in Fig. 24). This energy difference is what is measured directly by infrared. The scattering is measured as light detected by the spectrometer and the maximum amount of light detected is the highest point on the trace. Strictly speaking, Raman scattering should be expressed as a shift in energy from that of the exciting radiation and should be referred to as Δcm^{-1} but it is often expressed simply as cm^{-1} .

3.4.2. Isotope shift in molecular frequencies.

The study of the spectra of molecules in which one or more of their atoms are substituted by the corresponding isotope can often furnish information about the structure of the molecule which cannot at all, or only with difficulty, be obtained in any other way. This is especially true for those molecules in which a hydrogen atom is replaced by its heavy isotope deuterium, because for this substitution the relative change in the masses is so much greater than for all other isotopic substitutions. In order to make full use of the material which can be obtained in this way it is necessary to know exactly the changes which must be expected in the structure of the corresponding energy levels and wave functions.

When an atom of a molecule is replaced by an isotopic atom of the same element, it is assumed that the potential energy function and configuration of the molecule are changed by negligible amount (see, e.g. [24]). The frequencies of vibration may, however, be appreciably altered because of the change in mass involved (Eq. (71)). This especially, as defined above, true if hydrogen is the atom in question because of the large percentage change in mass. This shift or isotopic effect is very useful for several purposes. In the first place it may be used to help assign spectral lines to modes of vibration. Thus a normal mode of vibration in which the hydrogen atom in question is oscillating with a large relative amplitude will suffer a greater isotopic change in frequency than a normal mode in which a small relative amplitude. In the limiting case in which only hydrogen atoms are moving, replacement of all of them by deuterium atoms should decrease the corresponding fundamental frequency by the factor

$1/\sqrt{2}$, this being the square root of the ratio of masses. The totally symmetric (A_1) vibration of methane [149] is an example of this situation (see, also [150]). For CH_4 , the frequency is 2914.2 cm^{-1} which decrease to 2084.2 cm^{-1} for the case CD_4 . The ratio $\omega_{CD_4}/\omega_{CH_4}$ thus has experimental value of $\rho = \nu^i/\nu = \sqrt{\mu/\mu^i} = 0.715$, compared to a theoretically expected value of 0.707 [151]. The discrepancy is attributed to the fact that the observed frequencies are influenced by cubic and quartic terms in the potential energy (see above Eq. (77)), so that the vibration is not strictly harmonic as has been assumed in the theoretical development (for details, see [151]).

As was pointed out above, the potential energy functions of two isotopic molecules are identical to a high degree of approximation since they depend only on the motions of the electrons and the Coulomb repulsion of the nuclei [25]. The latter, of course, is entirely independent of these masses (see below). Not only the form of the potential curves, but also the relative positions of the potential curves of different electronic energies E_e are the same for two isotopic molecules [152]. The mass difference affects only, as noted above, the vibrational and rotational energy of the molecule in each electronic state. Restricting our considerations to the non-rotating molecule, we have for the band systems of two isotopic molecules, neglecting cubic and higher terms (in Eq. (77))

$$\nu = \nu_e + \omega'(v' + \frac{1}{2}) - \omega'_e x'_e (v' + \frac{1}{2})^2 - [\omega''_e (v'' + \frac{1}{2}) - \omega''_e x''_e (v'' + \frac{1}{2})^2] \quad (80)$$

and for isotope molecule

$$\nu' = \nu_e + \rho\omega'(v' + \frac{1}{2}) - \rho^2\omega'_e x'_e (v' + \frac{1}{2})^2 - [\rho\omega''_e (v'' + \frac{1}{2}) - \rho^2\omega''_e x''_e (v'' + \frac{1}{2})^2] . \quad (81)$$

Here ν_e is the difference in energy of the minima of the potential curves of the two electronic states involved which is the same to a very good approximation for the two isotopic molecules (see, however [28]). In the last two formula (80) and (81) one and two stroke label the upper and lower states. The equations (80) and (81) can be written in the approximation form

$$\nu = \nu_e + \nu_v ; \quad \nu^i = \nu_e + \rho\nu_v . \quad (82).$$

Following to the quantum mechanical formulae (80 - 81) do give a shift for the 0 - 0 band, owing to the fact that the zero - point vibration energies in the upper and lower states, in general, have different magnitudes and are different for the two isotopic molecules. A shift of the 0 - 0 band is directly observed in many isotope molecules (see, e.g. [25, 152]). Thus the existence of zero - point vibration is proved.

a) **isotope effect in water molecule.** Before to describing this effect we should remind the symmetry of the vibrations of water (see Fig. 25). We reproduce the C_{2v} point group (see, e.g. [153]) in Table 14 which would be correct point group for a single molecule of water. In this table, the symmetry elements are shown across the top. The first column contains a series of letters and numbers. The first one we see is A_1 . This is a way of describing a vibration, or for that matter an electronic function. It describes what happens to the vibration with each symmetry element of the molecule. These symbols are called irreducible representations and the top line always contains the one which refers to the most symmetrical vibration in terms of its behavior when it is rotated or

reflected by the symmetry operations. In higher symmetry point groups [153] where there is a centre of symmetry, there would also be a g or a u subscript. There are four possible letters, A, B, E and T. A and B mean that the vibration is singly degenerate. E means it is doubly degenerate and T means it is triply degenerate. In the C_{2v} point group all vibrations are singly degenerate. A is more symmetric than B. Across the line from the symbols representing the irreducible representations, there are a series of numbers for each. The numbers are either 1 or -1 and 1 is more symmetric than -1. For example, in the Table 14, an A_1 irreducible representation gives the value of 1 for every symmetry element. Fig. 25 shows three vibrations of water. For the stretching vibration, when the molecule is rotated about C_2 axis, the direction of the arrow representing a vibration does not change. This is the highest symmetry and is denoted as 1. In the asymmetric stretching vibration the sign of the arrow is reversed for C_2 and one plane. When this happens this is given the number -1. Thus, this last vibration belongs to a lower symmetry representation. It is conventionally given the irreducible representation B_1 . the main advantage of this assignment is that these tables also contain information that enables us to work on whether the vibration will be allowed by symmetry or not. For IR, this is done by multiplying the irreducible representation of the vibration by the irreducible representation of x, y or z which is given in the end column of the point group Table 14 in most, but not all, layouts. These correspond to three Cartesian coordinates of the molecule and are irreducible representation of the dipole operator. A similar approach is adopted for Raman scattering but in this case we look for the more complex quadratic functions $x^2, y^2, z^2, xy, x^2 - y^2$ etc., in the Table 14 and these are multiplied by the symmetry representation of the vibration.

Water is the main absorber of the sunlight. As we can see above, water molecule (with the molecular formula H_2O) are symmetric with two mirror planes of symmetry and a 2 - fold rotation axis. Its molecular diameter is about 2.75 Å [154]. The water molecule consists of two light atoms (H) and a relatively heavy atom (O). The approximately 16 - fold difference in mass gives rise to its ease of rotation and the significant relative movements of the hydrogen nuclei, which are in constant and significant relative movement.

The water molecule may vibrate in a number ways (see, Fig. 25). In the gas state the vibrations involve combination of symmetric stretch (ν_1), asymmetric stretch (ν_3) and bending (ν_2 of the covalent bonds with absorption intensity ($H_2^{16}O$) $\nu_1; \nu_2; \nu_3 = 0.07; 1.47; 1.0$ (see [154] and references therein). The frequencies of the main vibration of water isotopologues are shown in Table 15. The dipole moments of the molecule of water change in the direction of the movement of the oxygen atoms as shown by the arrows on the Fig. 25. As the H atoms are light, the vibrations have large amplitudes. The water molecule has a very small moment of inertia on rotation which gives to rich combined vibrational - rotational spectra in vapor containing tens of thousands to millions of absorption lines [23, 153]. In the liquid rotations tend to be restricted by hydrogen bonds, giving the librations. Also, spectral lines are broader causing overlap of many of the absorption peaks. The main stretching band in liquid water is shifted to a lower frequency ($\nu_3 = 3490 \text{ cm}^{-1}$ and $\nu_1 = 3280 \text{ cm}^{-1}$)

and the bending frequency increased ν_2 1644 cm^{-1} by hydrogen bonding (see, e.g. [154]). Isotope shift of water molecular frequencies is shown in Table 16. IR spectra of ordinary and heavy water are depicted in Fig. 27 (see, also [156] and references therein). In liquid water the IR spectrum is far more complex than the vapor due to vibrational overtones and combinations with librations (see Table 16). The librations depend on the moment of inertia such that the almost doubling of the moments of inertia of D_2O , relative to H_2O , reduces the frequencies by about a factor of $\sqrt{2}$ (see, however below).

b) isotope effect in "fullerene" molecule. The discovery [157] of the new fullerene allotropes of carbon, exemplified by C_{60} and soon followed by an efficient method for their synthesis [158], led to a burst of theoretical and experimental activity on their physical properties. Much of this activity concentrated on the vibrational properties of C_{60} and their elucidation by Raman scattering [159 - 161]. Comparison between theory and experiment (see, e.g. [161]) was greatly simplified by the high symmetry (I_h), resulting in only ten Raman active modes for the isolated molecule and the relative weakness of solid state effect [159], causing the crystalline C_{60} (c - C_{60}) Raman spectrum at low resolution to deviate only slightly from that expected for the isolated molecule [160]. Since the natural abundance of ^{13}C is 1.11% (see, e.g. [3]), almost half of all C_{60} molecules made from natural graphite contain one or more ^{13}C isotopes. If the squared frequency of a vibrational mod in a C_{60} molecule with n ^{13}C isotopes is written as a series $\omega^2 = \omega_{(0)}^2 + \omega_{(1)}^2 + \omega_{(2)}^2 + \omega_{(3)}^2 + \dots$ in the mass perturbation (where $\omega_{(0)}$ is an eigenmode frequency in a C_{60} molecule with 60 ^{12}C atoms), nondegenerate perturbation theory predicts for the two totally symmetric A_g modes a first - order correction given (see, e.g. [161])

$$\frac{\omega_{(1)}^2}{\omega_{(0)}^2} = - \frac{n}{720}. \quad (83)$$

This remarkable result, independent of the relative position of the isotopes within the molecule and equally independent of the unperturbed eigenvector, is a direct consequence of the equivalence of all carbon atoms in icosahedral C_{60} . To the same order of accuracy within nondegenerate perturbation theory, the Raman polarizability derivatives corresponding to the perturbed modes are equal to their unperturbed counterparts, since the mode eigenvectors remain unchanged. These results lead to the following conclusion [161]: The A_g Raman spectrum from a set of noninteracting C_{60} molecules will mimic their mass spectrum if the isotope effect on these vibrations can be described in terms of first - order nondegenerate perturbation theory. It is no means obvious that C_{60} will meet the requirements for the validity of this simple theorem. A nondegenerate perturbation expansion is only valid if the A_g mode is sufficiently isolated in frequency from its neighboring modes. Such isolation is not, of course, required by symmetry. Even if a perturbation expansion converges, there is no a priori reason why second - and higher - order correction to Eq. (83) should be negligible. As was shown in paper [161] the experimental Raman spectrum (see below) of C_{60} does agree with the prediction of Eq. (83). Moreover, as was shown in quoted paper, experiments with isotopically enriched samples display the striking correlation between mass and Raman spectra predicted by

the above simple theorem. Fig. 28 shows a high - resolution Raman spectrum at 30 K in an energy range close to the high - energy pentagonal - pinch $A_g(2)$ vibration according to [161]. Three peaks are resolved, with integrated intensity of 1.00; 0.95; and 0.35 relative to the strongest peak. The insert of this figure shows the evolution of this spectrum as the sample is heated. The peaks cannot be resolved beyond the melting temperature of CS_2 at 150 K. The theoretical fit [161] yields a separation of $0.98 \pm 0.01 \text{ cm}^{-1}$ between two main peaks and $1.02 \pm 0.02 \text{ cm}^{-1}$ between the second and third peaks. The fit also yields full widths at half maximum (FDWHM) of 0.64; 0.70 and 0.90 cm^{-1} , respectively. The mass spectrum of this solution shows three strong peaks (Fig. 28^b) corresponding to mass numbers 720; 721 and 722, with intensities of 1.00; 0.67 and 0.22 respectively as predicted from the known isotopic abundance of ^{13}C . The authors [161] assign the highest - energy peak at 1471 cm^{-1} to the $A_g(2)$ mode of isotopically pure C_{60} (60 ^{12}C atoms). The second peak at 1470 cm^{-1} is assigned to C_{60} molecules with one ^{13}C isotope, and the third peak at 1469 cm^{-1} to C_{60} molecules with two ^{13}C isotopes. The separation between the peaks is in excellent agreement with the prediction from Eq. (83), which gives 1.02 cm^{-1} . In addition, the width of the Raman peak at 1469 cm^{-1} , assigned to a C_{60} molecule with two ^{13}C atoms, is only 30 % larger than the width of the other peaks. This is consistent with the prediction of Eq. (83) too, that the frequency of the mode will be independent of the relative position of the ^{13}C isotopes within the molecule. The relative intensity between two isotope and one isotope Raman lines agrees well with the mass spectrum ratios. Concluding this part we stress that the Raman spectra of C_{60} molecules show remarkable correlation with their mass spectra. Thus the study of isotope - related shift offers a sensitive means to probe the vibrational dynamics of C_{60} .

3.4.3. "Mass - independent" isotope effect.

More than the quarter of a century [162] Thiemens and Heidenreich [163] demonstrated essentially equal effects of isotopic substitution of ^{18}O and ^{17}O for ^{16}O on the rates [164, 165] of formation of ozone by an electric discharge in oxygen (see, also reviews [166 - 168]). Thiemens and Heidenreich called this observation a "non - mass dependent" or "mass - independent" isotopic effect. The observed non - mass dependent oxygen isotope formation is a kinetic isotope effect [164]. The observed effect was a remarkable deviation from the accepted theory (see, e.g. [169]) of isotope effects, which would predict that the effect of ^{18}O would be approximately double that of ^{17}O . The mechanism for the effect remains uncertain. Since that first publication, the ozone reaction has been extensively investigated both experimentally and theoretically. A number of other reactions have been labeled "mass - independent" isotope effect [166]. Mass - independent isotopic composition have been observed in O_3 , CO_2 , N_2O and CO in Earth's atmosphere and in carbonate from a martian meteorite, which suggests a role for mass - independent processes in the atmosphere of Mars [170]. According to [167], the observed mass - independent meteoritic oxygen and sulfur isotopic (see, also [171]) compositions may derive from chemical processes

in the presolar nebula and their distributions could provide insight into early solar system evolution (see, also [1 - 2]). Although the magnitude and direction of variation of the isotope ratios for these processes vary, they have one common feature - they all depend on mass.

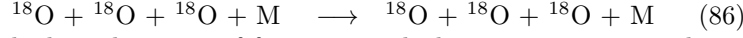
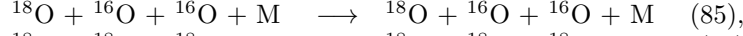
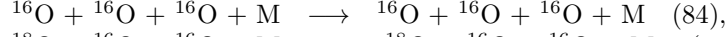
The most complete set of experimental data for oxygen isotope effects in the photochemical formation of ozone has been obtained by the Mauersberger group [172 - 174]. These authors managed to sort out rate constants (see below) for many reactions of labeled O atoms and/or labeled O₂ molecules providing a severe test for theory (see, also review [168]). At present time, the most successful theory in terms of agreement with experiment is that of Marcus group [175 - 179], which is based on the RRKM (Rice - Ramsperger - Kessel - Marcus) theory of recombination reactions, and this will be described.

Quantum mechanical resonance calculations as performed by Babikov et al. [180 - 182] are the ultimate tool for investigating the formation of ozone, but these attempts are the first in the direction of "first - principle" solutions of the ozone isotope effect [171]. Resonance lifetimes for large total angular momenta are required and their determination is a formidable task. What is the impact of the shallow van der Waals - like wells and the long - lived states they support? Do they contribute to the stabilization process or are these states so fragile that the first collision with M (third body) destroys them? What is the role of the excited electronic states which correlate with ground state products? Moreover, how the vibrational energy of the excited complex is removed by the bath atom or molecule is largely not understood.

On the basis of the assumption that any deviation from mass dependence must reflect of a nuclear process, Hulston and Thode [183] suggested that deviations from mass - dependent isotopic composition may be used to distinguish nuclear from chemical and physical processes in meteoritic measurements [170]. The observation by Clayton et al. [184] of a non - mass dependent isotopic composition in meteoritic substances was thus interpreted as indicating that the meteorite contained residual primary grains from a nucleosynthesis process [1 - 2]. Subsequently, the authors of the paper [163] reported a chemically produced mass - independent isotopic composition in the formation of ozone from molecular oxygen. The observed fractionation pattern was the same as observed in meteoritic substances and thus it was suggested that the observed isotopic composition in a meteoritic material could reflect a chemical instead a nuclear process.

Gellene [185] modeled the isotope fractionation based on nuclear symmetry. In his approach, symmetry restrictions arise for homonuclear diatomic (for example, ¹⁶O¹⁶ and ¹⁸O¹⁸O) involved in the O + O₂ collision because a fraction of their rotational states (f - parity) correlate with those of the corresponding ozone molecule. In contrast, in the case of heteronuclear oxygen molecules (for example, ¹⁶O¹⁸O), all of their rotational states (e and f parity) correlate with those of the resulting ozone molecule. Gellen's model can reproduce the general features of the enrichment pattern quite well. A number of others attempts have been made [186] to find an explanation of the ozone isotope anomaly; none were able to account for the experimental results [168].

The role of molecular symmetry was questioned by Anderson et al. [172], who presented rate coefficients of four selected ozone formation channels. Whereas three channels



had similar rates of formation, which were consistent with a value of $\sim 6 \cdot 10^{-34} \text{ cm}^6\text{s}^{-1}$ [168], the fourth channel



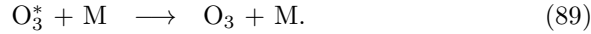
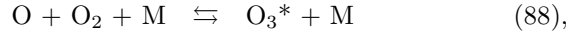
resulted in a rate coefficient that was 50% higher than the other three. Here M represents a third - body molecule as was indicate early. The difference in the rate coefficients of reactions 2 and 4 was unexpected. Thus, the difference in the rate coefficients of reactions 2 and 4 does not support an important role of symmetry in the isotope enrichment process. Later, a similar conclusion was reached by Sahested et al. [187] who performed rate coefficient studies for the $^{16}\text{O} - ^{18}\text{O}$ system on dual channel processes, using CO_2 and A as third - body molecules, but without isolating the process contributing to the enrichments.

More details studies [174] are shown:

- 1) molecular symmetry cannot explain the ozone enrichment process;
- 2) a collision between a light oxygen atom and a heavier molecule will result in a rate coefficient that is higher than the coefficient from reactions involving only one isotope.

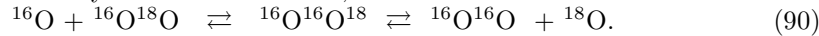
Thus, experimental results presented provide new insights into the puzzling ozone isotope effect.

To concluding this part we should mentioned some theoretical results of Marcus et al. Marcus et al. recognized the fact that the ozone isotope effect in this reaction is very pressure dependence (see, Fig. 29), as indeed is the rate constant for recombination of an oxygen molecule with an oxygen atom to form ozone. The reaction may be written



In this reaction mechanism, the ozone molecule initially formed with excess vibrational energy (O_3^*) will revert to reactants unless it is stabilized by energy transfer by collision with another molecule (third body), M. This is the source of the pressure dependence of the rate constant. Marcus and co - workers [175 - 179] found two factors important in the RKKM analysis of the isotope effect in this pressure - dependent region:

- a) zero - point energy difference between isotopic species in competing reactions of asymmetrical molecules, such as



The lower zero - point energy [164] of the heavier molecule increases the region of phase space accessible to the transition state, favoring this channel.

- b) a "non RKKM" effect that precludes certain regions of phase space to a symmetrical transition state, thus preventing the complete randomization of vibrational energy distribution (for details see [167, 168]).

In addition to the formation of ozone, a number of other three - isotope systems involving oxygen or sulfur isotopes have been found to exhibit non - mass dependent isotope effects [166, 171]. The bright example of this situation a three - isotope system which have ^{32}S - ^{33}S - ^{34}S combination.

Thus, in the formation of ozone from molecular oxygen by photolysis or in an electric discharge, the kinetic isotope effects of ^{17}O and ^{18}O are essentially equal, in spite of the predictions of the accepted theory. This is clearly a non - mass dependent isotope effect.

4. Isotope Effect in Solids.

4.1. Elementary excitations.

The modern view of solid state physics is based on the presentation of elementary excitations, having mass, quasiimpuls, electrical charge and so on (see, e.g [188]). According to this presentation the elementary excitations of the non - metallic materials are electrons (holes), excitons (polaritons [189]) and phonons [190]. The last one are the elementary excitations of the crystal lattice, the dynamics of which is described in harmonic approximation. as is well - known, the base of such view on solid are the multiparticle approach. In such view, the quasiparticles of solid are ideal gas, which described the behavior of the system, e.g. noninteracting electrons. We should add such approach to consider the theory of elementary excitations as suitable model for the application of the common methods of the quantum mechanics for the solution solid state physics task. In this part of our review will be consider not only the manifestations of the isotope effect in different solids, but also will bring the new accurate results, showing the quantitative changes of different characteristics of phonons and electrons (excitons) in solid with isotopical substitution (see, also [191]). By the way, isotopic effect become more pronounced when we dealing with solids. For example, on substitution of H with D the change in energy of the electron transition in solid state (e.g. LiH) is two orders of magnitude larger than in atomic hydrogen (see, e.g. [48]). In the use of an elementary excitations to describe the complicated motion of many particles has turned out to be an extraordinary useful device in contemporary physics, and it is view of a solid which we describe in this part of review,

The basic Hamiltonian which our model of the solid is of the form [191]

$$H = H_{ion} + H_{electron} + H_{electron-ion} \quad (91)$$

where

$$H_{ion} = \sum_i \frac{p_i^2}{2m} + \frac{1}{2} \sum_{i \neq j} V(R_i - R_j) \quad (92),$$

$$H_{electron} = \sum_i \frac{p_i^2}{2m} + \frac{1}{2} \sum_{i \neq j} \frac{e^2}{|r_i - r_j|} \quad (93),$$

$$H_{electron-ion} = \sum_{i,j} v(r_i - R_j) \quad (94)$$

H_{ion} describes a collection of ions (of a single species) which interact through a potential $V(R_i - R_j)$ which depends only on the distance between ions. By ion we mean a nucleus plus the closed - shell, or core, electrons, that is, those electrons which are essentially unchanged when the atoms are brought together to make a solid. $H_{electron}$ presents the valence electrons (the electrons outside the last closed shell), which are assumed to interact via a Coulomb interaction. Finally, $H_{electron-ion}$ describes the interaction between the electrons (excitons) and the ions, which is again assumed to be represented by a suitable chosen potential.

In adopting (91) as our basic Hamiltonian, we have already made a number of approximation in a treatment of a solid. Thus, in general the interaction between ions is not well - represented by a potential $V(R)$, when the coupling between the closed - shell electrons on different ions begins to play an important role (see, e.g. [192, 193]). Again, in using a potential to represent electron - ion interaction, we have neglected the fact that the ions possess a structure (the core electrons); again, when the Pauli principle plays an important role in the interaction between the valence electrons, that interaction may no longer be represented by a simple potential. It is desirable to consider the validity of these approximations in detail (for detail see, e.g. [193]). In general one studies only selected parts of the Hamiltonian (91). Thus, for example, the band theory of solids is based upon the model Hamiltonian [192, 194].

$$H_B = \sum_i \frac{p_i^2}{2m} + \sum_{i,j} v(r_i - R_{j0}) + V_H(r_i), \quad (95)$$

where the R_{j0} represents the fixed equilibrium positions of the ions and the potential V_H describes the (periodic) Hartree potential of the electrons. One studies the motion of a single electron in the periodic field of the ions and the Hartree potential, and takes the Pauli principle into account in the assignment of one - electron states. In so doing one neglects aspects other than the Hartree potential of the interaction between electrons. On the other hand, where one is primarily interested in understanding the interaction between electrons in metals, it is useful to consider only (93), replacing the effect of the ion cores by a uniform distribution of positive charge [195]. In this way one can approximate the role that electron interaction plays without having present the additional complications introduced by the periodic ion potential. Of course one wants finally to keep both the periodic ion potential and the electron interactions, and to include as well the effects associated with departure of the ions from the equilibrium positions, since only in this way does not arrive at a generally adequate description of the solid. Usually for the elementary excitations in solids by first considering various different parts of the Hamiltonian (91) and then taking into account the remaining terms which act to couple different excitations.

4.2. Phonons.

The simplest kind of motion in solids is the vibrations of atoms around the equilibrium point. The interaction of the crystalforming particles with the one

another at the move of the one atom entanglements neighbor atoms [26]. The analysis of this kind motion shows that the elementary form of motion is the wave of the atom displacement. As is well - known that the quantization of the vibrations of the crystal lattice and after introduction of the normal coordinates, the Hamiltonian of our task will be have the following relation (see, e.g. [196])

$$H(Q,P) = \sum_{i,q} \left[-\frac{\hbar^2}{2} \frac{\partial^2}{\partial Q^2(\vec{q})} + \frac{1}{2} \omega_j^2 Q_j^2(\vec{q}) \right] \quad (96).$$

In this relation, the sum, where every addend means The Hamiltonian of linear harmonic oscillator with coordinate $Q_j(\vec{q})$, the frequency $\omega_j(\vec{q})$ and the mass, which equals a unit. If the Hamiltonian system consists of the sum, where every addend depends on the coordinate and conjugate its quasiimpuls, then according to quantum mechanics [49] the wave function of the system equals the product of wave functions of every appropriate addend and the energy is equal to the sum of assigned energies. Any separate term of the Hamiltonian (96) corresponds, as indicate above, the linear oscillator

$$-\frac{\hbar^2}{2} \frac{\partial^2 \Psi}{\partial Q^2} + \frac{1}{2} \omega^2 Q^2 \Psi = \varepsilon \Psi. \quad (97)$$

Solving last equation and finding the eigenvalues and eigenfunctions and then expressing explicitly the frequency, we will obtain for model with two atoms in primitive cell (with masses M_1 and M_2) the following equation

$$\omega^2 \simeq 2C \left(\frac{1}{M_1} + \frac{1}{M_2} \right) \quad (98)$$

and

$$\omega^2 \simeq \frac{C}{2(M_1 + M_2)} K^2 a^2. \quad (99)$$

Taking into account that $K_{\max} = \pm \pi/a$, where a is a period of the crystal lattice, i.e. K_{\max} respond the border of the first Brillouin zone

$$\omega^2 = \frac{2C}{M_1} \text{ and } \omega^2 = \frac{2C}{M_2} \quad (100)$$

Formula (98) describes the optical branch of vibrations whereas (99) - acoustical branch of vibrations (see, e.g. Fig. 5.17^a in [197]). Usually the last formula is written in this way

$$\omega = \sqrt{\frac{\alpha}{M}}, \quad (101)$$

where α is so - called the force constant (see, also formula (76)). Here, as early M is the mass of vibrated atom (ion). From the preceding relation it is clear that, as in molecular physics, in solid the isotope effect directly manifests in vibration spectrum, which depends on the symmetry [198] measures either in IR - absorption or in Raman scattering of light. Before analyzing Raman scattering spectra of different solids we briefly consider the classical approximation of the mechanism of Raman effect [199].

Historically, Raman scattering denotes inelastic scattering of light by molecular vibrations or by optical phonons in solids. In a macroscopic picture, the Raman effect in crystals is explained in terms of the modulation of polarizability by the quasi - particle under consideration. The assumption that the polarization depends linearly upon the electric field strength [145] is a good approximation and is invariably used when discussing the scattering of light by crystal excited by lasers. However, the approximation is not valid for large strength such as can be obtained from pulsed lasers [147]. The polarization may then be expressed as

$$P = \alpha E + \frac{1}{2}\beta E^2 + \frac{1}{6}\gamma E^3 + \frac{1}{24}\delta E^4 + \dots, \quad (102)$$

where β , the first hyperpolarizability coefficient, plays an important part for large values of E , since it is responsible for the phenomenon of optical harmonic generation using Q - switched lasers. Isolated atoms have $\beta = 0$, since, like μ the dipole moment, it arises from interactions between atoms. A simplified theory of Rayleigh scattering, the Raman effect, harmonic generation and hyper Raman scattering is obtained by setting (see, e.g. [147])

$$E = E_0 \cos \omega_0 t, \quad (103)$$

$$\alpha = \alpha_0 + \left(\frac{\partial \alpha}{\partial Q}\right)Q, \quad (104)$$

$$\beta = \beta_0 + \left(\frac{\partial \beta}{\partial Q}\right)Q, \quad (105)$$

$$Q = Q_0 + \cos \omega_v t. \quad (106).$$

Here Q is a normal coordinate, ω_v is the corresponding vibrational frequency and ω_0 is the laser frequency. After that we have

$$P = \alpha_0 E_0 \cos \omega_v t + \frac{1}{2} \left(\frac{\partial \alpha}{\partial Q}\right) Q_0 E_0 \cos \omega_0 t \cos \omega_v t + \frac{1}{2} \beta_0 E_0^2 \cos^2 \omega_0 t + \frac{1}{2} \left(\frac{\partial \beta}{\partial Q}\right) Q_0 E_0^2 \cos^2 \omega_0 t \cos \omega_v t. \quad (107)$$

Then, after small algebra, we obtaine

$$P = \alpha_0 E_0^2 \cos \omega_v t + \frac{1}{2} \left(\frac{\partial \alpha}{\partial Q}\right) Q_0 E_0 \cos(\omega_0 - \omega_v)t + \cos(\omega_0 + \omega_v)t + \frac{1}{2} \beta_0 E_0^2 + \frac{\beta_0}{4} E_0^2 \cos 2\omega_0 t + \frac{1}{2} Q_0 E_0^2 \left(\frac{\partial \beta}{\partial Q}\right) \cos(2\omega_0 - \omega_v)t + \cos(2\omega_0 - \omega_v)t. \quad (108).$$

In last relation the first term describes the Rayleigh scattering, second - Raman scattering, third - d.c. polarization, fourth - frequency doubling and the last - hyper Raman effect. Thus the hyper Raman effect is observed with large electric field strength in the vicinity of twice the frequency of the exciting line with separations corresponding to the vibrational frequencies. α and β are actually tensors and β components $\beta_{\alpha\beta\gamma}$ which are symmetrical suffixes [200].

Semiconducting crystals (C, Si, Ge, α - Sn) with diamond - type structure present ideal objects for studying the isotope effect by the Raman light - scattering method. At present time this is facilitated by the availability of high - quality crystals grown from isotopically enriched materials (see, e.g [27] and references therein). In this part our understanding of first - order Raman light scattering spectra in isotopically mixed elementary and compound (CuCl, GaN, GaAs) semiconductors having a zinc blende structure is described. Isotope effect in light scattering spectra in GE crystals was first investigated in the paper by Agekyan et al. [201]. A more detailed study of Raman light scattering spectra in isotopically mixed Ge crystals has been performed by Cardona and coworkers [27].

It is known that materials having a diamond structure are characterized by the triply degenerate phonon states in the Γ point of the Brillouin zone ($\vec{k} = 0$). These phonons are active in the Raman scattering spectra, but not in the IR absorption one [198]. Figure 30^a demonstrates the dependence of the shape and position of the first - order line of optical phonons in germanium crystal on the isotope composition at liquid nitrogen temperature (LNT) [202]. The coordinate of the center of the scattering line is proportional to the square root of the reduced mass of the unit cell, i.e \sqrt{M} . It is precisely this dependence

that is expected in the harmonic approximation. An additional frequency shift of the line is observed for the natural and enriched germanium specimens and is equal, as shown in Ref. [27] to 0.34 ± 0.04 and $1.06 \pm 0.04 \text{ cm}^{-1}$, respectively (see, e.g. Fig. 7 in Ch. 4 of Ref. [203]).

First - order Raman light - scattering spectrum in diamond crystals also includes one line with maximum at $\omega_{LTO}(\Gamma) = 1332.5 \text{ cm}^{-1}$. In Fig. 30^b the first - order scattering spectrum in diamond crystals with different isotope concentration is shown [204]. As shown below, the maximum and the width of the first - order scattering line in isotopically - mixed diamond crystals are nonlinearly dependent on the concentration of isotopes x . The maximum shift of this line is 52.3 cm^{-1} , corresponding to the two limiting values of $x = 0$ and $x = 1$. Analogous structures of first - order light scattering spectra and their dependence on isotope composition has by now been observed many times, not only in elementary Si, and α - Sn, but also in compound CuCl and GaN semiconductors (for more details see reviews [26, 27]). Already short list of data shows a large dependence of the structure of first - order light - scattering spectra in diamond as compared to other crystals (Si, Ge). This is the subject detailed discussion in [205].

Second - order Raman spectra in natural and isotopically mixed diamond have been studied by Chrenko [206] and Hass et al. [207]. Second - order Raman spectra in a number of synthetic diamond crystals with different isotope composition shown in Fig. 31 are measured with resolution ($\sim 4 \text{ cm}^{-1}$) worse than for first - order scattering spectra. The authors of cited work explain this fact by the weak signal in the measurement of second - order Raman scattering spectra. It is appropriate to note that the results obtained in [207] for natural diamond ($C_{13C} = 1.1\%$), agree well with the preceding comprehensive studies of Raman light - scattering spectra in natural diamond [208]. As is clearly seen from Fig. 31 the structure of second - order light scattering "follows" the concentration of the ^{13}C isotope. It is necessary to add that in the paper by Chrenko [206] one observes a distinct small narrow peak above the high - frequency edge of LO phonons and the concentration of ^{13}C $x = 68\%$. Note is passing that second - order spectra in isotopically mixed diamond crystals were measured in the work by Chrenko [206] with a better resolution than the spectra shown in Fig. 31. Second - order Raman light scattering spectra and IR absorption spectra in crystals of natural and isotopically enriched ^{70}Ge can be found in [26].

A comprehensive interpretation of the whole structure of second - order Raman light - scattering spectra in pure LiH (LiD) crystals is given in [29, 205, 209]. Leaving this question, let us now analyze the behavior of the highest frequency peak after the substitution of hydrogen for deuterium (see, also [209]).

Absorption behavior of an IR - active phonon in mixed crystals with a change in the concentrations of the components can be classified into two main types: one and two - mode (see, e.g. the review [210]). Single - mode behavior means that one always has a band in the spectrum with a maximum gradually drifting from one endpoint to another. Two - mode behavior is defined by the presence, in the spectrum, of two bands characteristic of each components lead not only

to changes in the frequencies of their maxima, but mainly to a redistribution of their intensities. In principle, one and the same system can show different types of behavior at opposite ends.[211]. The described classification is qualitative and is rarely realized in its pure form (see, also [212]). The most important necessary condition for the two - mode behavior of phonons (as well as of electrons [213]) is considered to be the appearance of the localized vibration in the localized defect limit. In the review [210] a simple qualitative criterion for determining the type of the IR absorption behavior in crystals with an NaCl structure type has been proposed (see also [213]). Since the square of the TO (Γ) phonon frequency is proportional to the reduced mass of the unit cell M , the shift caused by the defect is equal to

$$\Delta = \omega_{\text{TO}}^2 \left(1 - \frac{\bar{M}}{M}\right). \quad (109)$$

This quantity is compared in [210] with the width of the optical band of phonons which, neglecting acoustical branches and using the parabolic dispersion approximation, is written as

$$W = \omega_{\text{TO}}^2 \left(\frac{\varepsilon_0 - \varepsilon_\infty}{\varepsilon_0 + \varepsilon_\infty}\right). \quad (110)$$

A local or gap vibrations appears, provided the condition $|\Delta| > (1/2)W$ is fulfilled. As mentioned, however, in [210] in order for the two peaks to exist up to concentrations on the order of ~ 0.5 , a stronger condition $|\Delta| > W$ has to met. Substituting the numerical values from Tables 1 and 2 of [205] into formulas (109) and (110) shows that for LiH (LiD) there holds (since $\Delta = 0.44\omega_{\text{TO}}^2$ and $W = 0.58\omega_{\text{TO}}^2$) the following relation:

$$|\Delta| > (1/2)W. \quad (111)$$

Thereby it follows that at small concentrations the local vibration should be observed. This conclusion is in perfect agreement with earlier described experimental data [209]. As to the second theoretical relation $\Delta > W$, one can see from the above discussion that for LiH (LiD) crystals the opposite relation, i.e. $W > \Delta$, is observed [214].

Following the results of [215], in Fig. 32 we show the second - order Raman scattering spectra in mixed $\text{LiH}_x\text{D}_{1-x}$ crystals at room temperature. In addition to what has been said on Raman scattering spectra at high concentration [215], we note that as the concentration grows further ($x > 0.15$) one observes in the spectra a decreasing intensity in the maximum of $2\text{LO}(\Gamma)$ phonons in LiD crystal with a simultaneous growth in intensity of the highest frequency peak in mixed $\text{LiH}_x\text{D}_{1-x}$ crystals. The nature of the latter is in the renormalization of $\text{LO}(\Gamma)$ vibrations in mixed crystal [216]. Comparison of the structure of Raman scattering spectra (curves 1 and 2 in Fig. 32) allows us, therefore, to conclude that in the concentration range of $0.1 < x < 0.45$ the Raman scattering spectra simultaneously contain peaks of the $\text{LO}(\Gamma)$ phonon of pure LiD and the $\text{LO}(\Gamma)$ phonon of the mixed $\text{LiH}_x\text{D}_{1-x}$ crystal. For further concentration growth ($x > 0.45$) one could mention two effects in the Raman scattering spectra of mixed crystals. The first is related to an essential reconstruction of the acoustooptical part of the spectrum. This straightforwardly follows from a comparison of the structure of curves 1 -3 in Fig. 32. The second effect originates from a further shift of the highest frequency peak toward still higher frequencies, related to

the excitation of LO(Γ) phonons. The limit of this shift is the spectral location of the highest frequency peak in LiH. Finishing our description of the Raman scattering spectra, it is necessary to note that a resonance intensity growth of the highest frequency peak is observed at $x > 0.15$ in all mixed crystals (for more details see [217]).

Once more reason of the discrepancy between theory and results of the experiment may be connected with not taking into account in theory the change of the force-constant at the isotope substitution of the smaller in size D by H ion [218]. We should stress once more that among the various possible isotope substitution, by far the most important in vibrational spectroscopy is the substitution of hydrogen by deuterium. As is well-known, in the limit of the Born-Oppenheimer approximation the force-constant calculated at the minimum of the total energy depends upon the electronic structure and not upon the mass of the atoms. It is usually assumed that the theoretical values of the phonon frequencies depend upon the force-constants determined at the minimum of the adiabatic potential energy surface. This leads to a theoretical ratio $\omega(H)/\omega(D)$ of the phonon frequencies that always exceed the experimental data. Very often anharmonicity has been proposed to be responsible for lower value of this ratio. In isotope effect two different species of the same atom will have different vibrational frequencies only because of the difference in isotopic masses. The ratio p of the optical phonon frequencies for LiH and LiD crystals is given in harmonic approximation by:

$$p = \frac{\omega(H)}{\omega(D)} = \sqrt{\frac{M(LiD)}{M(LiH)}} \simeq \sqrt{2} \quad (112)$$

while the experimental value (which includes anharmonic effects) is $1.396 \div 1.288$ (see Table1 in Ref. [218]). In this Table there are the experimental and theoretical values of p according to formula (112), as well as the deviation $\delta = \frac{P_{Theory} - P_{exp}}{P_{theory}}$ of these values from theoretical ones. Using the least squares method it was found the empirical formula of $\ln(\delta\%) \sim f[\ln[\frac{\partial E}{\partial M}]]$ which is depicted on Fig. 33. As can be seen the indicated dependence has in the first approximation a linear character:

$$\ln(\delta\%) = -7.5 + 2\ln(\frac{\partial E}{\partial M}). \quad (113)$$

From the results of Fig. 33, it can be concluded that only hydrogen compounds (and its isotope analog - deuterium) need to take into account the force-constant changes in isotope effect. It is also seen that for semiconductor compounds (on Fig. 33 - points, which is below of Ox line) the isotope effect has only the changes of the isotope mass (details see [218]).

Thus, the experimental results presented in this section provide, therefore, evidence of, first, strong scattering potential (most importantly, for optical phonons) and, second, of the insufficiency of CPA model for a consistent description of these results [207].

4.3. Electronic excitations.

Isotopic substitution only affects the wavefunction of phonons; therefore, the energy values of electron levels in the Schrödinger equation ought to have

remained the same. This, however, is not so, since isotopic substitution modifies not only the phonon spectrum, but also the constant of electron-phonon interaction (see above). It is for this reason that the energy values of purely electron transition in molecules of hydride and deuteride are found to be different [24]. This effect is even more prominent when we are dealing with a solid [219]. Intercomparison of absorption spectra for thin films of LiH and LiD at room temperature revealed that the longwave maximum (as we know now, the exciton peak [220]) moves 64.5 meV towards the shorter wavelengths when H is replaced with D. For obvious reasons this fundamental result could not then receive consistent and comprehensive interpretation, which does not belittle its importance even today. As will be shown below, this effect becomes even more pronounced at low temperatures (see, also [26]).

The mirror reflection spectra of mixed and pure LiD crystals cleaved in liquid helium are presented in Fig. 34. For comparison, on the same diagram we have also plotted the reflection spectrum of LiH crystals with clean surface. All spectra have been measured with the same apparatus under the same conditions. As the deuterium concentration increases, the long-wave maximum broadens and shifts towards the shorter wavelengths. As can clearly be seen in Fig. 34, all spectra exhibit a similar long-wave structure. This circumstance allows us to attribute this structure to the excitation of the ground (1s) and the first excited (2s) exciton states. The energy values of exciton maxima for pure and mixed crystals at 2 K are presented in Table 17. The binding energies of excitons E_b , calculated by the hydrogen-like formula, and the energies of interband transitions E_g are also given in Table 17.

Going back to Fig. 34, it is hard to miss the growth of Δ_{12} , [221], which in the hydrogen-like model causes an increase of the exciton Rydberg with the replacement of isotopes (see Fig. 90 in [26]). When hydrogen is completely replaced with deuterium, the exciton Rydberg (in the Wannier-Mott model) increases by 20% from 40 to 50 meV, whereas E_g exhibits a 2% increase, and at $2 \div 4.2$ K is $\Delta E_g = 103$ meV. This quantity depends on the temperature, and at room temperature is 73 meV, which agrees well enough with $\Delta E_g = 64.5$ meV as found in the paper of Kapustinsky et al. Isotopic substitution of the light isotope (^{32}S) by the heavy one (^{34}S) in CdS crystals [222] reduces the exciton Rydberg, which was attributed to the tentative contribution from the adjacent electron bands (see also [228]), which, however, are not present in LiH. The single-mode nature of exciton reflection spectra of mixed crystals $\text{LiH}_x\text{D}_{1-x}$ agrees qualitatively with the results obtained with the virtual crystal model (see e.g. Elliott et al. [210]; Onodera and Toyozawa [223]), being at the same time its extreme realization, since the difference between ionization potentials ($\Delta\zeta$) for this compound is zero. According to the virtual crystal model, $\Delta\zeta = 0$ implies that $\Delta E_g = 0$, which is in contradiction with the experimental results for $\text{LiH}_x\text{D}_{1-x}$ crystals. The change in E_g caused by isotopic substitution has been observed for many broad-gap and narrow-gap semiconductor compounds (see also below).

All of these results are documented in Table 21 of Ref.[26], where the variation of E_g , E_b , are shown at the isotope effect. We should highlighted here that

the most prominent isotope effect is observed in LiH crystals, where the dependence of $E_b = f(C_H)$ is also observed and investigated. To end this section, let us note that E_g decreases by 97 cm^{-1} when ^7Li is replaced with ^6Li .

Further we will briefly discuss of the variation of the electronic gap (E_g) of semiconducting crystals with its isotopic composition. In the last time the whole row of semiconducting crystals were grown. These crystals are diamond, copper halides, germanium, silicon [321], CdS and GaAs. All numerated crystals show the dependence of the electronic gap on the isotope masses (see, reviews [26, 27]).

Before we complete the analysis of these results we should note that before these investigations, studies were carried out on the isotopic effect on exciton states for a whole range of crystals by Kreingol'd and coworkers (see, also [203]). First, the following are the classic crystals Cu_2O [224, 225] with the substitution $^{16}\text{O} \rightarrow ^{18}\text{O}$ and $^{63}\text{Cu} \rightarrow ^{65}\text{Cu}$. Moreover, there have been some detailed investigations of the isotopic effect on ZnO crystals, where E_g was seen to increase by 55 cm^{-1} ($^{16}\text{O} \rightarrow ^{18}\text{O}$) and 12 cm^{-1} (at $^{64}\text{Zn} \rightarrow ^{68}\text{Zn}$) [226, 227]. In [222] it was shown that the substitution of a heavy ^{34}S isotope for a light ^{32}S isotope in CdS crystals resulted in a decrease in the exciton Rydberg constant (E_b), which was explained tentatively [228] by the contribution from the nearest electron energy bands, which however are absent in LiH crystals.

More detailed investigations of the exciton reflectance spectrum in CdS crystals were done by Zhang et al. [229]. Zhang et al. studied only the effects of Cd substitutions, and were able to explain the observed shifts in the band gap energies, together with the overall temperature dependence of the band gap energies in terms of a two-oscillator model provided that they interpreted the energy shifts of the bound excitons and $n = 1$ polaritons as a function of average S mass reported as was noted above, earlier by Kreingol'd et al. [222] as shifts in the band gap energies. However, Kreingol'd et al. [222] had interpreted these shifts as resulting from isotopic shifts of the free exciton binding energies (see, also [221]), and not the band gap energies, based on their observation of different energy shifts of features which they identified as the $n = 2$ free exciton states (for details see [222]). The observations and interpretations, according Meyer et al. [230], presented by Kreingol'd et al. [222] are difficult to understand, since on the one hand a significant band gap shift as a function of the S mass is expected [229], whereas it is difficult to understand the origin of the relatively huge change in the free exciton binding energies which they claimed. Very recently Meyer et al. [230] reexamine the optical spectra of CdS as function of average S mass, using samples grown with natural Cd and either natural S ($\sim 95\% ^{32}\text{S}$), or highly enriched ($99\% ^{34}\text{S}$). These authors observed shifts of the bound excitons and the $n = 1$ free exciton edges consistent with those reported by Kreingol'd et al. [222], but, contrary to their results, Meyer et al. observed essentially identical shifts of the free exciton excited states, as seen in both reflection and luminescence spectroscopy. The reflectivity and photoluminescence spectra in polarized light ($\vec{E} \perp \vec{C}$) over the A and B exciton energy regions for the two samples depicted on the Fig. 35. For the $\vec{E} \perp \vec{C}$ polarization used in

Fig. 35 both A and B excitons have allowed transitions, and therefore reflectivity signatures. Fig. 35 also reveals both reflectivity signatures of the $n = 2$ and 3 states of the A exciton as well that of the $n = 2$ state of the B exciton.

In Table 18 Meyer et al. summarized the energy differences $\Delta E = E(\text{Cd}^{34}\text{S}) - E(\text{Cd}^{\text{nat}}\text{S})$, of a large number of bound exciton and free exciton transitions, measured using photoluminescence, absorption, and reflectivity spectroscopy, in CdS made from natural S ($\text{Cd}^{\text{nat}}\text{S}$, 95% ^{32}S) and from highly isotopically enriched ^{34}S (Cd^{34}S , 99% ^{34}S). As we can see, all of the observed shifts are consistent with a single value, $10.8 \pm 0.2 \text{ cm}^{-1}$. Several of the donor bound exciton photoluminescence transitions, which in paper [230] can be measured with high accuracy, reveal shifts which differ from each other by more than the relevant uncertainties, although all agree with the $10.8 \pm 0.2 \text{ cm}^{-1}$ average shift. These small differences in the shift energies for donor bound exciton transitions may reflect a small isotopic dependence of the donor binding energy in CdS. This value of $10.8 \pm 0.2 \text{ cm}^{-1}$ shift agrees well with the value of 11.8 cm^{-1} reported early by Kreingol'd et al. [222] for the $B_{n=1}$ transition, particularly when one takes into account the fact that enriched ^{32}S was used in that earlier study whereas Meyer et al. have used natural S in place of an isotopically enriched Cd^{32}S (for details see [230]).

Authors [230] conclude that all of the observed shifts (see Table 18) arise predominantly from an isotopic dependence of the band gap energies, and that the contribution from any isotopic dependence of the free exciton binding energies is much smaller. On the basis of the observed temperature dependencies of the excitonic transitions energies, together with a simple two-oscillator model, Zhang et al. [229] earlier calculated such a difference, predicting a shift with the S isotopic mass of $950 \mu\text{eV}/\text{amu}$ for the A exciton and $724 \mu\text{eV}/\text{amu}$ for the B exciton. Reflectivity and photoluminescence study of $^{\text{nat}}\text{Cd}^{32}\text{S}$ and $^{\text{nat}}\text{Cd}^{34}\text{S}$ performed by Kreingol'd et al. [222] shows that for anion isotope substitution the ground state ($n = 1$) energies of both A and B excitons have a positive energy shifts with rate of $\partial E/\partial M_S = 740 \mu\text{eV}/\text{amu}$. Results of Meyer et al. [230] are consistent with a shift of $\sim 710 \mu\text{eV}/\text{amu}$ for both A and B excitons. Finally, it is interesting to note that the shift of the exciton energies with Cd mass is $56 \mu\text{eV}/\text{amu}$ [229], an order of magnitude less than found for the S mass.

The present knowledge of the electronic band structure of Si stems from experimental observation of electronic transitions in transmission, reflectivity, or cyclotron resonance, on the one hand, and theoretical calculations, e.g. those based on pseudopotential or $\vec{k} \cdot \vec{p}$ methods (for details see [231 - 235] and references therein). In this manner it has been established that the fundamental, indirect band gap of Si occurs between the Γ_8^+ valence band maximum and the Δ_0 conduction band minima along (100).

Recently, Lastras-Martinez et al. [233] performed ellipsometric measurements on isotopically enriched ^{28}Si and ^{30}Si and deduced the isotopic dependence of E_1 from the analysis of the data in reciprocal (Fourier inverse) space. However, these measurements did not resolve (see, also [226]) the nearly degenerate E'_0 and E_1 transitions and the isotopic shift was assigned solely to the

stronger E_1 transitions (see, however, Fig. 36). We should add that in papers [235] very recently was studied the dependence of indirect band gap in Si on the isotopic mass. Photoluminescence and wavelength-modulated transmission spectra displaying phonon assisted indirect excitonic transitions in isotopically enriched ^{28}Si , ^{29}Si , ^{30}Si as well as in natural Si have yielded the isotopic gap E_{gx} which equals 1213.8 ± 1.2 meV. This is purely electronic value in the absence of electron-phonon interaction and volume changes associated with anharmonicity (for details see [235] and below).

Returning to Fig. 36, we can see that the spectrum contains two characteristic signatures, attributed to the excitonic transitions across the E'_0 and E_1 gaps. Isotopic dependence of the E'_0 and E_1 is displayed in Fig. 36, where the photo-modulated reflectivity spectra of ^{28}Si , ^{29}Si , and ^{30}Si are shown for the spectral range $3.3 \leq E \leq 3.58$ eV. The E'_0 and E_1 excitonic band gaps determined in paper [235] from the line-shape analysis. Linear least-squares fit yielded the corresponding isotopic dependences $E'_0 = (3.4468 - 0.03378 M^{-1/2})$ eV and $E_1 = (3.6120 - 0.6821 M^{-1/2})$ eV. In concluding, we should note that the spin-orbit interaction depends in Ge in contrast to that in Si [235].

As is well known ago, the fundamental energy gap in silicon, germanium, and diamond is indirect (see, e.g. [232]). While the conduction band minima in Si and diamond are located at the Δ point along $\langle 100 \rangle$, with Δ_6 symmetry, those of germanium with L_6^+ symmetry occur at the $\langle 111 \rangle$ zone boundaries [235]. The onset of the absorption edge corresponds to optical transition from the Γ_8^+ valence band maximum to the L_6^+ conduction band minima in Ge, and the Δ_6 in Si and diamond; for wavevector conservation, these indirect transitions require the emission or absorption of the relevant phonons. In Si and C, transverse acoustic (TA), longitudinal acoustic (LA), transverse optic (TO), or longitudinal optic (LO) phonons of Δ symmetry must be simultaneously emitted or absorbed. In Ge (see, also above), the wavevector conserving phonons are TA, LA, TO or LO phonons with L symmetry. At low temperatures, these indirect transitions are assisted by phonon emission. In this case we should expect at low temperatures four excitonic derivative signatures at photon energies $E_{gx} + \hbar\omega_{\vec{q},j}$ in modulated transmission experiments and in photoluminescence at the photon energies $E_{gx} - \hbar\omega_{\vec{q},j}$. Here E_{gx} is the excitonic band gap and j corresponds to a wave vector preserving phonon. In Fig. 37 - A the photoluminescence and wavelength - modulated spectra of ^{30}Si ($M = 2.81$ amu) are displayed; the labels $n = 1$ and 2 designate the ground and the first excited states of the indirect TA and TO excitons. From the energies of the photoluminescence and wavelength-modulated excitonic signatures in all isotopic specimens (see [235]) cited authors deduce E_{gx} as well as the energies of the participating TO, LO and TA phonons, shown in Fig. 37 - B as function of $M^{-1/2}$. The excitonic band gap data are fitted well with expression $E_{gx}(M) = E_{gx}(\infty) - CM^{-1/2}$, yielding $E_{gx}(\infty) = (1213.8 \pm 1.2)$ meV and $C = (313.7 \pm 5.3)$ meV/amu. A linear fit in M can be made over small range of available masses (see, Fig. 37 - B) with a slope $(\partial E_{gx}/\partial M)_{P,T} = 1.01 \pm 0.04$ meV/amu, which agrees with the results of bound exciton photoluminescence of Karaickaj et al. [234]. The experiments in papers [235] also indicate that separation of the $n = 2$ and $n = 1$ excitons

is isotope mass independent, implying, according these authors, the excitonic binding energy is independent on isotope mass within experimental error. In concluding this part we should note that recent high - resolution spectroscopic studies of excitonic and impurity transition in high - quality samples of isotopically enriched Si have discovered the broadening of bound exciton emission (absorption) lines connected with isotope - induced disorder as well as the depend of their binding energy on the isotope mass [234, 235]. The last effect was early observed on the bound excitons in diamond [236, 237], and earlier on the free excitons [238] in $\text{LiH}_x\text{D}_{1-x}$ mixed crystals (see, e.g. [151] and references therein).

4.4. Effects related to isotopic disorder.

4.4.1. Thermal conductivity.

In insulators and semiconductors (at $T < \theta_D$) the thermal conduction is effected by phonons, predominantly acoustic ones [239]. Thermal conductivity of crystals has been subject of many experimental theoretical studies (see, e.g. reviews and monographs [195, 239 - 246]). The first experimental results (see, e.g. [243]) have already pointed out the existence of maximum of the thermal conductivity coefficient k_m at about $T \approx 0.05 \theta_D$, where θ_D is the Debye temperature. The growth of k at low temperatures has been related to phonon scattering due to Umklap (U -) - type processes [245; 26]. In the vicinity of k_m thermal conductivity is quite sensitive to impurities and defects in the specimen. The scattering of phonons dynamic isotope disorder is independent of temperature and lattice anharmonicity. The role of isotopes as an additional channel of phonon scattering and their influence on thermal conductivity were first theoretically studied by Pomeranchuk [247] in 1942, and were experimentally studied using Ge in 1958 [248]. According to the results of the latter reference, for a Ge specimen (having 95.8% ^{74}Ge), a threefold growth of the thermal conductivity coefficient as compared to the specimen of germanium with natural isotope composition was observed. Later, the influence of isotopes on diamond thermal conductivity was studied many times [249 - 251].

It is generally assumed (see, e. g. [26]) that at not too high temperatures, the dominant interacting among phonons involve three phonons. In a "normal" (N -) process the wave vectors \vec{q} of the phonons are conserved and such process tend to restore a disturbed phonon distribution to one which can be described as a displaced Planck distribution (see, e.g. Fig. 5.2 in [242]) which is unaffected by N - processes and corresponds to a heat flow. By themselves, therefore, N - processes would not lead to a thermal resistance.

In Umklap (U -) - process [245] the wave vectors are not conserved and, as in other resistive processes, they tend to restore a disturbed phonon distribution to the equilibrium Planck distribution which corresponds to zero heat flow, and thus lead to a finite conductivity (for more details, see, review [26]). The Debye expression [252] for the conductivity $k(T)$ is derived from an adoption of the simple kinetic theory

$$k(T) = \frac{1}{3} \langle v_{ph} \rangle \ell_{ph}(T) C_p(T), \quad (114)$$

where $\langle v_{ph} \rangle$ is an average phonon velocity, $\ell_{ph}(T)$ their mean free path and $C_p(T)$ the corresponding specific heat (for diamond see [253]). A theory of $k(T)$ requires basically the calculation of

$$\ell_{ph}(T) = \tau_{ph}(T) \langle v_{ph} \rangle \quad (115)$$

a rather formidable task since several scattering mechanisms (normal -, u - processes, boundary of sample, isotope scattering) [26] contribute to determining the mean free path. In formula (115) $\tau_{ph}(T)$ is the phonon relaxation time. The simplest of these mechanisms, and the one that can be varied for a given material of the acoustic phonons by isotopic mass fluctuations. This scattering is equivalent to Rayleigh scattering (of photons) at point defect. Within Debye approximation, we will have

$$k(T) = \frac{k_B}{2\pi\nu} \left(\frac{k_B}{h} \right)^3 T^3 \int_0^{\frac{\theta_D}{T}} \tau(x) \frac{x^4 e^x}{(e^x - 1)^2} dx. \quad (116)$$

In last expression k_B is the Boltzmann constant. Klemens [239] was the first to try to take the role of N - processes into account. Using perturbation theory Klemens [239] developed the following expression for the scattering rate $\tau_{isotope}^{-1}$:

$$\tau_{isotope}^{-1} = \frac{x(x-1)V_0}{4\pi\langle v_{ph} \rangle^3} \left(\frac{\Delta M}{M} \right)^2 \omega^2, \quad (117)$$

where V_0 is a volume per atom (for diamond $5.7 \cdot 10^{-24} \text{ cm}^3$) and ω is phonon frequency. Callaway approach [244] successfully introduces normal phonon scattering (τ_N^{-1}) and resistive scattering (τ_R^{-1}) (see formula (4.51) in [26]).

In Fig. 38 present the results of Wei et al. [251]. The solid curves are the results of fitting the Callaway theory [244], using a single set of fitting parameter. In this paper, Wei et al. have measured a record thermal conductivity of $410 \text{ Wcm}^{-1}\text{K}^{-1}$ at 104 K for a 99.9% ^{12}C enriched diamond. These authors predict that a 99.999% ^{12}C diamond should have a peak value of thermal conductivity exceeding $2000 \text{ Wcm}^{-1}\text{K}^{-1}$, at about 80K, assuming, of course, that is not limited by point defect scattering mechanisms other than minority isotopes. Similar results have very recently been reported by Olson et al. [250]. We should stress that none of the currently existing theories accurately takes into account all the possible scattering processes.

Thermal conductivity studies have also performed on very highly enriched, ultra - pure ^{70}Ge (see, reviews [26, 27]). The maximum value of $k_m = 10.5 \text{ kWm}^{-1}\text{K}^{-1}$ was observed, in the vicinity of $T = 16.5 \text{ K}$, for the ^{70}Ge specimen of 99.99% purity, which is significantly higher than the value for sapphire ($6 \text{ kWm}^{-1}\text{K}^{-1}$ around T_m 35K) and comparable to the value for silver ($11 \text{ kWm}^{-1}\text{K}^{-1}$ near $T_m = 15.4\text{K}$). Comparison of experimental results shows [256] that, at its maximum (see, e.g. Fig. 6^a [205]), the thermal conductivity of the $^{70/76}\text{Ge}$ (91.91%) specimen is 14 times less than that of ^{70}Ge (91.91%). An increase in k reaches however, only 30% at $T = 300\text{K}$ (see, also [26, 27]).

The thermal conductivity of monoisotopic and isotopically mixed specimens of silicon crystals has been studied in following papers [257 - 260]. Since the most detailed results have been obtained by the authors of [259], we restrict ourselves to their consideration. It is well - known that natural silicon con-

sists of three isotopes: ^{28}Si ($\sim 92\%$), ^{29}Si ($\sim 5\%$), and ^{30}Si ($\sim 3\%$). The use of monoisotopic silicon (for example ^{28}Si) can substantially reduce the value of dissipated energy scattered in electronic elements made of silicon (e.g. in the memory of electronic computers [261]). The results studies of the thermal conductivity of monoisotopic and isotopically mixed crystals are shown in Fig. 39. According to the results presented in this Fig., for SI284 specimen $k = 237(8) \text{ Wm}^{-1}\text{K}^{-1}$ at 300K, whereas for the SINI (natural Si) specimen it is equal to $150 \text{ Wm}^{-1}\text{K}^{-1}$. This means that at 300K the thermal conductivity of a monoisotopic ^{28}Si specimen grows, as compared to the natural silicon, by 60 % (later - 10%, see, erratum). At the same time, at about 20 K (in the vicinity of the maximum of the silicon thermal conductivity curve) k reaches the value of $30000 \pm 5000 \text{ Wm}^{-1}\text{K}^{-1}$, which is 6 times higher the value $k = 5140 \text{ Wm}^{-1}\text{K}^{-1}$ for natural specimen (ee, also [241]).

The thin solid and dashed lines in Fig. 39 correspond to the results of theoretical computations of thermal conductivity for monoisotopic specimen SI284 and for a specimen with natural silicon isotope composition. In these calculations, the model of the Ge thermal conductivity developed in [256] with modified Debye temperature and phonon mean free path has been used. For fitting, the authors have used the low - temperature results, where the thermal conductivity is described by the T^3 law. Calculations presented in Fig. 39 were performed, for the natural specimen, for free mean path equals 5.0 mm (dashed line). For comparison, let us point out that in Ref. [257] the analogous quantity was equal to 5.7 mm, and for isotopically pure SI284 specimen the corresponding value was 14.0 mm (thin solid line). As seen from Fig. 39, there is agreement between theory and experiment, which has also been mentioned by the authors of [259] themselves. They have also pointed out good agreement between their experimental results and calculations made in [262], except for the domain of U - processes. Beside that, Ruf and co - authors have mentioned an unsatisfactory agreement between theory and experiment in the domain of high - temperatures (300 - 400K), especially for the specimen with natural isotope composition. They think that this disagreement can occur due to fundamental reasons that require further study. In particular, taking into account the fine structure of the nonequilibrium phonon distribution function could bring theoretical and experimental results much closer. A qualitative comparison of the influence of the isotope effect on the thermal of germanium, silicon and diamond is given in Table 19.

In concluding we should remark, that until recently all theories on thermal conductivity had a strongly phenomenological flavor, making use of the relaxation time approximation. In recent years, considerable progress towards an ab initio theory has been made [262; 263]. These authors used two - and three - body potentials obtained by fitting phonon dispersion relations and related the anharmonic properties with a single average Grüneisen parameter. In this manner they determined the third - order coupling coefficients for all possible three - phonon combinations. They then solved iteratively the Boltzmann equation for phonon transport without using the relaxation - time approximation. A scattering time must, however, still be used to describe boundary scattering in

the lowest temperature region. In this manner they reproduced rather well the thermal conductivities of Ge, Si and diamond and the observed isotope effects (for details see [262; 263]).

4.4.2. Disorder - induced Raman scattering.

The frequencies of vibrational modes in a solid depend on the interatomic forces and the atomic masses. By changing the mass of atoms by isotopic substitution the frequencies of modes are changed in a small but characteristic way that can be monitored by Raman spectroscopy. In isotopically pure crystals the width Γ_0 of the Raman line is determined - aside from experimental resolution - by the phonon lifetime which is governed by the spontaneous anharmonic decay into phonon of lower energy [239]. In an isotopically disordered material an additional contribution $\Gamma_{isotope}$ to the linewidth comes from the elastic scattering of phonons via mass fluctuation and has been observed for many semiconductors (see, review [27] and reference therein). Line shift and line broadening are theoretically obtained as real and imaginary parts of a complex self - energy which can be calculated in the framework of a coherent potential approximation (CPA) in the case of weak phonons scattering [26]. This theory describes, for example, frequency shift and line broadening very well in isotopically disordered diamond [264], Ge [265] and α - Sn [266]. A mass perturbation theory of the harmonic lattice dynamics for calculating $\Gamma_{isotope}$ has been developed by Tamura and applied to Ge [267], GaAs and InSb [268]. For the complex self - energy of the Raman phonon of a semiconductor with diamond structure, the second - order term ($n = 2$) contains the real part [269, 26]

$$\Delta_2(\omega, x) = \frac{g_2(x)}{4} \omega \left(\frac{1}{6N_c} \right) \sum_i \omega_i \frac{\omega - \omega_i}{(\omega - \omega_i)^2 + \gamma^2} \quad (118)$$

and the imaginary part (see, also [267, 268])

$$\Gamma_2(\omega, x) = \frac{g_2(x)}{4} \omega \left(\frac{1}{6N_c} \right) \sum_i \omega_i \frac{\gamma}{(\omega - \omega_i)^2 + \gamma^2}. \quad (119)$$

In the last two formulae N_c is the number of unit cells. For $\gamma \rightarrow 0$ Eq. (119) simplifies to a sum over δ - functions, which represents the one - phonon density of state $\rho(\omega)$ (compare to [268]),

$$\Gamma_2(\omega, x) = \Gamma_{iso} = \tau_{iso}^{-1} = \frac{\pi}{6} \omega^2 g | \vec{e} | \rho(\omega). \quad (120)$$

From this relation we can see, that Γ_{iso} depends on three factors:

- i) the relative mass variance g_2 ;
- ii) the phonon density of states $\rho(\omega)$ at the frequency ω of the Raman mode, and
- iii) a relevant phonon eigenvector \vec{e} .

4.4.2.1. Disorder shift and broadening of the lines in the Raman spectra.

In modern language, as say above, phonons are referred to as quasiparticles, with a complex self-energy $\Sigma = \Sigma_r + i\Sigma_i$ induced in insulators (semiconductors) by anharmonic phonon-phonon interactions and in crystals with several isotopes of a given element also by isotopic mass disorder. In metals and heavily doped semiconductors one must also take into account the self-energy which corresponds to the interaction of the phonon with the conduction electrons. The

purpose of this section is to discuss the isotopic disorder contributions to the self-energy of phonons, in the first step in semiconductors of the tetrahedral variety with special emphasis on the quantum effects observed at low temperatures (especially in diamond - where isotopic effects dominates over the anharmonic ones - as well as in germanium where anharmonic effects are larger [26]).

The definition of the average mass $\bar{m} = \sum_i c_i m_i$ implies that $g_1 = 0$. In

further discussion we display a compilation of the disorder-induced self-energies for the Raman phonons of elemental and compound crystals (diamond, Si, Ge, α -Sn and $\text{LiH}_x\text{D}_{1-x}$, 6H-SiC polytype) which have been obtained either by Raman spectroscopy or from theoretical calculations by several research groups during the last two decades. Raman studies that address the variation of the self-energy with the isotopic composition have been conducted for $\text{LiH}_x\text{D}_{1-x}$ (see, for example review [214]), diamond [204, 264, 270, 271], and Si [272]. The coherent potential approximation (CPA) has been employed for diamond [264, 270] and Si [272], while ab initio electronic structure based calculations have been performed for diamond and Ge [273].

Fig. 40 displays the Raman frequencies of diamond versus the ^{13}C concentration. The points (open symbols) represent experimental values. The dashed curve represents the approximately linear dependence expected in the VCA. The upward curvature of the experimental data (with respect to the VCA line) clearly demonstrates the existence of an isotopic-disorder-induced self-energy as emphasized by the solid line, which is a fit with Eq. (2.39) for $n = 2, 3$ of Ref. [26]. It is difficult to see with the naked eye in Fig. 40 the asymmetric behavior versus x , which may arise from third-order perturbation terms. The asymmetry appears, however, rather clearly when the difference between the measured (or the calculated) behavior and the VCA line is plotted, as shown in Fig. 41. In this figure, the solid line also represents the fit to all experimental data, the dot-dashed line represents CPA calculations while the dotted line is a fit to the asterisks which indicate points obtained in the ab initio calculations [192; 201]. All data in Fig. 44 show a similar asymmetric behavior, with a maximum of $\Delta_{\text{dis}}(x)$ at $x \approx 0.6$. These results allows us to conclude that the real part of the self-energy due to isotopic disorder is well understood for these systems, including the superposition of second-order and third-order perturbations terms in the case of the diamond. Similar degree of understanding has been reached for $\Gamma_{\text{dis}}(x)$ as shown in Fig. 42. The x position of the maxima of Δ_{dis} and Γ_{dis} determined from the experimental data agree with those obtained by perturbation theory [Eq. (2.42) of Ref. [26]] and also with the CPA and ab initio calculations (details see [269]). Concerning the other elemental semiconductors, detailed experimental results with sufficient values of x to reach quantitative conclusions of the type found for diamond, are only available for Si. These data for Si are shown in Figs. 43 and 44. (filled circles) together with the results of CPA calculations (filled squares). The latter show for Δ_{dis} a clear asymmetry with a maximum at $x_{\text{max},\Delta} \approx 0.56$. The quality and the number of the experimental points are not sufficient to conclude that an asym-

metry exists but they cannot exclude it either. The measured absolute values of Δ_{dis} almost (not quite) agree within error bars with the calculated ones. The corresponding experimental values of $\Gamma_{\text{dis}}(x)$ (see Fig. 44) are about a factor of 2 lower than the calculated ones, although both show the asymmetric behavior ($x_{\text{max},\Gamma} \approx 0.62$) predicted by theory. The reason for the discrepancy between the calculated and measured Γ_{dis} is to be sought in the mechanism responsible for it in Si [69]. Within harmonic approximation $\Gamma_{\text{dis}} = 0$ for Si, Ge and α -Sn, because the Raman frequency is at the maximum of the spectrum and thus corresponds to zero density of one-phonon states. The rather small, but not negligible, observed value of Γ_{dis} results from DOS induced at the Γ point by the anharmonic interactions responsible for the linewidths of the isotopically pure crystals. Thus, the widths observed for Si, as well as for Ge and α -Sn, correspond to fourth-order (twice disorder and twice anharmonicity) and higher-order terms.

As was shown in the papers [268, 269], the isotope effects of a disordered sublattice in a compound is different from that for the corresponding monatomic crystal. Widulle et al. apply Eqs. (2.50a) and (2.50b) of Ref. [26] to the Raman spectroscopic results on a variety of $^{\text{nat}}\text{Si}^{12}\text{C}_{1-x}^{13}\text{C}_x$ polytypes, recently reported by Rohmfeld et al. [275]. They have performed a fit Eq. (2.40) for $n = 2, 3$ of Ref. [26] to the linewidths of the transverse optic (TO) modes of the 6H-SiC polytype measured in [275] for ^{13}C concentration ranging from $x = 0.15$ to $x = 0.40$ Fig. 45). The fit performed in Ref. [275] was based on the asymmetric curve obtained by CPA calculations for diamond [264]. This curve was first fitted to the data points of the TO (2/6) mode and further adjusted to the TO (0) and TO (6/6) modes by multiplication with the constant eigenvectors. Instead, authors [269] have considered each TO mode separately and performed fits with Eq. (2.40) for $n = 2, 3$ of Ref. [26] in the same manner as for elemental semiconductors (see above). Widulle et al. used, however, parameters appropriate to SiC, not to diamond. In this way, they conclude that the behavior of Γ_{dis} versus x is asymmetric (Fig. 45). This fact cannot, according to Widulle et al, derived from the data of the results paper [275]. The latter can be fitted equally with either a symmetric or an asymmetric curve.

As has been mentioned many times, the isotopic disorder in the crystal lattice lifts the forbiddenness imposed by the quasiimpuls conservation law, thus allowing a contribution to the half - width of the scattering line from other phonons from the domain with the maximum density of states, especially from the TO branches of Ge. The two structures observed in the spectrum of first - order Raman scattering near 275 and 290 cm^{-1} correspond to the maximum of the density of states of TO phonons (see [27] and references therein), which become active because of the violation of the quasi - momentum conservation law by the isotopic disorder in the crystal (see, for instance Fig. 20 in [205]). The effect of the development of an additional structure in Raman scattering spectra was observed relatively long ago [276] in isotopically mixed $\text{LiH}_x\text{D}_{1-x}$ (Fig. 46). The effects caused by isotopic disorder in the crystal lattice in isotopically mixed are analogous to those described above (see, also [205]) There exist, however, principal differences. In contrast to Ge and C, in which

the first - order spectra exhibit a one - mode character, the second - order spectra of $\text{LiH}_x\text{D}_{1-x}$ crystals have one - and two - mode characters for $\text{LO}(\Gamma)$ phonons, and also contain a contribution from the local excitation at small values of x . Fig. 46 demonstrates the dependence of the half - width of the line of $\text{LO}(\Gamma)$ phonons in light - scattering spectra on the concentration of isotopes. One clearly sees a substantial growth (by factor 2 - 4) of the half - width of the line with increasing concentration of isotopes, as well as the existence of a short - wavelength structure that has already been related in Ref. [276] to the excitation of TO phonons in isotopically disordered crystal lattice (for more details see [277]).

To conclude this part of our review, we should note that in contrast elemental semiconductors, where isotope scattering potential is weak, in the case isotope-mixed crystals $\text{LiH}_x\text{D}_{1-x}$ isotope scattering potential is very strong and CPA approximation in such simple version does not describe the Raman spectra of these crystals.

4.4.3. Effects of isotope randomness on electronic properties and exciton transition.

As follows from Fig. 34, excitons in $\text{LiH}_x\text{D}_{1-x}$ crystals display a unimodal character, which facilitates the interpretation of their concentration dependence. Figure 47 shows the concentration dependence of the energy of interband transitions E_g . Each value of E_g was found by adding together the energy of the long-wave band in the reflection spectrum and the binding energy of the exciton. The latter was found from the hydrogen-like formula using the experimental values of the energies levels of 1s and 2s exciton states. We see that the 100% replacement of hydrogen with deuterium changes E_g by $\Delta E_g = 103 \text{ meV}$ at $T = 2 \text{ K}$ (see, e.g. [221]). This constitutes 2% of the energy of the electron transition, which is two orders of magnitude greater than the value corresponding to the isotopic replacement of atomic hydrogen with deuterium reported earlier [278].

The nonlinear concentration dependence of E_g can be sufficiently well approximated with a second order polynomial

$$E_g(x) = E_b + (E_a - E_b - b)x - bx^2, \quad (121)$$

where E_a , E_b are the values of E_g for LiD and LiH respectively, and b is the curvature parameter equal to 0.046 eV. This result generally agrees with the published data (see also Elliott and Ipatova [279] and references therein). For comparison let us indicate that in the case of isotopic substitution in germanium the energy E_g depends linearly on the isotopic concentration for both direct (E_0 , $E_0 + \Delta_0$, $E_1 + \Delta_1$) and indirect electron transitions [280]. Unfortunately, today there is no information on the form of the function $E_g \propto f(x)$ for isotopic substitution in C, ZnO, CdS, CuCl, Cu_2O , GaAs, GaN, Si, etc. crystals, although, as noted above, the values of E_g have been measured for isotopically pure crystals. However, we should add, that isotopic substitution in Ge leads not only to the shift of the luminescence spectrum, but also to the nonlinear concentration

dependence of the emission line half - width, as in the case of lithium hydride (see, below) was attributed to isotopic disordering of the crystal lattice [281].

According to the results depicted on Fig. 88, the addition of deuterium leads not only to the short-wave shift of the entire exciton structure (with different rates for 1s and 2s states [221], but also to a significant broadening of the long-wave exciton reflection line. This line is broadened 1.5 - 3 - fold upon transition from pure LiH to pure LiD. The measure of broadening was the halfwidth of the line measured in the standard way (see e.g. [282]) as the distance between the maximum and the minimum in the dispersion gap of the reflection spectrum, taken at half-height. The concentration dependence of the halfwidth (ΔE^R) of the long-wave band in the exciton reflection spectrum at 2 K is shown in Fig. 48. Despite the large spread and the very limited number of concentrations used, one immediately recognizes the nonlinear growth of ΔE^R with decreasing x . A similar concentration dependence of ΔE^R in the low-temperature reflection spectra of solid solutions of semiconductor compounds A_2B_6 and A_3B_5 has been reported more than once (see e.g. the review [279] and references therein). The observed broadening of exciton lines is caused by the interaction of excitons with the potential of large-scale fluctuations in the composition of the solid solution. Efros and colleagues (see e.g. [283]) used the method of optimal fluctuation [284] to express the formula for the concentration dependence of the broadening of exciton reflection lines:

$$\Delta E^R = 0.5\alpha \left[\frac{x(1-x)}{Nr_{ex}} \right]^{1/2}. \quad (122)$$

where $\alpha = dE_g/dx$; r_{ex} is the exciton radius which varies from 47 Å to 42 Å upon transition from LiH to LiD [49]. The value of coefficient α was found by differentiating Eq. (121) with respect to x - that is, $dE_g/dx = \alpha = E_a - E_b - b + 2bx$. The results of calculation according to Eq. (122) are shown in Fig. 48 by a full curve.

The experimental results lie much closer to this curve than to the straight line plotted from the virtual crystal model. At the same time it is clear that there is only qualitative agreement between theory and experiment at $x > 0.5$. Nevertheless, even this qualitative analysis clearly points to the nonlinear dependence of broadening on the concentration of isotopes, and hence to the isotopic disordering. Since isotopic substitution only affects the energy of optical phonon, and, as a consequence, the constant of exciton-phonon interaction (in the first place, the Fröhlich interaction g_F^2), the nonlinearity of functions $\Delta E_g \propto f(x)$, $\Delta E^R \propto f(x)$ is mainly related to the nonlinear behavior of $g_F^2 \propto f(x)$. In this way, the experimental study of the concentration dependence of the exciton-phonon interaction constant may throw light on the nature and mechanism of the large-scale fluctuations of electron potential in isotopically disordered crystals (see also [277]).

A principal matter for further theoretical development is the question concerning the effect of crystal lattice disordering on the binding energy E_B of Wannier-Mott exciton [151]. This problem has been treated theoretically in the papers of Elliott and coworkers [285, 286], where they study the effect of weak disordering on E_B (the disordering energy is comparable with E_B). The

binding energy indicated in the papers was calculated under the coherent potential approximation by solving the Bethe-Salpeter equation [290] as applied to the problem of Wannier-Mott exciton in disordered medium. One of the principal results of this paper [285] is the nonlinear dependence of E_B on the concentration. As a consequence, the binding energy E_B at half-and-half concentrations is less than the value derived from the virtual crystal model. The exciton binding energy is reduced because the energy E_g is less owing to the fluctuation smearing of the edges of the conduction and valence band. This conclusion is in qualitative agreement (although not in quantitative agreement, the discrepancy being about an order of magnitude (see also [285]) with the experimental results for the mixed crystal $\text{GaAs}_{1-x}\text{P}_x$ with $x = 0.37$, where the reflection spectra exhibited two exciton maxima (see also Fig. 34) used for finding the value of E_b (see Nelson et al. [287] and references therein). Let us add that the pivotal feature of the model of Elliott and coworkers is the short-range nature of the Coulomb potential (for more details see [49]).

Before the comparison of our experimental results with the theory developed by Elliott and Kanehisa, it would be prudent to briefly review main properties of their theoretical model. According to Ref. 285 this model considers an exciton with a direct gap of a semiconductor alloy. Such a system consists of an electron (particle 1) in the conduction band (c) with mass m_c and a hole (particle 2) in the valence band (v) with mass m_v . The problem of the exciton in disordered systems is to solve the Hamiltonian

$$H = \vec{p}^2/2m_c + \vec{p}^2/2m_v + u(\vec{r}_1 - \vec{r}_2) + V_c(\vec{r}_1) + V_v(\vec{r}_2), \quad (123)$$

with both the Coulomb interaction u and the potential V_ν due to disorder ($\nu = c, v$). Reference 362 neglected disorder - induced interband mixing. As it is well known, in place of the electron-hole coordinates, (\vec{r}_1, \vec{p}_1) and (\vec{r}_2, \vec{p}_2) , one may introduce the center-of-mass and relative coordinates, (\vec{R}, \vec{P}) and (\vec{r}, \vec{p}) to rewrite (123) as

$$H = \vec{p}^2/2m_r + u(\vec{r}) + \vec{P}^2/2M + V_c(\vec{R} + m_v \vec{r}/M) + V_v(\vec{R} - m_c \vec{r}/M), \quad (124)$$

where m_r and M are the reduced and total masses, respectively. Because of the random potential, the translational and relative degrees of freedom cannot be decoupled. This is essentially difficult when considering the two-body problem in a disordered system [288]. However, when the exciton state in question is well separated from other states so that the energy spacing is much larger than the translational width and disorder, one can forget about the relative motion and just apply any single-particle alloy theory (see, e.g. Ref. [289 and references therein) solely to their translational motion. For each exciton state the translational part of Hamiltonian in this case is

$$H_t = \vec{P}^2/2M + \bar{V}_c(\vec{R}) + \bar{V}_v(\vec{R}) \quad (125).$$

Here \bar{V}_c and \bar{V}_v are averages of V_c and V_v . This approach is very similar to the Born-Oppenheimer adiabatic approximation. Such situations hold in some mixed alkali halide crystals and probably A_2B_6 crystals. On the contrary, when the exciton binding energy is comparable to the disorder energy, the adiabatic approximation breaks down, and it is essential to take into account the effect of

disorder on both the translational and relative motions. This is the case with the Wannier-Mott exciton in A_3B_5 alloys, for which the Elliott and Kanehisa model was developed. In this case the solution task is to start from the independent electron and hole by neglecting u in (124) and then to take into consideration the Coulomb interaction between the average electron and average hole. A further simplified approach adopted in the literature [289] in solving the Bethe-Salpeter [290] equation is to suppose a free-electron-like one particle Green's function with a built-in width to allow for the random potential due to disorder. In the cited theoretical model, the average (or "virtual crystal") gap is given by

$$E_g^{vc}(x) = E_0 + (\delta_c - \delta_v)(x - 1/2), \quad (126)$$

where E_0 is average gap, δ_c , δ_v are the values of the fluctuation broadening of the conduction and valence bands, respectively. Reference [285] also assumed the Hubbard density of states for both the conduction and valence bands with width W_c and W_v , respectively, as well as similar dispersion in both bands. With this assumption the exciton binding energy has been calculated according to the CPA model (see, also [210]). It should be added here the key feature of the model developed in Ref. [285] is the short-range nature of the Coulomb potential.

The data from Table 17 and other published sources (see [49, 221, 277]) were used for plotting the energy E_B as a function of isotopic concentration x in Fig. 49. The values of binding energy E_B were calculated using the hydrogen-like formula (see below) with the energies of exciton levels of 1s and 2s states being found from the reflection spectra (see Fig. 34). Theoretical description of the binding energy of Wannier-Mott excitons as a function of x was based on the polynomial derived by Elliott and coworkers [285]:

$$E_b = E_b^{crys} - E_{bow} \left[\frac{1-W}{2U_0} \right] - E_{eff}, \quad (127)$$

$$E_{eff} = x(1-x) \frac{\delta_c \delta_v}{W}, \quad (128)$$

$$E_b^{crys} = U_0 + \frac{W}{2U_0} - W. \quad (129)$$

where $W = W_c + W_v$, and W_c and W_v are the widths of the conduction band and the valence band which are equal to 21 eV [291] and 6 eV [292, 293] respectively. Here E_{bow} is the curvature parameter found from the function $E_g \propto f(x)$; δ_c and δ_v are the magnitudes of the fluctuation smearing of the valence band and the conduction band edges, $\delta_c = 0.103$ eV and $\delta_v = -0.331$ eV. As follows from Fig. 49, these values of the parameters give a good enough description of the nonlinear dependence of the binding energy of Wannier-Mott exciton in disordered medium. This agreement between theory and experiment once again proves the inherent consistency of the model proposed by Kanehisa and Elliott, since the isotopic substitution affects the short-range part of the interaction potential.

In this way, the nonlinear dependence of the binding energy of Wannier-Mott exciton is caused by isotopic disordering of the crystal lattice. As is seen from Fig. 49 the exciton binding energy decreasing (relative linear law (VCA)-see dashed line in Fig. 49) in the vicinity of the middle mean concentration really calls out the fluctuated broadening of the edge of the conduction and valence bands. In accordance with the theoretical model the last reason gives

rise to the reduced E_g and there by the shallowing of the exciton levels and, respectively, the reduction of E_b (for more details see [151, 277]).

4.5. Zero - point vibration energy.

The short history of zero - point vibration energy can be found in Rechenberg's paper [294]. According to Rechenberg M. Panck used this conception at a Berlin meeting of German Physical Society at 1911 [295] after that it used numerously (see, e.g. [252, 296]). For the first time in solid state physics the conception of zero - point vibration energy probably have used by Fan [297] and for the interpretation of experimental results by Kreingol'd et al. [224, 225, 227], Cardona et al. (see, e.g. [298, 27]) as well as Agekyan and coworkers [201]. The classical definition of this conception have proposed by Baym [299]..." The minimum amount of kinetic energy coming from the uncertainty principle is called zero - point energy" (see, also [123]).

The effect of changing the atomic mass M is to change the phonon frequencies ω according to Equation (101)

$$\omega = \sqrt{\frac{\alpha}{M}}, \quad (101')$$

where α is a force constant characteristic of the phonon under consideration (see above). The change in atomic mass implies, at low temperatures (see below), a change in the average atomic displacement for each phonon mode. In the case of one atom per primitive cell the mean squared phonon amplitude $\langle u^2 \rangle$ is given by [284]:

$$\langle u^2 \rangle = \langle \frac{\hbar^2}{4M\omega} [1 + 2n_B(\omega)] \rangle = \langle \frac{\hbar}{4M^{1/2}\alpha^{1/2}} [1 + 2n_B(\omega)] \rangle, \quad (130)$$

where $n_B(\omega)$ is the Bose - Einstein statistical factor, ω is the frequency of a given phonon and $\langle \dots \rangle$ represents an average over all phonon modes. The average in r.h.s. of (130) is often simplified by taking the value inside $\langle \dots \rangle$ at an average frequency ω_D which usually turns out to be close to the Debye frequency. We should distinguish between the low temperature ($\hbar\omega \gg k_B T$) and the high temperature ($\hbar\omega \ll k_B T$) limits and see:

$$\begin{aligned} (\hbar\omega \gg k_B T), \quad \langle u^2 \rangle &= \frac{\hbar}{4M\omega_D} \sim M^{-1/2} \quad \text{independent of } T \text{ and} \\ (\hbar\omega \ll k_B T), \quad \langle u^2 \rangle &= \frac{k_B T}{2M\omega_D^2} \sim T \quad \text{independent of } M \end{aligned} \quad (131).$$

Using Eq. (130) we can find from last equations that $\langle u^2 \rangle$, the zero-point vibrational amplitude, is proportional to $M^{-1/2}$ at low temperatures: it thus decrease with increasing M and vanishes for $M \rightarrow \infty$. For high T , however, we find that $\langle u^2 \rangle$ is independent of M and linear in T (details see [26] and references therein).

The temperature and isotopic mas dependence of a given energy gap $E_g(T, M_i)$ can be described by average Bose-Einstein statistical factor n_B corresponding to an average phonon frequency θ_i as (see also [300, 298, 233])

$$E_g(T, M_i) = E_{bar} - a_r \left(\frac{M_{nat}}{M_i} \right)^{1/2} [1 + 2n_B], \quad (132)$$

where $n_B = 1/[\exp(\frac{\theta_i}{T}) - 1]$ and E_{bar} and a_r the unrenormalized (bare) gap and the renormalization parameter, respectively. In the low-temperature limit, $T \ll \theta_i$, equation (132) reduces

$$E_g(T, M_i) = E_{bar} - a_r \left(\frac{M_{nat}}{M_i} \right)^{1/2} \quad (132)$$

Here $E_g(T, M_i)$ is independent of temperature and proportional to $(1/M_i)^{1/2}$, whereas a_r is the energy difference between the unrenormalized gap ($M_i \rightarrow \infty$) and the renormalized value [297, 301].

In the high-temperature limit, $T \gg \theta_i$ and Eq. (132) can be written as

$$E_g(T, M_i) = E_{bar} - 2T \frac{a_r}{\theta}, \quad (133)$$

and $E_g(T, M_i)$ is independent of M_i [5]. The extrapolation of Eq. (133) to $T = 0K$ can be used to determine the unrenormalized gap energy E_{bar} , i.e., the value that corresponds to atoms in fixed lattice position without vibrations (frozen lattice [278]), from the measured temperature dependence of $E_g(T)$ in the high-temperature (i.e. linear in T) region. Fig. 50 shows the indirect gap of silicon T [303]. It is important to note that the experimental T range of Fig. 50 (confined to $T < \theta$) does not suffice to determine the asymptotic behavior for $T \rightarrow \infty$. The experimental range is usually limited (to 300K in Fig 50) by the broadening of optical spectra with increasing T . As already mentioned, the zero - point renormalization of a gap can also be estimated from the corresponding isotope effect. In the case of E_{ind} for silicon, a gap shift of - 1.04 meV/amu is found for $T \ll \theta$ [302]. On the basis of the Eq. (133), the isotope effect leads to a renormalization of 60 ± 1 meV for the E_{ind} in silicon, in reasonable agreement with the value ~ 57 meV found from the $E_{ind}(T)$ asymptote. The isotope shift, and the corresponding zero - point renormalization, have also been determined for the indirect gap of Ge (see Fig. 51 [26]). They amount to (at $T \simeq 6K$): isotope shift equals 0.36 meV/amu, renormalization equals -53 meV. The value of - 370 meV found for the zero - point renormalization of E_{ind} in diamond (see, Fig. 52) can be used to obtain the dependence on isotopic mass by means of the $M^{-1/2}$ rule (Eq.(132)) [27]

$$\frac{dE_{ind}(0)}{dM} = \frac{1}{2} \cdot 370 \cdot \frac{1}{13} = 14.2 \text{ meV/amu} \quad (134).$$

The last value is in excellent agreement with the value estimated above. A recent semiempirical LCAO calculation results in a renormalization of 600 meV [298], even larger than the experimental values. The value of the exciton energy shown in Fig. 52, 5.79 eV, can be compared with ab initio calculations of the indirect gap [27], which yield an indirect gap of 5.76 eV. This value must be compared with that from Fig. 52 adding the exciton binding energy ($5.79 + 0.07 = 5.86$ eV). This experimental gap value according to [27] is in rather good agreement with ab initio calculations. The agreement becomes considerably worse if the zero - point renormalization of 370 meV is not taken into account (5.48 vs. 5.76) All these arguments support the large zero - point renormalization found for the indirect gap of diamond.

Using Eq. (132) it can be written the difference in energy ΔE_g between a given energy gap in isotopically pure material (LiH) and its isotope analogue (LiD)

$$\Delta E_g = E_g(M_i) - E_g(M_{nat}) = a_r \left[1 - \left(\frac{M_{nat}}{M_i} \right)^{1/2} \right]. \quad (135)$$

As can be seen from Table 1 and results of [301] ΔE_g at 2K equals $\Delta E_g = 0.103$ eV and $E_g(\text{LiH}, T = 0K) = 5.004$ eV (linear approximation and $E_g(\text{LiH}, T = 300K) = 4.905$ eV then using Eq. (133) we obtain $a_r = 0.196$ eV. This

magnitude is very close (approximately 84%) to the value of 0.235 eV of zero (see Fig. 53) vibration renormalization of the energy band gap in LiH crystals (details see [301, 203]). Using Eq. (135) we obtain $\Delta E_g(\text{theor}) = 0.134$ eV that is very close, on the other hand, to observed experimental value equals 0.103 eV. The discrepancy between these values may be caused by the negligible contribution of the isotopic lattice expansion to the band gap renormalization as well as small temperature range. We should add, so far LiH and LiD have different temperature coefficients $\frac{dE_{g=1s}}{dT}(\text{LiH}) = 0.19 \text{ meVK}^{-1}$ and $\frac{dE_{g=1s}}{dT}(\text{LiD}) = 0.25 \text{ meVK}^{-1}$ [277], we may conclude that the isotope effect at high temperature is disappeared (Fig. 54 [303]) (see, also [304]).

Several groups have conducted low-temperature studies of the direct and indirect band gaps of natural and isotopically controlled Ge single crystals. Parks et al. [280] have used piezo - and photomodulated reflectivity spectra of four monoisotopic and one natural Ge crystals. These techniques do not require the extreme sample thinning which is necessary for optical-absorption measurements and the derivative nature of the spectra emphasizes the small changes. The excellent signal - to - noise ratio and the superb spectral resolution allowed a very accurate determination of the dependence of E_{DG} on isotopic mass. At very low temperatures an inverse square-root dependence accurately describes band-gap dependence $E_{DG} = E_{DG}^{\infty} + \frac{C}{\sqrt{M}}$.

A fit through five data points yields $E_{DG}^{\infty} = 959 \text{ meV}$ and $C = -606 \text{ meV}/\text{amu}^{1/2}$. Written as a linear dependence for the small range of isotopic masses, Parks et al. find $dE_{DG}/dA = 0.49 \text{ meV}/\text{amu}$, in perfect agreement with the results of other researchers [27]. Parks et al. also determined the isotope mass dependence of the sum of the direct gap and the split-off valence band (Δ_0) and find $d(E_{DG} + \Delta_0)/dA = 0.74 \text{ meV}/\text{amu}$. The experimental results can be compared to the Zollner et al. [298] calculations which are found to be of the correct order of magnitude. The theoretical estimates for the contributions of the linear isotope shifts of the minimum, indirect gaps which are caused by electron-phonon interaction, are too large by a factor of ~ 1.7 and for the smallest direct gap they are too large by a factor ~ 3.2 . The analogous results were obtained by Zhernov [305], who have criticized the approach of Cardona et al. in estimation of zero - point renormalization of the band gap.

5. Some modern application of the stable and radioactive isotopes.

5.1. Stable isotopes.

5.1.1. Traditional applications.

Present part is devoted to description of different applications of the stable isotope effect in solids. Capture of thermal neutrons by isotope nuclei followed by nuclear decay produces new elements, resulting in a very number of possibilities for isotope selective doping of solids [31]. There are presented different facilities which use in this reactor technology. The feasibility of constructing

reactors dedicated to the production of neutron transmuting doped (NTD) silicon, germanium (and other compounds) was analyzed in terms of technical and economic viability and the practicality of such a proposal is examined [30]. The importance of this technology for studies of the semiconductor doping as well as metal-insulator transitions and neutral impurity scattering process is underlined. The introduction of particle irradiation into processing of semiconductor materials and devices creates a new need for additional understanding of atomic-displacement-produced defects in semiconductors. The use of the isotopes in a theory and technology of the optical fibers we briefly considered too. For the first time it was shown also the influence of the isotopes on properties of the optical fibers. There is short description of theory and practice of semiconductor lasers. The discovery of the linear luminescence of free excitons observed over a wide temperature range has placed lithium hydride, as well as crystals of diamond in line as prospective sources of coherent radiation in the UV spectral range. For LiH isotope tuning of the exciton emission has also been shown [3].

In the next part we detail analyze the process of self-diffusion in isotope pure materials and heterostructure. Interest in diffusion in solids is as old as metallurgy or ceramics, but the scientific study of the phenomenon may probably be dated some sixth-seven decades ago. As is well-known, the measured diffusion coefficient depends on the chemistry and structure of the sample on which it is measured. We are briefly discussed the SIMS (secondary ion mass spectrometry) technique. In SIMS technique, the sample is bombarded by reactive ions, and the sputtered-off molecules are ionized in a plasma and fed into a mass-spectrometer. Self-diffusion is the migration of constituent atoms in materials. This process is mediated by native defects in solids and thus can be used to study the dynamics and kinetics of these defects. The knowledge obtained in these studies is pivotal for the understanding of many important mass transport processes such as impurity diffusion in solids (see, e.g. reviews [306 - 308] and monographs [309 - 310]). Another area of interest in a detailing understanding of the self - and foreign - atom diffusion behavior is self - and dopant diffusion in Si - Ge alloys. Dopant diffusion in Ge is not well understood [311] and accurate diffusion data are very limited [312]. Dopant diffusion in Ge and SiGe isotope multilayer structures would significantly improve our understanding of the mechanism of diffusion in Ge and SiGe alloys and how they change with alloy composition and strain. This information is important in particular for the integration of these materials in the next generation of electronic devices. The advances in the understanding of atomic - transport processes and defect reactions in semiconductors has contributed to the remarkable increase of computer speed and capacity over the last two decades. On the other hand, the higher computer power gives rise to more reliable and predictive theoretical calculations of the properties of point defects in semiconductors and hence also expedites their own technological evolution [313, 314]. Very perspective is isotope-based quantum computer. We should add here that the strength of the hyperfine interaction is proportional to the probability density of the electron wavefunction at the nucleus. In semiconductors, the electron wavefunction extends over large distances through the crystal lattice. Two nuclear spins can

consequently interact with the same electron, leading to electron-mediated or indirect nuclear spin coupling. Because the electron is sensitive to externally applied electric fields, the hyperfine interaction and electron-mediated nuclear spin interaction can be controlled by voltages applied to metallic gates in a semiconductor device, enabling the external manipulation of nuclear spin dynamics that is necessary for quantum computation in quantum computers (for details see [3, 30]).

5.1.1.1. Diffusion.

One of the fundamental processes occurring in all matter is the random motion of its atomic constituents. In semiconductors much has been learned in recent years about the motion of host and impurity atoms as well as native defects such as vacancies and interstitials. A number of excellent review papers [306 - 308] and monographs [309 - 310] have been written. When a concentration gradient dN/dx is introduced, random motion leads to a net flux of matter J which is proportional to the gradient (Fick's first law, see, e.g. [315])

$$J = -DdN/dx \quad (136).$$

The diffusion coefficient D can in many (though not in all) cases be described by a thermally activated constant (see, also [316]):

$$D = D_0 \exp(-E/k_B T). \quad (137)$$

Impurity diffusion in semiconductors plays a key role in the fabrication of electronic devices. For example, diffusion can be utilized as a desirable process enabling the introduction of dopant impurities into areas defined by a mask on a semiconductor wafer. Diffusion can act also as a detrimental process broadening narrow impurity implantation profiles or rapidly admitting diffusion of undesirable impurities. There exists a very extensive literature on diffusion studies for most semiconductors. The field is extremely active especially for the semiconductors which have become important recently for high-temperature electronics (e.g. C; SiC), light emitting devices working in the green and blue range of the visible spectrum (e.g. ZnSe, GaN) and IR records (Ge).

As simple as diffusion may appear to be, at least conceptually, there still exist many basic unanswered questions. Results from supposedly identical experiments conducted by different groups often scatter by significant factors. This clearly indicates that there are still hidden factors which need to be determined. Even for the most thoroughly studied crystalline solid, Si (see, e.g. [311, 312] references therein), we still do not know with certainty the relative contributions of vacancies and interstitials to self- and impurity diffusion as a function of temperature, the position of the Fermi level, and external effects such as surface oxidation and nitridation (see also [313]).

Fuchs et al. [317] presented results of a very accurate method to measure the self-diffusion coefficient of Ge which circumvents many of the experimental problems encountered in the conventional methods. Fuchs et al used Ge isotopic heterostructures (stable isotope), grown by molecular-beam epitaxy (MBE). In general, isotope heterostructures consist of layers of pure (e.g. ^{70}Ge , ^{74}Ge) or deliberately mixed isotopes of a chemical element. In this paper Fuchs et

al. [317] used the isotope heterostructure growing on the Ge substrate. At the interface only the atomic mass is changing, while (to first order) all the other physical properties stay the same. In the as-grown samples, this interface is atomically flat with layer thickness fluctuations of about two atomic ML [318]. Upon annealing, the isotopes diffuse into each other (self-diffusion) with a rate which depends strongly on temperature. The concentration profiles were measured with SIMS (secondary-ion-mass spectroscopy), after pieces of the same samples have been separately annealed at different temperature. This allows an accurate determination of the self-diffusion enthalpy as well as the corresponding entropy. The isotopic heterostructures are unique for the self-diffusion studies in several respects.

1) The interdiffusion of Ge isotopes takes place at the isotopic interface **inside** the crystal, unaffected by possible surface effects (e.g., oxidation, strains and impurities) encountered in the conventional technique (see Fig. 55).

2) One sample annealed at one temperature provides five more or less independent measurements: Germanium consists of five stable isotopes. Their initial respective concentrations vary for the different layers of the as-grown isotope heterostructure. After annealing, the concentration profile of each of the five isotopes can be analyzed separately to obtain five data points for each annealing temperature. Tan et al. [319] were the first to make use of GaAs isotope superlattice ($^{69}\text{GaAs}$; $^{71}\text{GaAs}$) on a Si-doped substrate to study Ga self-diffusion. Unfortunately however, their analysis was only partially successful because native defects and silicon out diffusion from the doped substrate into the superlattice obscured their results (see, also [317]).

Contrary to the short period superlattices required for Raman experiments, Fuchs et al. [317] used sufficiently thick layers to access \sqrt{Dt} products of one to several micrometers. This first studies as was mentioned above will focus on Ge self-diffusion in undoped material. They are working with bilayers of ^{70}Ge and ^{74}Ge (each 1000 or 2000 Å thick) which were grown by MBE on a natural substrate. Disregarding for the moment the small differences in diffusivity caused by different isotopes masses (see, also [320]), they expected the Ge isotopes to diffuse symmetrically into each other following complementary error functions. There exists no net flow of Ge atoms and the atomic concentrations add up to unity at every point: $[^{70}\text{Ge}] + [^{74}\text{Ge}] = 1$. The individual profiles are described by

$$[^{70}\text{Ge}]_x = 0.5[^{70}\text{Ge}]_0 \left\{ 1 - \text{erf} \left(x/2\sqrt{Dt} \right) \right\}. \quad (138)$$

$$[^{74}\text{Ge}]_x = 0.5[^{74}\text{Ge}]_0 \left\{ 1 - \text{erf} \left(-x/2\sqrt{Dt} \right) \right\}. \quad (139)$$

The interface is located at $x = 0$ and $[^{70}\text{Ge}]_0 = [^{74}\text{Ge}]_0 = 4.4 \cdot 10^{22} \text{ cm}^{-3}$.

For the experiments Fuchs et al. [317] have chosen five diffusion temperatures and have adjusted the times so as to obtain similar \sqrt{Dt} products. Fig. 56 shows SIMS results for the as-grown sample and for the sample diffused at 586°C for the 55.55h. Because the isotopes are only enriched into the high 90% range, they obtained SIMS data from some of the residual minor Ge isotopes. This redundancy in data is very useful in the deconvolution of the SIMS instrument

function and in improving the accuracy of the data. The obtained results by Fuchs et al. are in excellent agreement with previously published values.

Ga self-diffusion in GaAs [321] and GaP [322] was measured directly in isotopically controlled GaAs and GaP heterostructures. In the case of GaP, for the experiment, ^{71}GaP and ^{69}GaP epitaxial layers 200 nm thick were grown by solid source MBE at 700°C on undoped GaP substrates. The natural Ga isotope composition in the GaP substrates is 60.2% ^{69}Ga and 39.8% ^{71}Ga . The compositions in the isotopically controlled epilayers, on the other hand, were 99.6% ^{69}Ga (^{71}Ga) and 0.4% ^{71}Ga (^{69}Ga). In the SIMS measurement, the primary ion beam was formed with 5.5 keV Cs^+ ions. GaCs^+ molecules were detected as secondary species as the sputtering proceeded.

As before, assuming Fick's equations describe the self-diffusion process and the diffusion coefficient D is constant [316], the concentrations of the Ga isotopes can be expressed as

$$C(x) = \frac{C_1 + C_2}{2} - \frac{C_1 - C_2}{2} \text{erf}(x/R), \quad (140)$$

where $x = 0$ at the epitaxial interface, C_1 and C_2 are the initial Ga isotope concentrations at the left- and right-hand side of the interface, respectively, and $\text{erf}(y)$ is the error function. The characteristic diffusion length R was defined as

$$R = 2\sqrt{Dt}, \quad (141)$$

where D is the Ga self-diffusion coefficient and t is the annealing time.

The SIMS data can then be compared with calculated values of $C(x)$. Adjusting the diffusion length R , a fit of $C(x)$ to the SIMS profile can be made. Fig. 57 shows the SIMS profiles (solid lines) and the calculated $C(x)$ of ^{69}Ga (circles) and ^{71}Ga (continuous line) in a sample annealed at $T = 1111^\circ\text{C}$ for 3 h and 51 min. Excellent agreement was obtained between the measured and the calculated profiles over two and a half orders of magnitude in concentrations. From these results for GaP Wang et al. [322] obtained the values of the activation enthalpy H^{SD} and self-diffusion entropy S^{SD} equal to 4.5 eV and $4k_B$, respectively. For comparison, Wang et al. [322] obtained the activation enthalpy and entropy for GaAs are 4.24 eV and $7.5k_B$, respectively. The significant difference in values of S^{SD} , according Wang et al., indicates profound variations in the way that the mediating native defects are formed or migrate in GaP as compared to GaAs. The small value S^{SD} in GaP may be connected to the stronger Ga - P bond compared to the Ga - As bond (see, also [323]).

Bract et al. [324] studied (see, also Fig. 58) the Ga self-diffusion and Al - Ga interdiffusion with isotope heterostructures of AlGaAs/GaAs . Ga diffusion in $\text{Al}_x\text{Ga}_{1-x}\text{As}$ with $x = 0.41; 0.62; 0.68$ and 1.0 was found to decrease with increasing Al concentration. The intermixing observed at AlGaAs/GaAs interfaces was accurately described if a concentration-dependent interdiffusion coefficient was assumed. The higher Al diffusivity in GaAs as compared to Ga self-diffusion was attributed to the higher jump frequency of ^{27}Al as compared to ^{71}Ga caused by the difference in their masses. The lower Ga diffusivity in AlAs compared to GaAs was proposed to be due to lower thermal equilibrium concentrations of vacancies (C_v^{eq}) in AlAs as compared to GaAs. The different values C_v^{eq} in these materials were explained by the differences in the electronic properties between AlAs and GaAs. We should add here that the value of acti-

vation enthalpy Q of studied heterostructures lies in the range 3.6 ± 0.1 that is consistent with Wee et al. [325] results.

Very recently Bracht et al. [314] have reported the diffusion of boron, arsenic and phosphorus in silicon isotope multilayer structures at temperatures between 850°C and 1100°C . The diffusion of all dopants and self - atoms at a given temperature is modeled with the same setting of all native - point - defect - related parameters. As an example on the Fig. 58 the concentration profiles of ^{31}P along with the corresponding ^{30}Si profiles measured with SIMS after diffusion are shown. The diffusion of P in the isotope structure leads to an I (interstitial) supersaturation and V (vacancy) undersaturation and thereby suppresses the contribution of vacancies in P and Si diffusion compared to the diffusion of As. This increases the sensitivity of the P and Si profiles to negatively charged self - interstitials. The demand to describe the diffusion of all dopants and the corresponding Si profiles at a given temperature with the same energy levels of the native - point defects led to the conclusion that negatively charged vacancies rather than negatively charged self - interstitials dominate under n - type doping. Successful modeling of the simultaneous P and Si diffusion requires a contribution of a singly positively charged mobile P defects to P diffusion (for details see, also [313]).

5.1.1.2. Neutron transmutative doping of semiconductors.

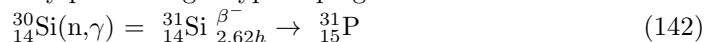
The main advantage of the neutron transmutative doping (NTD) method, as we know at present, is the precision doping which is connected with the linear dependence of concentration of doping impurities on the dose of neutron irradiation. Such dependence is numerous observed in the different experiments (see, e.g. [326 - 328]). As an example, in Fig. 60 there is shown the dependence of the concentrations doped phosphorus on the dose of irradiation the Si crystal in nuclear reactor. This dependence was measured with the help of Hall effect [329]. However, at the large dose of neutron irradiation there is observed the non - linear dependence. On Fig. 45 in Ref. 30 was shown the results of paper [330] where was observed the deviation from linear law at the large dose of neutron irradiation of the sample of ^{74}Ge which was annealed after irradiation at 460°C during different time. More amazing effect was observed at the second irradiation of the samples of ^{74}Ge previously strong doped with As by NTD method. Instead expectable increase of the concentration free charges (electrons) n there is observed the decrease n . This decrease was direct proportional to the neutron irradiation dose of ^{74}Ge crystals. Both effects are rather details analyzed in papers [327, 330]. The transmutation of the stable germanium isotopes via capture of thermal neutrons is well understood. Considering Ge and Si it should be note, that donors As and P will be created, following neutron capture and β - decay of isotopes of these semiconductor elements. The new elements are, of course, the prototypical donors. Neutron capture leads to NTD. Beside that, there are elements which have light isotopes which upon neutron capture transmute to a lower Z element either by electron capture or by positron decay. In

this case acceptors are created. A classical case is the transmutation of $^{70}_{32}\text{Ge}$ into $^{71}_{31}\text{Ga}$ (for details see [30]).

It is well-known that doping of silicon single crystals by incorporation of impurities from the melt during solidification in most cases leads to an inhomogeneous distribution of impurities in the solids [331 - 333]. This is due to the fact that nearly all impurities in silicon have thermal equilibrium distribution coefficients much less than unity and that the solidification or crystal growths at each position of the interface is characterized by a different state of thermal inequilibrium leading to distribution coefficients that in space and time continuously change and result in a nonuniform impurity distribution [334, 335]. In actual crystal production the nonuniformity is further enhanced by lack of control of exactly constant melt volume and feed of the doping impurity. The most widely used doping elements in silicon are boron and phosphorus. Boron has a distribution coefficient between 0.9 and 1 which makes a doping uniformity of $\pm 10\%$ easily obtainable (see, e.g. [333]). The thermal equilibrium distribution coefficient for phosphorus of approximately 0.3 leads in general to the above mentioned large doping variations both on a microscale (center to periphery) and on a macroscale (striations). No other n-type doping element has a larger distribution coefficient. Because fast diffusing p-type dopants (Ga, Al) are available, because electron mobility is greater than hole mobility, and because contact alloying technology is reasonable, n-type silicon is generally used for solid state power devices [334, 336]. With avalanche breakdown voltages being determined from areas with lower resistivities, use of a conventionally doped material results in hot-spot formation prior to breakdown and too high forward voltage drop leading to excessive heat dissipation because of a safe punch through design [331, 333, 337].

Phosphorus doping by means of NTD was suggested by Lark-Horovitz [338] and Tanenbaum and Mills [339] for homogeneity purposes and has been applied for high-power thyristor manufacturing in [331, 333, 336]. Hill et al. [336] were demonstrated how such a homogeneous phosphorus doping may result in a "theoretical design" possibility for high-power components (see also below).

The process used for fractional transmutation of silicon into phosphorus and thereby performing n-type doping



was first pointed out by Lark-Horovitz in 1951 [338]. Apart from special applications and research, the above process was, however, not utilized to any extent until the early seventies, at which time manufacturers of high-power thyristors and rectifiers for high-voltage direct current transmission lines, in particular, initiated usage of the transmutation doping process [340, 336, 341]. The reasons for not using the neutron doping method throughout the sixties may be found in the lack of a processing technology which could benefit from a more uniform doping, insufficient availability of high resistivity starting material, and the lack of nuclear reactors with irradiation capacities in excess of that needed for testing fuel and materials for nuclear power stations.

Let us, for the following discussion, assume that completely uniform neutron

doping may be accomplished. The homogeneity of the doped silicon is in this case determined by the background doping, i.e., the distribution of impurities in the starting material, where the net impurity concentration may be of either donor or acceptor type. Let us further, for simplicity, consider starting material of one conductivity type and assume complete n - type conduction after irradiation and annealing. With C_S being the net impurity concentration of the starting material and C_D the resulting donor concentration after irradiation we have, for both n - and p - type material,

$$C_D^{\max} - C_D^{\min} = C_S^{\max} - C_S^{\min}. \quad (143)$$

In such case we may define

1) the homogeneity factors for the starting material (α_S) and for the neutron doped material (α_D), respectively

$$\alpha_S = \frac{C_S^{\min}}{C_S^{\max}} \quad (144)$$

and

$$\alpha_D = \frac{C_D^{\min}}{C_D^{\max}} \quad (145) \text{ and}$$

2) the doping factor

$$f_D = \frac{C_D^{\max}}{C_S^{\max}}. \quad (146)$$

From this is easily derived

$$1 - \alpha_D = \frac{1 - \alpha_S}{f_D}. \quad (147).$$

Table 15 of Ref. 30 summarizes values of α_D as a function of α_S and f_D . It is seen that in order to obtain neutron-doped silicon with, for instance, a homogeneity factor greater than 0.9, it is necessary to use a doping factor of at least 7 when starting from "undoped" n-type material in which the homogeneity factor is typically not greater than 0.3 when taking the microcavitations (striations) into account. An examples of such neutron-doped silicon are shown in Figs. 61 and 62. It should be noted that in terms of resistivity, which is often used for impurity characterization, a doping factor f_D means use of starting material with minimum resistivity a factor f_D or $2.8f_D$ greater than the resistivity after neutron doping for n - and p-type starting material, respectively. The difference is due to the electron mobility being 2.8 times greater than the hole mobility. In conclusion of this section it should be generally noted that in order to make neutron-doped silicon with significantly more uniform resistivity than conventionally doped material, a doping factor $f_D = 5$ or more should be applied.

Following Janus and Malmros [340] let us consider further the theoretical case where a cylindrical silicon crystal is surrounded by a material with the same neutron absorption and scattering efficiency as the silicon itself (see Fig. 57 in Ref. [30]). Let us furthermore assume a thermal neutron flux gradient along an x axis perpendicular to the crystal axis with the neutrons coming from an external source. In this case the neutron flux will have the form

$$\Phi = \Phi_0 \cdot \exp\left(-\frac{x}{b}\right), \quad (148)$$

where b, the decay length, may be obtained from the formula

$$b = (3 \cdot \sigma_{Si} \cdot \sigma_{Si,t} \cdot C_{Si}^2)^{-0.5}. \quad (149)$$

$\sigma_{Si} = 0.16 \cdot 10^{-24} \text{ cm}^2$ is the mean of the absorption cross-sections for the 3 silicon isotopes, ^{28}Si , ^{29}Si and ^{30}Si weighted with their abundance. $\sigma_{Si,t} =$

$2.3 \cdot 10^{-24} \text{ cm}^2$ is the total cross-section (absorption + scattering) and $C_{\text{Si}} = 4.96 \cdot 10^{22} \text{ cm}^{-3}$ is the total number of silicon atoms in 1 cm^3 . Hence b may be calculated:

$$b_{\text{silicon}} = 19 \text{ cm.} \quad (150)$$

In order to improve the doping homogeneity in the cylindrical crystal this will be slowly rotated around its axis. The time average of this flux at the distance r from this axis is

$$\Phi = \frac{1}{\pi} \int_0^\pi \Phi_0 \exp\left[-\frac{r}{b} \cos t\right] dt = \Phi_0 \left[1 + \frac{1}{4} \left(\frac{r}{b}\right)^2 + \dots\right]. \quad (151)$$

The ratio between the neutron dose at the periphery and at the axis of the crystal cylinder will then be

$$\frac{\Phi(a)}{\Phi(0)} \simeq 1 + \frac{1}{4} \left(\frac{a}{b}\right)^2, \quad (152)$$

where a is the crystal radius (Fig. 57 in Ref. [30]).

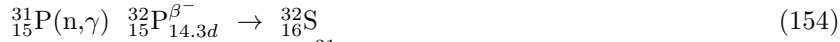
For intrinsic starting material the irradiation doped silicon will thus have a homogeneity factor of

$$\alpha_D \simeq 1 - \frac{1}{4} \left(\frac{a}{b}\right)^2 \simeq 0.956 \quad (153)$$

for an 80-mm-diameter crystal, i.e., the absorption limiting factor for the obtainable radial variations.

In the above analysis we have neglected the effects of fast neutron moderation in the silicon. By comparison, however, of irradiations performed in reactors with fast neutron fluxes from 10^{-4} to 1 times the thermal flux and with different flux gradients, the authors [340] have observed no influence on the resistivity homogeneity due to fast neutron moderation in the silicon.

In irradiated silicon crystals for semiconductor device applications only two isotopes ^{31}Si and ^{32}P are of importance in connection with radioactivity of neutron doped material. For thermal neutron doses less than $10^{19} \text{ neutron/cm}^2$, no other elements have been detected emitting radiation. Further more, ^{31}Si , having a half - life of 2.62 h, decays to an undetectable level in 3-5 days. For this reason, it will be discussed the radioactivity only of the ^{32}P isotope. Fig. 58 in Ref. [30] pictures the ^{32}P activity as a function of final resistivity for a variety of thermal neutron flux levels typical for the nuclear test reactors in use. As was shown in [340] absolute flux determination to 1% accuracy has proven obtainable for instance by means of calorimetric boron carbide monitors.



as a secondary one with ^{31}P concentration at each instant in time being dependent on the neutron dose received and the time allowed for the $^{31}_{14}\text{Si}_{2.62h}^{\beta^-} \rightarrow ^{32}_{15}\text{P}$ decay.

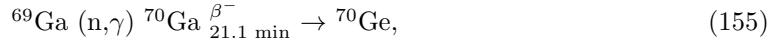
The use of NTD is of particular interest to thyristor manufacturers where n-type starting material is required for the basic p - n - p structure [342, 335]. Some advantages for high power device design and performance include:

- 1) more precise control of avalanche breakdown voltage,
- 2) more uniform avalanche breakdown, i.e., greater capacity to withstand overvoltages,
- 3) more uniform current flow in forward direction, i.e. greater surge current capacity, and

4) narrower neutral zone and therefore narrower base and lower forward voltage drop V_f .

The summary of some points concerning the preparation of NTD silicon for special applications on an R and D scale describe in papers [335, 336]. The production of large quantities of NTD silicon for power devices is described in [343]. More recently (see, e.g. [344]) the NTD technique has been also proposed for the effectual doping of P in a-Si:H films (see also [209]). The results of [344] are shown that NTD technique is an excellent method for doping of P in a-Si:H.

The NTD method have used with success in study of compound semiconductors: GaAs [345 - 348] and GaP [349, 350]. NTD of GaAs is based on the following thermal neutron capture nuclear reactions (see also [351]):



The relative abundances of the isotopes involved in the reactions and the cross-sections for these reactions are such that the ratio of Se and Ge concentrations produced is

$$N_{\text{Se}}/N_{\text{Ge}} = 1.46. \quad (158)$$

Selenium is a typically shallow substitutional donor in GaAs with an electronic energy level a few meV from the conduction bands edge [352]. Germanium in GaAs is an amphoteric impurity which acts as a shallow donor (also a few meV from the conduction band) is situated on a Ga site and as an acceptor level at $E_V + 0.04 \text{ eV}$ if situated on an As site [351]. Since, if electronically active, all of the Se atoms and some portion of the Ge atoms are expected to act as donors, NTD of GaAs is expected to dope GaAs more n-type. The addition of donors moves the Fermi level (E_F) away from the valence band (E_V) to the conduction band (E_C). If a sufficiently high concentration of donors is added, E_F will move to the upper half of the bandgap and the GaAs will be converted to n-type. Analysis of Hall effect data as a function of temperature provides a means of measuring the donor content in irradiated GaAs samples. Young et al were thus able to compare electrically active added donor content to the NTD-produced impurity concentrations determined from nuclear measurements. The Hall effect analysis also allows them to determine concentrations and energy levels (E) of impurities or defects in the p-type GaAs samples if the Fermi level in the material moves near E at some temperature over the range of measurements. This technique thus provides a means of identifying and measuring undercompensated acceptor content in the samples. The low temperature photoluminescence technique used in paper [351] measured donor-to-acceptor or conduction-band-acceptor luminescence. It provides an accurate determination of the position of acceptor electronic levels in the GaAs, permitting positive identification of impurities or defects with known luminescence lines. Identifications of lines due to specific impurities or defects can be made using luminescence techniques regardless of the position of the Fermi level in material. Little detailed information concerning an acceptor level can be obtained from Hall effect if that acceptor is overcompensated. However, the presence of specific acceptors can

be detected by luminescence techniques even in n-type samples. On other hand, luminescence data do not provide the quantitative information obtainable from Hall effect measurements.

Figures 63 and 64 show relative luminescence spectra for the four n-type samples respectively. The spectral positions indicated by arrows for carbon acceptor, the Ge acceptor, and 0.07 eV acceptor correspond to donor (or band) to acceptor luminescence lines. The most important conclusion to be drawn from a comparison of the spectra for the control and eight NTD samples is that Ge acceptors not present in the "starting material" control sample are introduced by the NTD process. The increase in intensity of the Ge acceptor line with increasing dose relative to both the carbon and 0.07 eV acceptor lines indicates that Ge acceptor content increases with increasing transmutation doping. Therefore, some of the Ge atoms produced by NTD in these samples are acting as acceptors rather than donors. Photoluminescence measurement studies of the control and eight annealed NTD samples at longer wavelengths indicate another new line present only in NTD samples at about 9450 Å. The intensity of this line increases with increasing NTD dose.

The characteristic lifetimes of radioactive isotopes can be used to label and identify defect levels in semiconductors which can be described in part 5.2.3.

5.1.1.3. Optical fiber.

The reflection and transmission of a plane wave, or ray, which is incident on a planar interface between two semi - infinite, uniform media is determined by Snell's laws (see, e.g. [353, 3]). In Fig. 65, the refractive indices of the medium of incidence and the second medium are n_{co} (core) and n_{cl} (cladding) $< n_{co}$, respectively, and the critical angle $\alpha_c = \sin^{-1}(n_{cl}/n_{co})$. Further we denote the angles of incidence, reflection and transmission, or refraction, relative to the normal QN (see Fig. 65) by α_i , α_r , and α_t , respectively. The incident, reflection and transmitted, or refracted, rays and the normal QN are coplanar. If $\alpha_i > \alpha_c$, the incident ray in Fig.65^a undergoes total internal reflection and $\alpha_r = \alpha_i$, but if $\alpha_i < \alpha_c$ there is partial transmission, or refraction, as shown in Fig. 65^b and the angles satisfy

$$\alpha_i = \alpha_r \quad (159) \text{ and}$$

$$n_{co}\sin\alpha_i = n_{cl}\sin\alpha_t. \quad (160)$$

Usually for the planar waveguides it is convenient to express these laws in terms of the complementary angles of incidence, reflection and transmission, i.e. $\theta_z = \pi/2 - \alpha_i = \pi/2 - \alpha_r$ and $\theta_t = \pi/2 - \alpha_t$ and the complementary critical angle $\theta_c = \pi/2 - \alpha_c$.

One of the possible major applications of isotopic engineering it will be considered isotopic fiber-optics and isotopic optoelectronics at large (see also [3, 354]). It is known that for typical solids the lattice constant variations of isotopically different samples are usually within the limits [3]

$$\frac{\Delta d}{d} \sim 10^{-3} \div 10^{-4}. \quad (161)$$

Let us define an isotopic fiber as a structure in which core and cladding have the same chemical content but different isotopic composition (see Fig. 66)

The boundary between different isotopic regions form an isotopic interface. The difference in the refractive index on both sides of the isotopic interface could lead to the possibility of total internal reflection of light and, consequently, could provide an alternative route to the confinement of light. For a quantitative estimate let us consider a boundary between SiO_2 (the main component of silica) where body sides are identical chemically and structurally but have a different isotopic content - e.g. $^{28}\text{Si}^{16}\text{O}_2$ and $^{30}\text{Si}^{18}\text{O}_2$ respectively (Fig. 66). In the first approximation the refractive index n is proportional to the number of light scatterers in the unit volume. From the Clausius-Mosotti relation (see, e.g. [355]) for the refractive index one can deduce the following proportion (at $\Delta n \ll n$)

$$\frac{\Delta n}{n} \simeq 3c \frac{\Delta d}{d}, \quad (162)$$

where c is a dimensionless adjustment factor of the order of unity. Substituting Eq. (161) to Eq. (162) we can obtain

$$\frac{\Delta n}{n} \sim 3 \cdot 10^{-3} \div 10^{-4}. \quad (163)$$

Using the Snell law of light refraction we obtain the following expression for the ray bending angle θ when the light travels through the refractive boundary (see, also Fig. 67)

$$\theta \simeq \alpha_0 - \arcsin \left(\frac{n_1}{n_2} \sin \alpha_0 \right), \quad (164)$$

where α_0 is the angle between the falling ray and the direction normal to the interface. For a sliding ray ($\alpha_0 \simeq 90^\circ$), which is the control case for light confinement in fibers, the combining of Eqs (163) and (164) leads to an estimate $\theta \sim 1.5 \div 4.5^\circ$. (165)

Thus, the isotopic fibers in which core and cladding are made of different isotopes the half-angle of the acceptance-cone could be up to several degrees [356]. The resulting lattice mismatch and strains at the isotopic boundaries are correspondingly one part per few thousand [3] and, therefore, could be tolerated. Further advancement of this "isotopic option" could open the way for an essentially monolithic optical chip with built-in isotopic channels inside the fully integrated and chemically uniform structure.

Besides that we should pay attention to the fact that composition (different isotopes) fluctuation are subject to the restoring force of the total free energy of the glass system which will also seek to minimize itself. Using isotope pure materials for core and cladding we should receive significant less Rayleigh scattering (see e.g. [3]).

5.1.1.4. Laser materials.

General considerations. As is well-known, the word laser is an acronym for "light amplification by the stimulated emission of radiation", a phrase which covers most, though not all, of the key physical processes inside a laser. Unfortunately, that concise definition may not be very enlightening to the nonspecialist who wants to use a laser but has less concern about the internal physics than the external characteristics. A general knowledge of laser physics is as helpful to the laser user as a general understanding of semiconductor physics is to the

circuit designer. From a practical standpoint, a laser can be considered as a source of a narrow beam of monochromatic, coherent light in the visible, infrared or UV parts of spectrum. The power in a continuous beam can range from a fraction of a milliwatt to around 20 kilowatts (kW) in commercial lasers, and up to more than a megawatt in special military lasers. Pulsed lasers can deliver much higher peak powers during a pulse, although the average power levels (including intervals while the laser is off and on) are comparable to those of continuous lasers

The range of laser devices is broad. The laser medium, or material emitting the laser beam, can be a gas, liquid, crystalline solid, or semiconductor crystal and can range in size from a grain of salt to filling the inside of a moderate-sized building. Not every laser produces a narrow beam of monochromatic, coherent light. A typical laser beam has a divergence angle of around a milliradian, meaning that it will spread to one meter in diameter after traveling a kilometer. This figure can vary widely depending on the type of laser and the optics used with it, but in any case it serves to concentrate the output power onto a small area. Semiconductor diode lasers, for example, produce beams that spread out over an angle of 20 to 40° hardly a pencil-thin beam. Liquid dye lasers emit at a range of wavelengths broad or narrow depending on the optics used with them. Other types emit at a number of spectral lines, producing light is neither truly monochromatic nor coherent. Practically speaking, lasers contain three key elements. One is the laser medium itself, which generates the laser light. A second is the power supply, which delivers energy to the laser medium in the form needed to excite it to emit light. The third is the optical cavity or resonator, which concentrates the light to stimulate the emission of laser radiation. All three elements can take various forms, and although they are not always immediately evident in all types of lasers, their functions are essential. Like most other light sources, lasers are inefficient in converting input energy into light; efficiencies can range from under 0.01 to around 20% [357].

In order to observe high excitation semiconductors (insulators) (HES) effects, it is necessary that the electronic excitations interact with each other at a sufficiently high rate. The short lifetime and diffusion path in direct gap materials necessitate a rather high density n of bound (excitons) or unbound electronic excitations. A value of $n = 10^{17} \text{ cm}^{-3}$ is a reasonable average [357], though the onset of HES effects depends strongly on the compounds under investigation, on the quality of the individual sample and on the special conditions of the experiment (see, e.g. [358]). The lifetime of excitons τ in direct gap materials is about 1 ns at low densities. It is reduced at high densities by quadratic recombination processes and stimulated emission to values around 0.1 ns (see [358, 359] and references therein).

The generation rate G , which is needed to obtain a stationary concentration of $n = 10^{17} \text{ cm}^{-3}$ e-h pairs with a lifetime of 10^{-10} s is at least $G \simeq 10^{27} \text{ cm}^{-3} \text{ s}^{-1}$. G has now to be connected with the excitation intensity I_{exc} , where I_{exc} is the energy per units of area and time impinging on the sample. Some authors prefer to give the photon flux density I_{ph} instead of I_{exc} in the case of optical excitation. They are connected by $I_{exc} = I_{ph} \cdot \hbar\omega$. Thus, $I_{exc} \simeq 10^6$

Wcm^{-2} with N_2 laser ($\hbar\omega_{exc} = 3.78 \text{ eV}$) corresponds to $I_{Ph} = 1.7 \cdot 10^{24} \text{ cm}^{-2} \text{ s}^{-1}$.

In the case of nonresonant two-photon band-to-band excitation of semiconductors for which the absorption edge $\hbar\omega_{ed}$ fulfills the inequality $2\hbar\omega_{exc} > \hbar\omega_{ed} > \hbar\omega_{exc}$, the relation between G and I_{exc} reads

$$I_{exc} = \left(\frac{G2\hbar\omega_{exc}}{K_2} \right)^{1/2}, \quad (166)$$

where K_2 is the two-photon absorption coefficient. Since K_2 is of the order of $10^{-7} \text{ W}^{-1} \text{ cm}$ for many direct materials (see, e.g. [360]) I_{exc} has to be about $2 \cdot 10^7 \text{ Wcm}^{-2}$ in order to observe HES effects. In real experiments on semiconductors I_{exc} is varied from 10^5 Wcm^{-2} to 10^8 Wcm^{-2} , where the upper limit is given by the threshold for destroying the sample surface. The excitation by two-photon absorption is especially useful if a homogeneous bulk excitation of rather thick samples is desired. With a standard Q - switched ruby laser volumes of several mm^3 can be pumped.

In the case of one-photon excitation in the exciton or band-to-band region, an equation like

$$I_{exc} = G\hbar\omega_{exc}/K_1 \quad (167)$$

does not hold. The values of the one-photon absorption coefficient K_1 are of the order of 10^5 cm^{-1} or even higher. However, the created e-h pairs do not remain confined in a surface layer of a thickness of $K_1^{-1} \leq 0.1 \text{ } \mu\text{m}$ but rapidly spread out into the volume of the crystal, driven by the gradient of the chemical potential. The effective penetration depth d_{eff} is generally assumed to be one or a few micrometers [358]. A value of this order of magnitude has been found in CdS, where a thin platelet (above $4 \text{ } \mu\text{m}$ thick) was excited by a N_2 - laser from one side and the change of the excitonic reflection spectra with I_{exc} was investigated on both sides of the sample [361]. Therefore, equation (167) should rather be replaced by

$$I_{exc} = G \cdot \hbar\omega_{exc} \cdot d_{eff}. \quad (168)$$

In the experiments I_{exc} is typically varied from 10^3 Wcm^{-2} up to $5 \cdot 10^6 \text{ Wcm}^{-2}$, the upper limit is again given by the damage threshold of the sample surface. With one-photon excitation it is generally possible to reach higher G values. Because of the high diffraction losses of the thin excited layers [362], it is partly possible to suppress the optical stimulation of recombination processes, especially if small diameters D of the excitation spot are used ($D < 100 \text{ } \mu\text{m}$).

It should be pointed out, that the excitation conditions for indirect gap semiconductors are quite different from those described above. In these materials the lifetime is several orders of magnitude larger than in direct gap materials. Therefore, excitation sources with much lower values of I_{exc} and even conventional incandescent lamps may be used, either pulsed or in a continuously working mode.

Diamond. Diamond has an indirect band structure similar to silicon [363], with six equivalent conduction band minima located on the $\langle 100 \rangle$ axes at $0.76k_{\text{max}}$. Quantitatively, however, diamond is different from all standard cubic semiconductors [203] including silicon in that the valence band spin-orbit interaction Δ_0 at $k = 0$ is very much smaller than the excitonic interactions important in optical experiments. The latter are the exciton binding energy E_B

= 80 meV and the localization energy $E_{loc} = 51$ meV of excitons to the acceptor in p-type semiconducting diamonds [364]. Substitutional boron is the only shallow impurity in diamond with an ionization energy $E_i = 370$ meV [28]. The spin-orbit splitting between the fourfold degenerate Γ_8^+ band and the twofold Γ_7^+ band amounts to $\Delta_0 = 6$ meV experimentally or to $\Delta_0 = 13$ meV theoretically in linear muffin-tin orbital and $k \cdot p$ calculations [27]. In all other standard cubic semiconductors this ordering of the interaction energies is inverse, yielding $\Delta_0 \gg E_B$ and E_{loc} . In silicon, e.g. $\Delta_0 = 44$ meV, $E_B = 14.7$ meV and $E_{loc} \approx 0.1 E_i$ according to Haynes' rule [365], with E_i ranging from ≈ 45 meV for the shallow donor phosphorus and the shallow acceptor boron up to ≈ 155 meV for the relatively deep acceptor indium [365] (for details see [28]).

The diamond having a wide band gap can emit the intense ultraviolet (uv) radiation due to recombination of the indirect free exciton [366]. Additionally, since the exciton has an extremely large binding energy ($E_B = 80$ meV) [367], diamond is one of the most promising candidates to realize opto-electronics devices, such as uv laser diode, available at a higher temperature. Nevertheless, only a little work has been done on the intrinsic recombination luminescence of indirect free excitons created only by d.c. - operated electron beams with much higher energy relative to the indirect band gap energy. Figure 68 shows typical photo-excited intrinsic edge emission spectra high-pressure synthetic (HPS) type-IIa diamond at temperatures of (a) 85K, (b) 125K and (c) 300K, which are almost the same as cathodoluminescence spectra in natural type IIa [367, 368] and the chemical vapor deposition (CVD) [369] (see, also Fig. 15 in Ref. [28]). Takiyama et al. [366] have been established that B_1 band consists of two Maxwell - Boltzman components labeled B'_1 and B_1 with the energy splitting (~ 7 meV) due to the spin-orbit interaction of the hole state (see, also [367]). The obtained in paper [366] intensity ratio of B'_1 to B_1 shows that thermalization occurred between the components in the free exciton state at each temperature (thermal equilibrium). Luminescence intensities of all these bands increase with increasing temperature and reach a maximum causes the remarkable reduction of the intensity. The intensities at 125K and 300K are approximately twice and 1/10 of that at 85K, respectively. No extrinsic emission due to bound excitons was found in the indirect edge region (5.5 - 4.8 eV).

In Ref. [366] decays of B_1 emission in the HPS type-IIa diamond were measured at the temperature of 75 - 300K and were found to be exponential over more than one order of magnitude, as typically illustrated in Fig. 69. The lifetime of free excitons at 85K is estimated to be 40 ns from the slope of curve (a). With increasing temperature (125K), the lifetime (70 ns) increases as well as the intensity. Both the lifetime and the intensity reach a maximum at ~ 150 K. At higher temperature (300K - curve c), they become shorter (20 ns) and much weaker than those at 125K. These decrements are due to the thermally-activated exciton ionization. The measured free exciton lifetime in the temperature range 75 - 300K are shown in Fig. 69. As it can see from Fig. 70, authors [366] successfully reproduced the temperature dependence of the lifetime of the exciton, where the best fit values obtained assuming $E_B = 80$ meV.

As is well-known natural diamond is 98.9% ^{12}C and 1.1% ^{13}C ; synthetic diamonds, however, may be grown with ^{13}C concentrations in the range $<0.1\%$ to 99% . The change of the indirect gap of diamond between pure ^{12}C and ^{13}C has been determined by Collins et al. [367], using for this purpose the luminescence spectra of diamond. The luminescence spectra of the natural (^{12}C) and synthetic (^{13}C) diamond were investigated by Collins et al. [367], Ruf et al. [370]. Fig. 15 in Ref. 28 compares the edge luminescence for a natural diamond with that for a synthetic diamond. The peaks labelled A, B and C are due, respectively, to the recombination of a free exciton with the emission of transvers - acoustic, transverse-optic and longitudinal-optic phonons having wavevector $\pm k_{\min}$ and quanta (in ^{12}C diamond) [371].

$$\hbar\omega_{TA} = 87 \pm 2, \hbar\omega_{TO} = 141 \pm 2, \hbar\omega_{LO} = 163 \pm 1 \text{ meV}. \quad (169)$$

Features B_2 and B_3 are further free-exciton processes involving the above TO phonon with one and two zone-centre optic phonons, respectively.

Boron forms an effective-mass-like acceptor in diamond, and both specimens used in Fig. 15 are slightly semiconducting with uncompensated boron concentrations around $5 \cdot 10^{16} \text{ cm}^{-3}$ in the natural diamond and $3 \cdot 10^{16} \text{ cm}^{-3}$ in the synthetic diamond. Peaks labelled D are associated with the decay of excitons bound to the boron acceptors (for details see Collins et al. [367]). Comparison of the data from the two diamonds shows that the zero-phonon lines D_0 and D_0^i are $14 \pm 0.7 \text{ meV}$ higher for ^{13}C than for ^{12}C diamond, and that the LO and TO phonon energies are lower by a factor of 0.96, equal within experimental error to the factor $(12/13)^{1/2}$ expected to first order when the lattice is changed from ^{12}C to ^{13}C . The low-energy thresholds of the free-exciton peaks A, B and C are given by [367]

$$E_{th}(A) = E_{gx} - \hbar\omega_{TA}; E_{th}(B) = E_{gx} - \hbar\omega_{TO} \text{ and } E_{th}(C) = E_{gx} - \hbar\omega_{LO}. \quad (170)$$

As was shown by Collins et al. the predicted threshold are entirely consistent with the experimental data. From the results of Collins et al. it was concluded that the dominant contribution arises from electron-phonon coupling, and that there is a smaller contribution due to a change in volume of the unit cell produced by changing the isotope. These two terms were calculated as 13.5 ± 2.0 and $3.0 \pm 1.3 \text{ meV}$ respectively. The more detailed and quantitative investigations of $E_g \sim f(x)$, where x is the isotope concentration, were done by Ruf et al. [370], where was studied five samples of diamond with different concentrations x (see Fig. 16 in Ref. [28]). From these data Ruf et al. [370] determined the linear variation of $E_g \sim f(x)$ for diamond. Linear fits the experimental data of Ruf et al., (solid line in Fig. 17 in Ref. 28) yield a slope of $14.6 \pm 0.5 \text{ meV/amu}$, close to the theoretical predictions. To concluding this part we should note that Okushi et al. [370^a] systematic studied of cathodoluminescence spectra of free exciton emission from diamond under high excitation conditions.

LiH. The possibility of using indirect transitions for obtaining light generation in semiconductors was probably to Basov et al. [372]. The stimulating emission on the LO replicas (see, Fig. 71) of a zero - phonon line free - exciton emission in CdS under two - photon excitation was first obtained by Kulevsky and Prokhorov [374] (see also [360, 375, 376]). As was shown by Liu and Liboff

[377] taking into account the mixed crystals lattice potential relief it could not be excluded absolutely the possibility on the zero - phonon line emission (see, also below).

The detection of LO phonon replicas of free - exciton luminescence in wide - gap insulators attracted (see Fig. 72) considerable attention to these crystals (see e.g. [378]). At the same time it is allowed one to pose a question about the possibility of obtaining stimulated emission in UV (VUV) region (4 - 6 eV) of the spectrum, where no solid state sources for coherent radiation exist yet. In the first place this related to the emitters working on the transitions of the intrinsic electronic excitation. The last one provides the high energetical yield of the coherent emission per unit volume of the substance. The results obtained on solidified xenon [372] and argon [379] under electron beam excitation with following excimer molecules emission form an exception.

In this part we will discuss the investigation results of the influence of the excitation light density on the free excitons emission spectra in the wide - gap insulator LiH (LiH - LiF) crystals. As was shown above the cubic LiH crystals are typical wide - gap ionic insulator with relatively weak exciton - phonon interaction however: $E_B/\hbar\omega_{LO} = 0.29$ where E_B and $\hbar\omega_{LO}$ are exciton binding energy and longitudinal optical phonon's energy, respectively. Besides it might be pointed out that the analogous relation for CdS, diamond and NaI is 0.73; 0.45 and 12.7, respectively (see e.g. [221] and references therein).

The reflectance spectra of the investigated crystals with clean surface (cleaved in LHeT) had a distinctly expressed excitonic structure (see also chapter 3 of book [29]). However, despite of the identical structure of all free - excitons luminescence spectra (Fig. 72), it is necessary to note a rather big variation of the luminescence intensity of the crystals from the different batches observed in the experiment. Therefore the crystals possessing the maximum value of the free exciton luminescence quantum yield were chosen for measurements of the density effects.

As it was shown early that the exciton luminescence is observed in LiH crystals Fig. 72 excited by the energy photons from the depth of the fundamental absorption. As an example, the 1LO and 2LO assisted luminescence lines at the low excitation density are shown in Fig. 64 (curve 1) in Ref. 28. With the increase of the excitation density an additional emission appears on the long-wavelength side of both lines (curve 2, Fig. 64 in Ref. 28) These results show that the increase of the excitation density the luminescence intensity of this new feature rises more quickly in the vicinity of the 1LO replicas than in the vicinity of the 2LO replicas. This is common regularity. At the same time it is necessary to note that for obtaining of the spectrum demonstrated in Fig. 64 (curve 2) in Ref. 28 the excitation light intensity was varied from three to twenty times depending on the crystal origin (see also [372, 378]).

In more detail and with better resolution was investigated the influence of the excitation light intensity on the shape and line intensity of 2LO replicas [380]. The maximum sensitivity of the experimental equipment at the maximum spectral resolution in these experiments was achieved by the sharp focusing not only excitation but also the registrated channel. Results presented in Fig. 73

witness that with the growth of the excitation light intensity a little narrowing can be observed at the beginning which is followed by an ignition of the luminescence intensity on the longwavelength side of 2LO replicas line, as it is repeatedly observed for other ionic semiconducting compounds (in details see, also [360]). Simultaneously with this the appearance of a characteristic probably mode structure (see curves 2 and 3, Fig. 73) is observed the width of which is determined by power surpassing the threshold. The divergence angle of the generation emission is simply connected with it and for different semiconductors lies in the interval $2 \div 25^\circ$ (see, e. g. [360]).

As is known at moderate excitations levels a linear dependence of luminescence intensity on the excitation density is observed (see, e.g. [381]). Such dependence is also observed in LiH crystals and at more substantial excitation light intensities (see Fig. 66, curve 1 in Ref. 28). Such linear coupling is usually considered to be unequivocal and testifying about exciton formation only as a results of an indirect light absorption process ([382]). At the same time the measurements of the respective dependence on the long - wavelength side of 2LO replica line (see Fig 66, curve 2 in Ref. 28) shown that the coupling between the luminescence and excitation intensities is not only linear but, in fact, of a threshold character as in case of other crystals (see, also [360, 383]).

5.1.2. New applications - quantum information.

The current rapid progress in the technology of high-density optical storage makes the mere announcing of any other thinkable alternatives a rather unthankful task. An obvious query "who needs it and what for?" has, nevertheless, served very little purpose in the past and should not be used to veto the discussion of non-orthodox technological possibilities. One such possibility, namely the technology of isotopic information storage (IIS) is discussed in this paragraph.

Isotopic information storage may consist in assigning the information 'zero' or 'one' to mono-isotopic microislands (or even to a single atoms) within a bulk crystalline (or thin film) structure. This technique could lead to a very high density of ROM-type (read-only memory or permanent storage) information storage, probably up to 10^{20} bits per cm^3 . The details are discussed in papers [384, 261, 191, 28]: here it notes only that the use of tri-isotopic systems (e.g. ^{28}Si ; ^{29}Si ; ^{30}Si) rather than di-isotopic (e.g. ^{12}C ; ^{13}C) could naturally lead to direct three dimensional color imaging without the need for complicated redigitizing (it is known that any visible color can be simulated by a properly weighted combination of three prime colors, but not of two).

Indeed, let us assume that the characteristic size of one information-bearing isotopic unit (several atoms) is 100 \AA . Then 1 cm^3 of crystalline structure, e.g. diamond, is able to store roughly $(10^8)^3/100^3 = 10^{18}$ bits of information [384,28]. This capacity greatly exceeds that need to store the information content of all literature ever published ($\cong 10^{17}$ bits), including all newspapers.

The main potential advantage of isotope-mixed crystals lies in the fact that the information is incorporated in the chemically homogeneous matrix. There

are no chemically different impurities (like in optical storage with color centres) or grain boundaries between islands of different magnetization (like in common magnetic storage). The information in isotope-mixed crystals exists as a part of the regular crystals lattice. Therefore, the stored information in isotope-mixed crystals is protected by the rigidity of the crystal itself. There are no "weak points" in the structure (impurities, domain wells, lattice strain etc.) which can lead to the information loss due to bond strains, enhanced diffusion, remagnetization, etc. Differences in the bond lengths between different isotopes (e.g. ^{28}Si - ^{29}Si or ^{29}Si - ^{30}Si ; H - D and so on) are due to the anharmonicity of zero-point vibrations (see, e.g. [26, 151]). This is not enough for the development of any noticeable lattice strains although these differences are sufficiently large to be distinguishably detected in IIS - reading) (for details see [191]).

The development of efficient quantum algorithms for classically hard problems has generated interest in the construction of a quantum computer. A quantum computer uses superpositions of all possible input states. By exploiting this quantum parallelism, certain algorithms allow one to factorize [396] large integers with astounding speed, and rapidly search through large databases, and efficiently simulate quantum systems [398]. In the nearer term such devices could facilitate secure communication and distributed computing. In any physical system, bit errors will occur during the computation. In quantum computing this is particularly catastrophic, because the errors cause decoherence [399] and can destroy the delicate superposition that needs to be preserved throughout the computation. With the discovery of quantum error correction [400] and fault-tolerant computing, in which these errors are continuously corrected without destroying the quantum information, the construction of a real computer has become a distinct possibility (see, also [401]). The task that lie ahead to create an actual quantum computer are formidable: Preskill [402] has estimated that a quantum computer operating on 10^6 qubits with a 10^{-6} probability of error in each operation would exceed the capabilities of contemporary conventional computers on the prime factorization problem. To make use of error-correcting codes, logical operations and measurement must be able to proceed in parallel on qubits throughout the computer. Several systems have been recently been proposed to obtain a physical implementation of a quantum computer (for detail see, e.g. [28, 191] and references therein).

As was shown for the first time by Schrödinger [385] fundamental properties of quantum systems, which might be include to information processes are:

1. Superposition: a quantum computer can exist in an arbitrary complex linear combination of classical Boolean states, which evolve in parallel according to a unitary transformation [386].
2. Interference: parallel computation paths in the superposition, like paths of a particle through an interferometer, can reinforce or cancel one another, depending on their relative phase [387].
3. Entanglement: some definite states of complete quantum system do not correspond to definite states of its parts (see, also [388]).
4. Nonlocality and uncertainty: an unknown quantum state cannot be accurately copied (cloned) nor can it be observed without being disturbed [389,

390].

These four elements are very important in quantum mechanics, and as we'll see below in information processing. All (classical) information can be reduced to elementary units, what we call bits. Each bit is a yes or a no, which we may represent it as the number 0 or the number 1. Quantum computation and quantum information are built upon analogous concept, the quantum bit [391], or qubit for short. It is a two-dimensional quantum system (for example, a spin 1/2, a photon polarization, an atomic system two relevant states, etc.) with Hilbert space. In mathematical terms, the state of quantum state (which is usually denoted by $|\Psi\rangle$ [385]) is a vector in an abstract Hilbert space of possible states for the system. The space for a single qubit is spanned by a basis consisting of the two possible classical states, denoted, as above, by $|0\rangle$ and $|1\rangle$. This mean that any state of qubit can be decomposed into the superposition

$$|\Psi\rangle = \alpha|0\rangle + \beta|1\rangle \quad (171)$$

with suitable choices of the complex coefficients a and b . The value of a qubit in state $|\Psi\rangle$ is uncertain; if we measure such a qubit, we cannot be sure in advance what result we will get. Quantum mechanics just gives the probabilities, from the overlaps between $|\Psi\rangle$ and the possible outcomes, rules due originally by Max Born (see, e.g. [392]). Thus the probability of getting 0 is $|\langle 0|\Psi\rangle|^2 = |\alpha|^2$ and that for 1 is $|\langle 1|\Psi\rangle|^2 = |\beta|^2$. Quantum states are therefore normalized; $\langle\Psi|\Psi\rangle = (b^*a^*) \cdot \begin{pmatrix} b \\ a \end{pmatrix} = 1$ (where $|\Psi\rangle$ is

represented by the vector $\begin{pmatrix} b \\ a \end{pmatrix}$) and the probabilities sum to unity. Quantum mechanics also tells us that (assuming the system is not absorbed or totally destroyed by the action of measurement) the qubit state of Eq. (171) suffers a projection to $|0\rangle$ ($|1\rangle$) when we get the result 0(1). Because $|\alpha|^2 + |\beta|^2 = 1$ we may rewrite Eq. (171) as (see, e.g. [393])

$$|\Psi\rangle = \cos\theta|0\rangle + e^{i\varphi}\sin\theta|1\rangle \quad (172)$$

where θ, φ are real numbers. Thus we can apparently encode an arbitrary large amount of classical information into the state of just one qubit (by coding the information into the sequence of digits of θ and φ). However in contrast to classical physics, quantum measurement theory places severe limitations on the amount of information we can obtain about the identity of a given quantum state by performing any conceivable measurement on it. Thus most of the quantum information is "inaccessible" but it is still useful - for example it is necessary in its totality to correctly predict any future evolution of the state and to carry out the process of quantum computation (see, e.g. [395]).

The numbers θ and φ define a point on the unit three - dimensional sphere, as shown in Fig. 74. This sphere is often called the Bloch (Poincare) sphere [394]; it provides a useful means of visualizing the state of a single qubit. A classical bit can only sit at the north or the south pole, whereas a qubit is allowed to reside at any point on the surface of the sphere [28].

Recently Kane [403] proposed a very interesting and elegant design for a

spin resonance transistor (SRT). He proposed to use the nuclear spins of ^{31}P dopant atoms, embedded in a silicon host, as the qubits. At low temperatures ($T < 0.1\text{mK}$) the dopant atoms do not ionize, and the donor electron remains bound to the ^{31}P nucleus. The control over the qubits is established by placing a gate-electrode, the so-called A-gate (see Fig. 75), over each qubit. By biasing the A-gate, one control the overlap of the bound electron with the nucleus and thus the hyperfine interaction between nuclear spin and electron spin, which allows two nuclear spins to interact by electron spin-exchange, which provides the required controlled qubit-qubit interaction (Fig. 76). The rate of loss of phase coherence between qubits in a quantum system is typically characterized by the dephasing time T_2 . At sufficiently low ^{31}P concentrations at temperature $T = 1.5\text{K}$, the electron-spin relaxation time is thousands of seconds and the ^{31}P nuclear spin relaxation time exceeds 10 hours. It is likely that at millikelvin temperatures the phonon limited ^{31}P relaxation time is of the order of 10^{18} [404], making this system ideal for quantum computation. In the work done by Kane et al. [405] a method for probing the spin quantum numbers of a two-electron system using a single-electron transistor is presented. In spite of significant technological difficulties for the realization of Kane's ingenious idea, e.g. it requires phosphorus atoms ordered as a regular array with spacing of 20 nm as well as a gate spacing of 10 nm, his model has triggered an enormous interest in semiconductor realizations of the nuclear spin quantum computers. We should add, that very perspective system of $\text{GaAs}/\text{Al}_{1-x}\text{Ga}_x\text{As}$ has a huge number of active nuclear spin ($\sim 10^4$), this reason does not permit this system used in quantum computation. Vrijen et al. [406] suggest using the full power of modern electronic band structure engineering and epitaxial growth techniques, to introduce a new, more practical, field effect SRT transistor design that might lend itself to a near term demonstration of qubits on a silicon-germanium heterostructures (for details see [407, 191]).

The last idea was developed by Shlimak et al. [408, 409]. The first step consists of the growth of isotopically engineered Si and Si - Ge epitaxial layers with lateral modulation of nuclear spin isotope content in the layer. The simplest case is a sequence of stripes of the spinless isotope (for example, ^{28}Si) and nonzero spin isotope (^{29}Si or natural Si, which contains 4.7% of ^{29}Si , or a controlled mixture of them). The following method, based on molecular - beam - epitaxy (MBE) growth on vicinal planes, can be suggested for preparation of such a striped layer. Usually, the substrate surface of Si cut at a small angle θ to some crystallographic direction consists of atomic size steps [410], followed by a relatively long plateau (see Fig. 77^a). The typical size of the steps a is of order 0.1 - 0.5 nm (depending on the crystallographic orientation), which gives the following value for the length of plateau: $d = a/\theta = 100 - 500 \text{ nm}$ for $\theta = 10^{-3}$. The atoms deposited on the hot substrate are mobile and move toward steps in the corner where more dangling bonds are utilized (see Fig. 77^b and Fig. 77^c). As a result, during the process of deposition and formation of a new layers, the steps move from left to right continuously. For a given deposition of one monolayer, i.e. to cover the entire plateau. If one isotope is deposited during the rest of this time τ (Fig. 77^b), followed by the other isotope being deposition

during the rest of this time interval $(t - \tau)$, then a periodical striped layer will be obtained with a controlled ratio of the strip widths: $\ell/(d - \ell) = \tau/(t - \tau)$, Fig 77^c. Taking into account that the typical growth rates in MBE reach values of about 0.5 \AA s^{-1} [411], the time t will permit the proposed procedure. The required number of monolayers with some amount of isotope ^{29}Si is determined by the minimal number of nuclear spins in a quantum dot which can be detected electronically. According [408] the next step of fabricating a nanosize structure on top of this layer. For this purpose, the scanning probe microscopy (SPM) technique is usually used, which can go lower than the limits obtainable by conventional methods, such as photon - and electron - beam lithography [412, 413]. In the case for fabrication of a nuclear - spin qubit device on top of an isotopically engineered Si layer, the authors [408] suggest using the atomic - force - microscopy - (AFM) - assisted local oxidation technique, which consists of the following steps. During the nanostructure patterning, the silicon surface will be firstly H passivated by treatment in buffered HF acid, which strips the native oxide and terminates the surface bonds with a hydride layer. This passivating hydride layer is robust and protects the surface for days from oxidation. Under suitable bias between conducting the AFM tip and the surface, the high electric field oxidizes the Si surface in the immediate vicinity of the tip. Feature down to 10 nm were obtained with this technique [408]. The more details of describing technology presents in Fig. 78.

Authors [409] believe that the proposed source - drain (SD) channel can also be used for the read - out operation, i.e. for the detection of a single nuclear spin state. The direct control of a nuclear spin state via nuclear magnetic resonance (NMR) measurements is a difficult problem. In Ref 414, coherent control of the local nuclear spin was demonstrated, base on pulsed NMR in a quantum Hall device. In Ref. 415, a self - contained semiconductor device is described that can nuclear spins in a nano - scale region. Measurements of the electron spin state are much easier taking into account the possibility of a spin - to - charge conversion for electrons. In accordance with the Kane model [403], the state of the nuclear spin ^{31}P is mediated by the spin of donor electron via the hyperfine interaction. Therefore the task is to determine the spin orientation of the corresponding donor electron. The suggested method [406] is based on the fact that at low temperatures, a donor atom can capture the second electron with small ionization energy, about 1 meV, which results in the appearance of negatively charged donor (D^- - center [371]). However, this process is possible only when the spin orientation of the second electron is opposite to that of the first electron. The appearance of the charged donor in the vicinity of the narrow SD channel will affect the current [416, 417] and can therefore be detected. As a result, one can determine the spin orientation of two neighboring donor electrons if one applies a potential difference between the corresponding A - gates which will cause the electron to jump from one donor to another. If we choose the spin orientation of the given donor as a reference, one can determine the spin state of the neighboring qubits on the right and left sides.

Following [409] we consider further a new mechanism of entanglement for distant qubits and discuss, first the principles of two - qubit operation. It has

been shown [418] that two - bit gates applied to a pair of electron or nuclear spins are universal for the verification of all principles of quantum computation.

Because direct overlap of wavefunctions for electrons localized on P donors is negligible for distant pairs, authors [409] proposed another principle of coupling based on the placement of qubits at fixed positions in a quasi - one - dimensional Si nanowire and using the indirect interaction of ^{31}P nuclear spins with spins of electrons localized in the nanowire which they called hereafter a "1D electrons". This interaction depends on the amplitude of the wavefunction of the "1D electrons" estimated at the position of the given donor nucleus $\Psi_n(\mathbf{r}_i)$ and can be controlled by the change in the number of "1D electrons" N in the wire. At $N = 0$, the interqubit coupling is totally suppressed, each ^{31}P nuclear spin interacts only with its own donor electron. Very recently it was shown [409^a], that the optical detection of the nuclear spin state, and selective pumping and ionization of donors in specific electronic and nuclear spin states, suggests a number of new possibilities which could be useful for the realization of silicon - based quantum computers.

5.2. Radioactive isotopes.

Radioactive isotopes (RI) are radioactive atoms of common elements like carbon, cobalt, or sodium etc. Usually RI are located in atomic "ash" that is left behind after uranium atoms are split in a "nuclear pile". Some RI are produced from exposure of common elements to powerful radiation inside a nuclear reactor during fission. Fission occurs when an atom's nucleus splits into two or more smaller nuclei, producing a large amount of energy. RI release radiation in the form of alpha, beta and gamma rays. The strength of the radiation is relative to the rate where radioactive material decays. Because of this, different radioisotopes can be used for different purposes, depending on their strength.

Some radioactive elements, such as radium - 224, radium - 226, radon 222, polonium - 210, tritium (^3H), carbon - 14, etc. are found in nature, but most radioactive materials are produced commercially in nuclear reactors or cyclotrons (see, e.g. [8,9, 13]) - also called particle accelerators. With nuclear reactors and cyclotrons, it is possible to make useful amounts of radioactive material safely and at low cost. Usually only one type of radionuclide can be produced at a time in a cyclotron, while a reactor can produce many different radionuclides simultaneously. As for unstable isotopes, there are over 1,000 some of which exist in nature, but most of which have been created synthetically in laboratories in nuclear reactors or cyclotrons. Although accelerators do create small quantities of lingering radioactivity, they do not pose the staggering high - level waste and proliferation problems associated with nuclear reactors, nor do they have any potential for catastrophic accidents of any kind, nor are they capable of producing weapons materials in militarily significant amounts.

It should be recognized that RI have been used in nuclear medicine, industry and scientific research (solids).

5.2.1. Human health.

Nuclear Medicine is a branch of medicine that uses radiation to provide information about the functioning of a person's specific organs or to treat disease. In most cases, the information is used by physicians to make a quick, accurate diagnosis of the patient's illness. The thyroid, bones, heart, liver and many other organs can be easily imaged, and disorders in their function revealed. In some cases radiation can be used to treat diseased organs, or tumors (see, e.g. 34, 35]). Five Nobel Laureates have been intimately involved with the use of radioactive tracers in medicine.

In the developed countries (26% of world population) the frequency of diagnostic nuclear medicine is 1.9% per year, and the frequency of therapy with radioisotopes is about one tenth of this. In Europe there are some 10 million nuclear medicine procedure per year. The use of radiopharmaceuticals in diagnosis of growing at over 10% per year. Nuclear medicine was developed in the 1950s by physicians with an endocrine emphasis, initially using iodine - 131 to diagnose and then treat thyroid disease. In recent years specialists have also come from radiology, as dual CT/PET (see below) procedures have become established.

As is well - known, diagnostic techniques in nuclear medicine use radioactive tracers which emit gamma rays from within the body. These tracers are generally short - lived isotopes linked to chemical compounds which permit specific physiological processes to be scrutinized. They can be given by injection, inhalation or orally. The first type where single photons are detected by a gamma camera which can view organs from many different angles. The camera builds up an image from the points from which radiation is emitted; this image is enhanced by a computer and viewed by a physician on a monitor for indications of abnormal conditions [419, 420].

A more recent development is Positron Emission Tomography (PET [36, 421, 422]) which is a more precise and sophisticated technique using isotopes produced in a cyclotron. A positron - emitting radionuclide is introduced, usually by injection, and accumulates in the target tissue. As it decays it emits a positron, which promptly combines with a nearby electron resulting in the simultaneous emission of two identifiable gamma rays in opposite directions. These are detected by a PET camera and give very precise indication of their origin. PET's most important clinical role in oncology, with fluorine - 18 as the tracer, since it has proven to be the most accurate non - invasive method of detecting and evaluating most cancers. It is also used in cardiac and brain imaging [36]. This particular image shows brain activity of a patient with Alzheimer's disease in Fig. 80.

New procedure combine PET with computed X - ray tomography (CT) scans to give coregistration of the two images (PETCT), enabling 30% better diagnosis than with traditional gamma camera alone. It is powerful and significant tool which provides unique information on a wide variety of disease from dementia to cardiovascular disease and cancer (oncology). Positioning of the radiation source within the body makes the fundamental difference between nuclear medicine and

other imaging techniques such as x - rays. Gamma imaging by either method described provides a view of the position and concentration of the radioisotope within body. Organ malfunction can be indicated if the isotope is either partially taken up in the organ (cold spot), or taken up in excess (hot spot). If a series of images is taken over a period of time, an unusual pattern or rate of isotope movement could indicate malfunction in the organ. A distinct advantage of nuclear imaging over x - ray techniques is that both bone and soft tissue can be imaged very successfully. This has led to its common use in developed countries where the probability of anyone having such a test is about one in two and rising.

Besides diagnosis the RI is very effective used in radiotherapy. Rapidly dividing cells are particularly sensitive to damage by radiation. For this reason, some cancerous growths can be controlled or eliminated by irradiating the area containing the growth. External irradiation can be carried out using a gamma beam from a radioactive cobalt - 60 source, though in developed countries the much more versatile linear accelerators are now being utilized as a high - energy x - ray source (gamma and x- rays are much the same).

Internal radiotherapy is by administering or planting a small radiation source, usually a gamma or beta emitter, in the target area. Iodine - 131 is commonly used to treat thyroid cancer, probably the most successful kind of cancer treatment. It is also used to treat nonmalignant thyroid disorders. Iridium - 192 implants are used especially in the head and breast. They are produced in wire form and are introduced through a catheter to the target area. After administering the correct dose, the implant wire is removed to shielded storage. This brachithrapy (short - range) procedure gives less overall radiation to the body, is more localized to the target tumor and is cost effective.

Treating leukemia may involve a bone marrow transplant, in which case the defective bone marrow will first be killed off with a massive (and otherwise lethal) dose of radiation before being replaced with healthy bone marrow from a donor. Many therapeutic procedures are palliative, usually to relieve pain. For instance, a strontium - 89 and increasingly samarium - 153 are used for the relief of cancer - induced bone pain. Rhenium - 186 is a never product for this (see, also [420,423]).

For some medical conditions, it is useful to destroy or weaken malfunctioning cells using radiation. The radioisotope that generates the radiation can be localized in the required organ in the same way it is used for diagnosis - through a radioactive element following its usual biological path, or through the element being attached to a suitable biological compound. in most cases, it is beta radiation which causes the destruction of the damaged cells. This is radiotherapy. Short - range radiotherapy is known as brachytherapy, and this is becoming the main means of treatment.

Although radiotherapy is less common than diagnostic use of radioactive material in medicine, it is nevertheless widespread, important and growing. An ideal therapeutic radioisotope is a strong beta emitter with just enough gamma to enable imaging, e.g. lutetium - 177. This is prepared from ytterbium - 176 which is irradiated to become Yb - 177 which decays rapidly to Lu - 177. Yttrium -

^{90}Sr is used for treatment of cancer, particularly non-Hodgkin's lymphoma, and its more widespread use is envisaged, including for arthritis treatment.

Iodine - 131 and phosphorus - 32 are also used for therapy. Iodine - 131 is used to treat the thyroid for cancers and other abnormal conditions such as hyperthyroidism (over-active thyroid). In a disease called Polycythemia vera, an excess of red blood cells is produced in the bone marrow. Phosphorus - 32 is used to control this excess. A new and still experimental procedure uses boron - 10 which concentrates in the tumor. The patient is then irradiated with neutrons which are strongly absorbed by the boron, to produce high-energy alpha particles which kill the cancer. Some examples of RI very effectively used in everyday life are presented in Table 19.

5.2.2. Geochronology.

The main data of the geochronology from which all conclusions are based are elemental isotopic abundances of the radionuclides which are largely deduced from meteorites. Meteorites are the prime source of information concerning the earliest stage of the solar system since they have undergone virtually no physical or chemical change since their time of formation approximately $4.6 \cdot 10^9$ years ago. The most primitive meteorites are believed to be carbonaceous chondrites which are largely heterogeneous agglomerations of particles which have undergone little heating since their formation. Other sources of elemental abundance determinations include the Earth, Moon, cosmic rays, Sun, and other stellar surfaces. A key result is the high degree of isotopic homogeneity among the aforementioned sources which supports the nebular hypothesis for the formation of the solar system. The essence of the nebular hypothesis is that the Sun, planets, comets, asteroids and meteorites formed from a common gaseous nebula which was well mixed. The formation of our solar system from a gaseous nebula is not precisely understood and the most extensive work in this area see in [424]. However, the recent determination of small variations in isotopic abundance indicates that some elements of different nucleosynthetic histories were not completely mixed. The understanding of these variations is already constraining the detailed steps of solar system formation by imposing mixing time scales (see, e.g. [2, 22]).

Although it is no surprise that determination of the age of the Earth (geochronology) is based on physical phenomena it is less expected that this is also the case for the chronology of a substantial part of the archaeological record. Of course on Roman sites the layer-by-layer finds, particularly of coins with inscriptions, often permit dating by reference to the enduring writings of contemporary authors, for example Julius Caesar, and in any case such writings establish the basic chronology of the period. To some extent the same is true further back in time, notably by relating to the king-lists giving the reign durations of the Egyptian pharaohs; these lists extend back to the First Dynasty and the earliest pyramid at about 5000 years ago - though even this age is not science-independent since, because of missing sections of the lists, it is reliant on an astronomical calculation of the date of a recorded stellar event (see, also, chapter

2). Beyond 5000 years ago all was conjecture until the so - called "radiocarbon revolution" in the early 1950s [425] ; from then on the 'deeper the older' was replaced by ages based on the laboratory - measured half - life (5568 - 5730 years) of ^{14}C . Today the main dating tool for the last 50,000 years or so is based on the radiocarbon method [426 - 428] (see, also [429]). The main radioactive methods for the periods before the time span of radiocarbon are potassium - argon, uranium - series dating, and fission - track dating. Thermoluminescence (TL) [430 - 433] overlaps with radiocarbon in the time period for which is useful, but also has potential for dating earlier epochs - as do optical dating [431] and electron spin resonance (EPR) - all trapped electron dating methods that rely indirectly on radioactive decay.

The journal *Radiocarbon* publishes the most up - date curves which in principle permit the conversion of radiocarbon dates to calibrated dates. The calibration curve (see Fig. 81) produced by Stuiver et al. [426, 427] combines the available data from tree - rings, uranium - thorium dated corals, and varve - counted marine sediment, to give a curve from 24,000 to 0 Cal BP. Calibration programs and curves can be obtained directly from the Radiocarbon website at www.radiocarbon.org. Several programs are now available which use a statistical methodology, termed Bayesian, to generate probability distributions of age estimations for single ^{14}C . The crucial point is that in any publication it should be indicated whether or not the radiocarbon determination has been calibrated, and if it has been, by which particular system or curve. Radiocarbon dating by the accelerator mass spectrometry (AMS) technique is opening up new possibilities. Precious objects and works of art can now be dated because minute samples are all that is required. In 1988 AMS dating resolved the long - standing controversy over the age of the Turin Shroud (Fig. 82), a piece of cloth with the image of a man's body on it that many genuinely believed to be the actual imprint of the body of Christ. Laboratories at Tucson, Oxford and Zurich all placed it in the 14th century AD (present time), not from the time of Christ at all, although this remains a matter of controversy. Radiocarbon looks set to maintain its position as the main dating tool back to 50,000 years ago for organic materials. For inorganic materials, however, TL and other, new, techniques are very useful (see below).

The preceding techniques are nuclear in the strict sense of the word: the essence of the dating clock is the build - up of a daughter product, as with potassium - argon and uranium - series, or the gradual disappearance of a radioactive isotope, as with radiocarbon. Unlike the preceding techniques luminescence dating is remarkable in utilizing a phenomena of which variants can be seen with the naked eye. There are two variants of luminescence dating: TL and optically stimulated luminescence (OSL), the latter also being referred to as optical dating [431]. For both variants, the latent dating information is carried in the form of trapped electrons; these are electrons which have been ionized by nuclear radiation and which have diffused into the vicinity of a defect in the lattice that is attractive to electrons, for example, such as a negative - ion vacancy, and have become trapped there (see Fig. 83). The nuclear radiation is from radioelements in the sample and in its surroundings; there is also a small

contribution from cosmic rays. The more prolonged the exposure to ionizing radiation the greater number of trapped electrons, which hence increases with years that have elapsed since the last event at which the traps were emptied. This setting of the clock to zero is the event dated and it can be due to the agency of heat, as with pottery, or of light, as with geological sediment. A measure of the number of trapped electrons is obtained by stimulation - by heat in the case of TL and by light on the case of OSL. In either case stimulation causes the eviction of electrons from their traps where upon they diffuse around the crystal until some form of recombination centre is found, such as a defect activated by being charged with a hole. The time spent in diffusion is very short and recombination can be regarded as instantaneous. In the case of a luminescence centre there is emission of light, the color being characteristic of the type of centre. Fig. 83 gives an indication of the overall mechanism; it is an over-simplified representation of reality but forms a useful basis for discussion (for details see also [434]). It is presumed that there is no shortage of activated luminescence centres and also that the radiation flux is not sufficient to cause any significant increase in the number of centres over the age span of the sample. An alternative to the picture given is to consider the process to be dominated by trapped holes; however, although this may represent reality in some cases it is irrelevant to the discussion of most phenomenon and it is convenient to use a description based on trapped electrons (see, also [430]). A similar description is relevant to dating by EPR except that there is then no eviction.

The basis of the evaluation of age is summarized in Fig. 84. The 'natural' signal, that resulting from the natural irradiation during burial, is compared with signals, from the sample, resulting from known doses of nuclear radiation; these are controlled by a calibrated radioisotope source. This procedure allows evaluation of the paleodose, the laboratory dose of nuclear radiation needed to induce 'artificial' luminescence equal to the natural signal. According to [430] the evaluation of age is given by

$$T = \frac{\text{Paleodose}}{\text{Dose - rate}}. \quad (173)$$

The dose - rate represents the rate at which energy is absorbed from the flux of nuclear radiation; it is evaluated by assessment of the radioactivity of the sample and its surrounding burial material, this is carried out both in laboratory and in the field.

At present, together with flint and calcite, the minerals of dominant interest archaeologically are quartz and feldspar, whether from pottery (to which mineral grains are added as temper), from sediment, or from volcanic products (see also [429]). The age range covered by the various types of sample and technique is remarkable - from few tens of years to around half a million. The limitation with quartz and flint is usually due to the onset of saturation - when all traps have become occupied; with feldspar it is more likely to be due to inadequate electron retention in the traps.

Fig. 85 shows an example of a TL glow - curve. A crucial feature of TL measurement is suppression of so - called 'spurious' TL. This is not induced by radiation and is a surface phenomenon which is not well understood - prior inter-grain friction plays a part but there are other influences as well. Fortunately

it can be avoided if the TL oven is flushed with high purity nitrogen or argon, after removal of air; elimination is also enhanced by red - rejection color filters. The glow - curve from a sample in which there is only one trap type consists of a broad peak but in practice several trap types are usually present in a sample and the glow - curve consists of a number of overlapping peaks [434]. For archaeological or geological dating the glow - curve region of interest is upwards of 300°C; below this temperature the TL is from traps that so shallow that they will have suffered serious loss of electrons during the centuries of burial.

5.2.3. Solid state physics.

The first application of radioactive isotopes in solid state physics research dates back almost century , when radioactive lead atoms were used to study self - diffusion in lead [435]. The 'radiotracer diffusion' technique was born . Nowadays it is common method for investigating atomic diffusion processes in solids (see, also above). Up to now approximately 100 different radioactive isotopes have been used (see, Fig. 86) in nuclear solid state physics [31], ranging from ^8Li up to ^{213}Fr . They are produced by nuclear reactions in reactors or at accelerators and the doping of the host lattice is performed either by nuclear reactions inside the material, by recoil implantation or by diffusion or implantation after nuclear production and chemical separation. The radioactive nuclei are used as probes of their structural or electronic environment either in metals [436], insulators [437], semiconductors or superconductors [438] and also on surfaces and interfaces (see above) [439 - 441]. However, a major part of the activity is focused on the investigation of defects and impurities in semiconductors such as Si, Ge, III - V or II - VI compounds.

The characteristic lifetimes of radioactive isotopes can be used to label and identify defect levels in semiconductors which can be detected by photoluminescence [347] and Raman-scattering spectroscopy [348]. Magerle et al. [347] show photoluminescence spectra of GaAs doped with ^{111}In that decays to ^{111}Cd . ^{111}In is isoelectronic to Ga and hence occupies Ga lattice sites in GaAs. It decays to ^{111}Cd with a lifetime $\tau_{111,In} = 98$ h by electron capture [37] . Since the recoil energy of the Cd nucleus due to the emission of the neutrino is much smaller than the typical displacement energy in GaAs [30], ^{111}Cd atoms on Ga sites (Cd_{Ga}) are created by the decay of ^{111}In on Ga sites ($^{111}\text{In}_{Ga}$) and act there as shallow acceptors. This chemical transmutation was monitored by photoluminescence spectroscopy. Figure 87 shows successively taken photoluminescence spectra from the ^{111}In doped sample. A spectrum from the undoped part is also shown. The photoluminescence spectrum of the undoped part of the sample shows the features well known for undoped MBE-grown GaAs [30]. The peaks FX and AX around 819 nm are due to the recombination of free and bound excitons. The peak (e,C) at 830 nm and its LO phonon replica (e,C) - LO at 850 nm are due to recombination of electrons from the conduction band into C acceptor states. The recombination of electrons from donor states into C acceptor states appears as a small shoulder at the right-hand sides of either of these two peaks. C is a residual impurity in GaAs present in MBE-grown

material with a typical concentration between 10^{14} and 10^{15} cm^{-3} [3]. Magerle et al. determined the height I_{Cd}/I_C of the (e, Cd) peak normalized to I_C as the function of time after doping. These was done by subtracting the normalized spectrum of the undoped part from the normalized spectra of the ^{111}In doped part. The height I_{Cd}/I_C of the (e,Cd) peak remaining in these difference spectra is displayed in the insert of Fig. 87. Indicated authors fitted these data by

$$\frac{I_{Cd}}{I_C}(t) = \frac{I_{Cd}}{I_C}(t = \infty) \left(1 - e^{-\frac{t}{\tau}}\right) \quad (174)$$

and obtained a time constant $\tau = 52(17) \text{ h}$, which is not the nuclear lifetime $\tau_{^{111}\text{In}} = 98 \text{ h}$ of ^{111}In . Evidently I_{Cd}/I_C is not proportional to N_{Cd} . The photoluminescence intensity I_{Cd} is proportional to the recombination rate of excess carriers per unit area through Cd acceptors states $\Delta n_L B_{Cd} N_{Cd}$, where B_{Cd} is a recombination coefficient. The excess sheet carrier concentration in the implanted layer Δn_L can be expressed in terms of the total carrier lifetime in the implanted layer τ_L and the generation rate of excess carriers per unit area in the implanted layer $f_L G$ by using the first of the two equilibrium conditions

$$f_L G = \frac{\Delta n_L}{\tau_L} \text{ and } f_B G = \frac{\Delta n_B}{\tau_B}. \quad (175)$$

The second one describes the balance between the generation rate $f_B G$ and the recombination rate of excess carriers $\frac{\Delta n_B}{\tau_B}$ in the bulk. The total generation rate G is proportional to the incident photon flux and $f_L + f_B = 1$. To get an expression for τ_L , cited authors assumed two additional recombination processes in the implanted layer: the radiative recombination via Cd acceptors and nonradioactive recombination due to residual implantation damage, and write the recombination rate in the small single approximation (see, e.g., [3] and references therein) as

$$\frac{\Delta n_L}{\tau_L} = \frac{\Delta n_L}{\tau_B} + \Delta n_L B_{Cd} N_{Cd} + \Delta n_L B_{nr} f_{nr} N_{Cd} \quad (176)$$

Here $\Delta n_L B_{nr} f_{nr} N_{Cd}$ is the nonradioactive recombination rate per unit area due to residual implantation damage, $f_{nr} N_{Cd}$ is the concentration of these non-radioactive recombination centers, and B_{nr} is the corresponding recombination coefficient. Hence Δn_L and Δn_B can be expressed as a function of N_{Cd} and the recombination rates through all the different recombination channels and thereby the relative photoluminescence peak intensities can be deduced. I_C is proportional to the sum of the (e,C) recombination rates per unit area in the implanted layer and the bulk and within this model it can obtain

$$I_C \propto \frac{\Delta n_L + \Delta n_B}{\tau_C} = G \frac{\tau_B}{\tau_C} \left(\frac{f_L}{1 + \Phi_{Cd}/f_B b} + f_B \right). \quad (177)$$

Here Φ_{Cd} is the dose between 10^9 and 10^{13} cm^2 . Thereby $\tau_C = 1/B_C N_C$ is an effective lifetime describing the recombination probability through C acceptor states and b is a constant defined below. With help of Eqs. (175) and (177) it can be obtain (assuming that the detection efficiencies of both peaks are equal) the following relation between I_{Cd}/I_C and Φ_{Cd} :

$$\frac{I_{Cd}}{I_C} = \frac{\Delta n_L B_{Cd} N_{Cd}}{(\Delta n_L + \Delta n_B)/\tau_C} = \frac{a}{1 + b/\Phi_{Cd}}, \quad (178)$$

with

$$a = \frac{f_L}{f_B} \frac{B_{Cd}}{(B_{nr} f_{nr} + B_{Cd})} \frac{\tau_C}{\tau_B} \text{ and } b = \frac{d}{f_B (B_{nr} f_{nr} + B_{Cd}) \tau_B}. \quad (179)$$

This model describes quantitatively the dependence of (e, Cd) intensity of N_{Cd} and cited authors use it to describe the increase of I_{Cd}/I_C with time in the

^{111}In -doped sample. Authors [347] model the change of the carrier lifetime τ_L with time t in the ^{111}In doped sample as

$$\frac{1}{\tau_L} = \frac{1}{\tau_B} + B_{Cd}N_{In} \left(1 - e^{-\frac{t}{\tau}}\right) B_{nr}f_{nr}, \quad (180)$$

where $N_{In} = \Phi_{In}/d$ is the initial ^{111}In concentration, $\tau = \tau_{111In} = 98.0$ h is the nuclear lifetime of ^{111}In , and B_{Cd} , B_{nr} and f_{nr} are the same constants as above. Thereby we assume following Magerle et al. that the same kinds of nonradioactive recombination centers are produced by In doping as by Cd doping and that the Cd concentration are identical to the ^{111}In concentration profile. Taking into account all above saying we can write

$$\frac{I_{Cd}}{I_C} = \frac{\frac{a}{1 + b/\Phi_{In}(1 - e^{-\frac{t}{\tau}})} + c/(e^{-\frac{t}{\tau}} - 1)}, \quad (181)$$

where a and b are the same constants as above and $c = B_{nr}f_{nr}/(B_{nr}f_{nr} + B_{Cd})$. This c term accounts for the fact that the ^{111}In doped sample the concentration of nonradioactive centers is not changing with Cd concentration. Magerle et al. fitted Eq. (181) to the data shown in inset of Fig. 87, keeping $\tau = 98.0$ h, $a = 1.25$ and $b = 3.0 \times 10^{11} \text{ cm}^{-2}$, and obtained $\Phi_{In} = 4.49 \times 10^{11} \text{ cm}^{-2}$ and $c = 0.5$ (2). This fit is shown as a solid line and agrees perfectly with the experimental data. In conclusion of this part it should note that this identification technique is applicable to a large variety of defect levels since for most elements suitable radioactive isotope exist (details see [3]).

Coupling between the LO phonon mode and the longitudinal plasma mode in NTD semi-insulating GaAs was studied in paper [348] using Raman-scattering spectroscopy and a Fourier-transform infrared spectrometer. Raman spectra are shown in Fig. 88 for unirradiated, as-irradiated and annealed samples. The remarkable feature is the low intensity and asymmetric linewidth of the LO-phonon spectrum observed in annealed samples, which are annealed above 600°C . The behavior is not understood by considering the only LO phonon. We should pay attention to the electrical activation of NTD impurities, which begin to activate electrically around 600°C . In the long-wavelength limit, the valence electrons, the polar lattice vibrations, and the conduction electrons make additive contributions to the total dielectric response function [3]:

$$\varepsilon_T(0, \omega) = \varepsilon_\infty + (\varepsilon_0 - \varepsilon_\infty) / [(1 - \omega^2/\omega_t^2) - \omega_p^2\varepsilon_\infty/\omega^2]. \quad (182)$$

The high - frequency value (L_+) of the mixed LO - phonon - plasmon modes is calculated from the roots of the dielectric constant of Eq. (182). The frequencies of the L_+ mode ω and of the longitudinal plasma mode $\omega_p = (4\pi ne^2/\varepsilon_\infty m^*)^{1/2}$ for various annealing temperatures are listed in Table 20. Here n is the electron concentration, m^* the effective mass in the conduction band ($= 0.07m_0$), and ε_∞ ($= 11.3$) the optical dielectric constant. The mixed LO-phonon-plasma mode appears around 300 cm^{-1} for electron concentration of $(0.8-2) \times 10^{17} \text{ cm}^{-3}$. The phonon strength [3] for the high-frequency mode (L_+) of the interacting plasmon - LO - phonon mode is about 0.95 for an electron concentration of $1 \times 10^{17} \text{ cm}^{-3}$, while that for the low-frequency mode (L_-) is below 0.1. Therefore, the asymmetric linewidth of the Raman spectrum observed in the annealed NTD GaAs arises from both the LO-phonon and L_+ modes, but the L_- mode is not observed because of a very weak phonon strength. As a result, the LO-phonon

intensity decreases with increasing coupling, and L_+ mode appears beside the LO-phonon peak.

The absorption spectra in the various annealing temperatures for NTD GaAs are shown in Fig. 89. In unirradiated samples, an absorption around 2350 cm^{-1} is assigned as the antisymmetric stretching vibration of CO_2 arising from CO_2 in an ambient atmosphere. The absorption peaks observed around 500 cm^{-1} are also assigned as a two-phonon overtone scattering [348^a] of transverse optical phonons (TO); these were observed at 493 cm^{-1} [2TO (X)], 508 cm^{-1} [2TO (L)], and 524 cm^{-1} [2TO (Γ)], respectively. In as - irradiated samples, a continuous absorption extending to the higher energy was observed. Although this origin cannot be attributed to interstitial anion clusters as discussed in neutron irradiated GaP [348^b]. In samples annealed above 600°C , the remarkable absorption was observed at wave numbers below 1450 cm^{-1} . The absorption increases with increasing annealing temperature (see Fig. 89). This behavior arises from the free - electron absorption due to the activation of NTD impurities, which occur at annealing temperatures above 600°C . The free-electron absorption observed is consistent with a collective motion as a plasmon mode described in Raman-scattering studies.

Kuriyama et al. [350] were studied by a photoluminescence method the transmuted impurities Ge and S in NTD semi-insulating GaP. In NTD GaP, Ge and S impurities are transmuted from Ga and P atoms by (n,γ) reactions, respectively. Ge in GaP is an amphoteric impurity for which both the donor and acceptor states appear to be deep. The ratio between transmuted impurities Ge and S is about 16 : 1. Unfortunately, after the transmutation reactions, the transmuted atoms are usually not in their original positions but displaced into interstitial positions due to the recoil produced by the γ and β particles in the nuclear reactions. In addition, the defects induced by the fast neutron irradiation disturb the electrical activation of transmuted impurities. However, Frenkel type defects [349] in NTD GaP were annealed out between 200 and 300°C , while P antisite (P_{Ga}) defects of $\sim 10^{18}\text{ cm}^{-3}$ annihilated at annealing temperatures between 600 and 650°C . therefore, transmuted impurities, Ge and S, would be substituted on Ga and/or P lattice sites by annealing at around 650°C .

Fig. 90 shows the photoluminescence (PL) spectra of unirradiated and NTD GaP. The PL spectrum (peak 1) of unirradiated samples shows signature of the DA pair recombination involving S donor and carbon acceptor [348^c]. Two (peaks 2 and 3) of the replicas occur at energies consistent with electronic transitions accompanied by zone-center optical phonons with energies 50.1 meV (LO_Γ) and 100.2 meV (2LO_Γ). Sulfur, silicon and carbon in GaP are the most common as the residual impurities [348^c]. In NTD - GaP the main transition energy was observed 1.65 eV . Since Ge in GaP is the amphoteric impurity with deep acceptor and donor levels, strong phonon co-operation will also occur. but optical transition rates will be significant only for associates. Similar situation has been proposed for Si in GaP [371], forming a nearest-neighbor Si_{Ga} - Si_{P} complex. Therefore, the broad emission would be expected to arise from a nearest-neighbor Ge_{Ga} - Ge_{P} coupled strongly to the lattice. To confirm

the presence of the $\text{Ge}_{Ga} - \text{Ge}_P$ complex, the temperature dependence of the half-width, W , of the broad emission was measured. If the localized electron transitions from the excited state to the ground state of this complex center produce the characteristic luminescence, the dependence would be appear to follow the configuration-coordinate (CC) [371, 3] model equation:

$$W = A[\coth(h\nu/2kT)]^{1/2}, \quad (183)$$

where A is a constant whose value is equal to W as the temperature approaches 0K and $h\nu$ is the energy of the vibrational mode of the excited state. In Fig. 91, Eq. (183) has been fitted to the experimental value for NTD-GaP. For the estimation of W , the spectrum of the 1.65 eV band was subtracted from that of the 1.87 eV band. The value of $h\nu$ used was 0.025 eV. The good fit to this equation that was found for the $\text{Ge}_{Ga} - \text{Ge}_P$ center in NTD-GaP shows the validity of applying the CC model. Results of paper [350] indicate that NTD method is a useful one for introducing Ge donor, resulting from a fact the Ge atoms are transmuted from Ga lattice sites in GaP. The obtained results are consistent with the presence of the $\text{Ge}_{Ga} - \text{Ge}_P$ complex as described earlier (see, e.g. [371]).

To concluding this part we briefly describe the present definition of the kilogram with mass of a certain number of silicon atoms [442 - 451]. To determine a new value of the Avogadro constant with a relative combined standard uncertainty of $2 \cdot 10^{-8}$, the mass determination of a 1 kg ^{28}Si sphere is crucial and should be determination to an unprecedented level of accuracy. By this year, the laboratories involved in the International Avogadro Project (the list of the participants in this Project see e. g. in [446]) should be able to determine the mass of a 1 kg silicon sphere under vacuum with combined standard uncertainty of 4 μg .

The value derived from the slope of the function $M_{\text{Si}} = f(\rho)$ as shown in Fig. 92 leads to what can be considered our best knowledge for the molar volume in single - crystal silicon [445], $M_{\text{Si}}/\rho = 12.0588207(54) \text{ cm}^3\text{mol}^{-1}$. The combination of this value with the 1998 the Committee on Data for Science and Technology (CODATA) recommended value of the Si lattice parameter [452] leads to an Avogadro constant $N_A 6.0221330(27) \cdot 10^{23} \text{ mol}^{-1}$, a candidate for consideration in future adjustments of the values of the constants by CODATA put forward by the CCM Working Group on the Avogadro constant. This value disagrees by more than 1 part in 10^6 with the CODATA 1998 recommended value for N_A based on Planck's constant as determined mainly by watt balance experiments (for details see, also [445, 450]).

Conclusion.

We have discussed the manifestation and origin of the isotope effect. For the first time we review from one point of view the current status manifestation of the isotope effect in a nuclear, atomic and molecular as well as solid state physics. It was shown that although these manifestations of the isotope effect vary, they all have one common feature - they all depend on mass.

In nuclear physics the mass of free particles (proton, neutron) doesn't conserve in the weak interaction process. This contradiction is removed although partly if we take into account the modern presentation that the mass of proton (neutron) is created from quark condensate (not from constituent quarks) which is the coherent superposition of the states with different chirality. Thus the elucidation of the reason of origin of the nucleon mass is taken down to elucidation of the reason to break down the chiral symmetry in Quantum Chromodynamics. In this context we should note that we do not know why the observed mass pattern (M_n , M_p , m_u , m_d , etc.) looks like indicated in text, but nuclear physics analyze the consequence of this empirical fact, but not the reasons of such pattern.

The concordance in the value of binding electron energy between theory and experiments have needed to take into account the nucleus motion. The binding energy corrections due to motion of the nucleus decrease rapidly with increasing nuclear mass. Due to the motion of nucleus, different isotopes of the same element have slightly different the frequency of spectral line. This so-called isotope displacement to the discovery of heavy hydrogen with the mass number $A = 2$ (deuterium). It was shown that each line in the spectrum of hydrogen was actually double. Really, the isotope shift of an optical transition is the sum of two terms: the mass effect and the field effect.

Perhaps the most surprising thing about molecular vibrations (diatomic molecule) is that the frequencies of vibration may be correctly calculated by means of classical mechanics. When an atom of a molecule is replaced by an isotopic atom of the same element, it is assumed that the potential energy function and configuration of the molecule are changed by negligible amount. The frequencies of vibration may, however, be appreciably altered because of the change in mass involved. This especially true if hydrogen is the atom in question because of the large percentage change in mass. This vibration frequency shift or isotopic effect is very simple observed. The direct correlation between vibration frequency and isotope's mass was studied on the example of "fullerene" molecule C_{60} . The observation of essentially equal effects of isotopic substitution of ^{18}O and ^{17}O for ^{16}O on the rates of formation of ozone was called a "non - mass dependent" or "mass - independent" isotopic effect. We should underline that the origin of "mass - independent" isotopic effect doesn't understand well.

In the fourth part of our review we have discussed the effects of isotopic substitution on the physical properties of solids and possible applications we have considered in the last part. Three types of effects have been identified: effects corresponding to the average isotopic mass, effects corresponding to the random distribution of the isotopic masses, and in few cases, effects due to the nuclear spin. In the case thermal expansion we have emphasized the zero - point renormalization of band gap energy, which is strongly affected by the isotopic mass. The energy of zero - point vibrations obtained from experiments in isotope - mixed crystals turned out, as a rule, to be compared (excluding $^{12}C_x^{13}C_{1-x}$, LiH_xD_{1-x} mixed crystals) to the energy of the longitudinal optical phonons. For thermal conductivity, we discussed the effect of mass disorder,

which is particularly important at low temperature. We next discussed the direct effect of average isotopic masses and their random distribution on phonon and exciton (electron) states. The harmonic approximation must be modified to include anharmonicity which depends on the average isotopic masses of each of the constituent elements. This approach is necessary for the first step for the system with strong scattering potential at isotope substitution (for example, $\text{LiH}_x\text{D}_{1-x}$ mixed crystals), which induces $\text{LO}(\Gamma)$ phonons localization in such systems. From this, there follows a necessity of developing such an approach that would lead to a self-consistent model of lattice dynamics, within which a unified description of not only local (small concentration range), but also crystal vibrations of mixed crystals in the whole range of the component's concentrations will be possible. A more consistent way of accounting anharmonicity, beginning, probably, already from the isotope-defect model, is also required. Without such an approach it is impossible to describe neither elastic nor vibrational properties of isotopically mixed crystals. Our view is that it is precisely the consistent way of treating anharmonicity that will allow us to develop such a model of lattice dynamics and will make it possible to describe not only weak, but strong scattering of phonons due to isotopic disorder.

Isotope control and engineering of different solids offers almost limitless possibilities for solid-state investigations and novel devices. First of all we should indicate the "new" reactor technology - neutron transmutative doping (NTD) of solids. Capture of thermal neutrons by isotope nuclei followed by nuclear decay produces new elements, resulting in a large number of possibilities for isotope selective doping of solids. The importance of this technology for studies of the semiconductors for doping materials (for different devices) is underlined.

One of the fundamental processes occurring in all matter is the random motion of its atomic constituents. As simple as diffusion may appear to be, at least conceptually, there still exist many basic unanswered questions. Results from supposedly identical experiments by different groups often scatter by significant factors. This clearly indicates that there are still hidden factors which need to be determined. Even the most thoroughly studied crystals of Si, we will do not know with certainty the relative contributions of vacancies and interstitials to self- and impurity diffusion as a function of temperature, the position of the Fermi level, and external effects such as surface oxidation or nitridation. The isotope control can contribute with new experimental approaches to the study of diffusion and can help in improving our understanding of the many interacting factors. A very accurate method to measure the self-diffusion coefficient uses the isotope heterostructure growing on the same substrate. At the interface only the atomic mass is changing, while all other physical properties stay the same. In as-grown samples, this interface is atomically flat with layer thickness fluctuations about two atomic layers. Upon annealing, the isotopes diffuse into each other (self-diffusion) with a rate that depends strongly on temperature.

The discovery of the linear luminescence of free excitons observed over wide temperature range has placed lithium hydride, as well as diamond crystals, in the row of possible sources of coherent radiation in the UV spectral range. The

elements of fiber - optics using the different values of refractive index of the different isotopes, from which it is easy to produce the core and cladding of the fiber should be mentioned.

The development of efficient quantum algorithms for classically hard problems has generated interest in the construction of a quantum computer. A quantum computer uses superposition of all possible input states. By exploiting this quantum parallelism, certain algorithms allow one to factorize large integers with astounding speed, and rapidly search through large databases, and efficiently simulate quantum systems. In the nearer term such devices could facilitate communication and distributed computing. In any physical systems, bit errors will occur during computation. In quantum computing this is particularly catastrophic, because the errors cause decoherence, and can destroy the delicate superposition that needs to be preserved throughout the computation. With the discovery of quantum error correction and fault - tolerant computing, in which these errors are continuously corrected without destroying the quantum information, the construction of a real computer has become a distinct possibility. In last two decades it was proposed some scheme of quantum processor based on nuclear spin impurity or some isotope of Si.

Finally we mention an application of highly pure ^{28}Si which is now in progress as a part of an international cooperation. This work is motivated by the fact that nearly all fundamental units (meter, second, amper, volt, etc.) can nowadays be based on atomic properties, the only exception being the kilogram. For the purpose of redefining the unit of mass in terms of the atomic mass, an extremely perfect sphere of approximately 1 kg weight is being made of highly pure ^{28}Si .

0.1.1 Acknowledgments.

I would like to express my deep thanks to many authors and publishers whose Figures and Tables I used in my review. Many thanks are due to Prof. W. Reder for carefully reading of my manuscript as well as Dr. P. Knight for improving my English and O. Tkachev for technical assistance. I wish to express my deep gratitude my family for a patience during long preparation of this review.

References.

1. Burbidge E.M., Burbidge G.R., Fowler W.A. and Hoyle F., 1957, Rev. Mod. Phys. **29**, 547.
2. Wallerstein G., Jhen I., Jr, Parker P. et al., 1997, *ibid*, **69**, 995; Esposito S., Primordial Nucleosynthesis: Accurate Prediction for Light Element Abundances, ArXiv:astro-ph/ 9904411.
3. Plekhanov V.G., 2004, Applications of the Isotopic Effect in Solids (Springer, Heidelberg).
4. Gell - Mann M., 1997, The Quark and the Jaguar (Adventures in the Simple and the Complex) (W.H. Freeman and Co., NY).

5. Green A.E.S., 1955, Nuclear physics (McCraw-Hill, NY).
6. Kaplan I., 2002, Nuclear Physics, 2nd ed. (Addison-Wesley, NY).
7. Burcham W.E., 1973, Nuclear Physics. An Introduction. 2nd ed. (Longman, NY).
8. Krane K.S., 1988, Introductory Nuclear Physics (Wiley and Sons, NY - Chichester)
9. Lilley J., 2001, Nuclear Physics (Wiley and Sons, Chichester - NY).
10. Wong S.M., 1998, Introductory Nuclear Physics (Wiley and Sons, Chichester - NY).
11. Hodgston P.E., Gadioli E., and Gadioli-Erba E., 2000, Introductory Nuclear Physics (Oxford University Press, Oxford - NY).
12. Heyde K., 2004, Basic Ideas and Concepts in Nuclear Physics (IOP, Bristol - Philadelphia).
13. Schirokov Ju.M. and Judin N.P., 1980, Nuclear Physics (Science, Moscow) (in Russian).
14. Taylor R.E., 1991, Rev. Mod. Phys. **63**, 573.
15. Kendall H.W., 1991, ibid **63**, 597.
16. Friedman J.I., 1991, ibid **63**, 615.
17. Wilczek F.A., 2005, Uspekhi Fiz. Nauk **175**, 1337 (in Russian).
18. Halzen F. and Martin D., 1984, Quarks and Leptons (Wiley, NY).
19. Striganov A.P. and Donzov Ju.P., 1955, Usp. Fiz. Nauk **55**, 314 (in Russian).
20. Frish S.E., 1963, Optical Spectra of Atoms (Fizmatgiz, M.-L). (in Russian).
21. Sobel'man I.I., Introduction in Theory of Atomic Spectra, 1977, 2nd Ed. (Science, Moscow) (in Russian).
22. King W.H., 1984, Isotope Shift in Atomic Spectra, Plenum, NY.
23. Eliashevich M.A., 1962, Atomic and Molecular Spectroscopy (Fizmatgiz, Moscow). (in Russian).
24. Herzberg G., 1951, Molecular Spectra and Molecular Structure (D. van Nostrand, NY).
25. Wilson E.B., Jr., Decius J.C. and Gross P.C., 1955, Molecular Vibrations. The Theory of Infrared and Raman Vibrational Spectra. (McGraw-Hill, NY).
26. Plekhanov V.G., 2005, Phys. Reports **410**, 1.
27. Cardona M. and Thewalt M.L.W., 2005, Rev. Mod. Phys. **77**, 1173.
28. Plekhanov V.G., 2006, Progr. Mat. Science, **51**, 287.
29. Plekhanov V.G., 2004, Giant Isotope Effect in Solids (Stefan - University Press, La Jola) (USA).
30. Plekhanov V.G., 2003, J. Mater. Science **38**, 3341.
31. Schatz G., Weidinger A. and Gardener A., 1996, Nuclear Condensed Matter Physics, 2nd Ed. (Wiley, NY).
32. Forkel - Wirth D., 1999, Rep. Progr. Phys. **62**, 527.
33. Forkel - Wirth D. and Deicher M., 2001, Nuclear Physics **A693**, 327.

34. Adelstein S.I. and Manning F.Y. (Eds.) 1995, Isotopes for Medicine and Life Science, (National Academy Press, Washington).
35. Gol'din L.L., 1973, Uspekhi-Phys (Moscow) **110**, 77 (in Russian); Amaldi U. and Kraft G., 2005, Rep. Progr. Phys. **68**, 1861.
36. Ter - Pogossian M.M., 1985, in Positron Emission Tomography, ed. by I. Reivich, A. Alovi. (Alan R. Press, NY).
37. Baranov V.Ju., (Ed.) 2005, Isotopes, Vol. 1 and 2 (Fizmatlit, Moscow) (in Russian).
38. Manuel. O., 2001, Origins of Elements in the Solar Systems (Kluwer Academic Press, NY).
39. Simmons E.H., 2000, Top Physics, ArXiv, hep - ph/0011244.
40. Froggatt C.D., 2003, Surveys High Energ. Phys. **18**, 77.
41. Ioffe B.L., 2006, Usp. Fiz. Nauk (Moscow) **176**, 1103 (in Russian).
42. Dolgov A.D. and Zel'dovich Ja.B., 1981, Rev. Mod. Phys. **53**, 1.
43. Linde A.D., 1984, Usp. Fiz. Nauk **144**, 177 (in Russian).
44. Ioffe B.L., 2001, ibid **171**, 1273 (in Russian).
45. Langacker P., 2003, Structure of the Standard Model, ArXiv: hep - ph. 0304186; Novaes S.F., 2000, Standart Model: An Introduction, ArXiv: hep-ph/00012839; Froggatt C.D., Nielsen H.B., Trying to Understand the Standard Model Parameters, ArXiv: hep-ph/0308144; Donoghue J.F., Golowich E. and Holstein B.R., 1992, Dynamics of Standard Model (Cambridge University Press, Cambridge); Burgess C. and Moore G., 2006, Standard Model A Primer, (Cambridge University Press, Cambridge).
46. Royzen I.I., Feinberg E.L., Chernavskaya, 2004, Usp. Fiz. Nauk **174**, 473 (in Russian).
47. Marciano W., and Pagels H., 1978, Phys. Reports **36**, 137; Lee D.W., 1972, Chiral Dynamics (Gordon and Breach, NY; Coleman S., 1985, Aspects of Symmetry (Cambridge University Press, Cambridge).
48. Plekhanov V.G., 1997, Uspekhi - Phys. (Moscow) **167**, 577 (in Russian).
49. Dirac P.A.M., 1958, The Principles of Quantum Mechaniv (Oxford University Press, U.K); Feynman R.P., Leighton R.P. and Sands M., 1965, The Feynman Lecture in Physics, vol.3 (Addison - Wesley, Reading, MA); Landau L.D. and Lifshitz E.M., 1977, Quantum Mechanics (Nonrelativistic Theory) (Pergamon, NY).
50. Grabert H. and Horner H., Eds.1991, Special issue on single charge tunneling, Z. Phys. **B85**, No 3, pp. 317 - 467; Basche T., Moerner W.E., Wild U.P. (Eds.) 1996 Single-Molecule Optical Detection. Imaging and Spectroscopy (VCH, Weinheim).
51. Bell J.S., 1964, Physics **1**, 195; 1966, Rev. Mod. Phys. **38**, 447.
52. Einstein A., Podolsky B. and Rosen N., 1935, Phys. Rev. **47**, 777.
53. Gisin N., Ribvordy G., Tittel W. and Zbinden H., 2002, Rev. Mod. Phys. **74**, 145.
54. Gibbert G., Amrick M., 2000, Practical Quantum Cryptography; A Comprehensive Analysis, ArXiv: quant - ph/ 0009027.
55. Soddy F., 1913, Nature (London) **92**, 399.

56. Frauenfelder H. and Henley E.M., 1991, Subatomic Physics (Prentice Hall, NY).
57. Kelly J.J., 2002, Phys. Rev. **C66**, 065203.
58. Lederer C.M. and Shirley V.S., 1978, Table of Isotopes (Wiley, NY).
59. Aston F.W., 1948, Mass-spectra and Isotopes (Science, Moscow) (in Russian); Blaum K., 2006, Phys. Reports **425**, 1.
60. Cahn R.N. and Goldhaber G.G., 1989, The Experimental Foundations of Particle Physics (Cambridge University Press, Cambridge).
61. Shurtleft R. and Derrington E., 1989, Am. J. Phys. **47**, 552.
62. Barrett R.C. and Jackson D.F., 1977, Nuclear Sizes and Structure (Clarendon, Oxford); Waraquier M., Moreau J., Heyde K., 1987, Phys. Reports **148**, 249.
63. Hornyack W.F., 1975, Nuclear Structures (Academic, NY); Brink B.M. 1965, Nuclear Forces (Pergamon, NY).
64. Carlson J. and Schiavilla R., 1998, Rev. Mod. Phys. **70**, 743.
65. Davies C. and Collins S., 2000, Physics World, August, 35 - 40.
66. Schiff L.I., 1937, Phys. Rev. **52**, 149.
67. Share S.S. and Stehn J.R., 1937, Phys. Rev. **52**, 48.
68. Schwinger J. and Teller E., 1937, *ibid* **52**, 286.
69. Greene G.L, Kessler E.G., 1986, Phys. Rev. Lett. **56**, 819.
70. Gartenhaus S., 1955, Phys. Rev. **100**, 900.
71. Adair R.K., 1950, Rev. Mod. Phys. **22**, 249.
72. Wilson R., 1963, The Nucleon - Nucleon Interaction (Wiley, NY); Henley E.M. and Schiffer J.P., 1998, Nuclear Physics, ArXiv: nucl-th / 9807041.
73. Segre E., 1982, Nuclei and Particles (Reading MA, Benjamin, NY).
74. Arndt R.A., Roper L.D., 1987, Phys. Rev. **D35**, 128.
75. Vinh Mau R., 1979, in, Mesons in Nuclei, Rho M., and Wilkinson D.H. , eds, (North-Holland, Amsterdam).
76. Machleidt R., Holinde K. and Elster Ch., 1987, Phys. Rev. **149**, 1.
77. Heisenberg W., 1932, Zs. Physik **77**, 1.
78. Renton P., 1990, Electroweak Interactions: An Introduction to the Physics of Quarks and Leptons (Cambridge University Press, Cambridge); Holstein B.R., 1989, Weak Interactions in Nuclei (Princeton University Press, Princeton); Paschos E.A., 2007, Electroweak Theory (Cambridge University Press, Cambridge).
79. Edelman S., 2004, Phys. Lett. **B 592**, 1.
80. Roy D.P., 1999, Basic Constituents of Matter and Their Interactions - A Progress Report: ArXiv: hep - ph/9912523.
81. Wilczek F., 2004, The Universe is a Strange Place, ArXiv: astro - ph/0401347.
82. Aitchison I.J.R. and Hey A.J.G., 1990, Gauge Theories in Particle Physics: A Practical Introduction (Adam Hilger, Bristol).
83. Griffiths D.J., 1987, Introduction to Elementary Particles (J.Wiley & Sons, NY).
84. Volcarce A. , Fernandez and Gonzalez P., 2005, Rep. Progr. Phys. **68**, 965.

85. Wagner W., 2005, *ibid* **68**, 2409.
86. Gross D.J., 2005, *Rev. Mod. Phys.* **77**, 837.
87. Politzer D., 2005, *ibid*, **77**, 851.
88. Wilczek F., 2005, *ibid*, **77**, 857.
89. Abbas A., 2001, *Mod. Phys. Lett.* **A16**, 755; 2004, **A19**, 2365.
90. Yndurain F.I., 1999, *The theory of Quark and Gluon Interactions* (Springer, Berlin).
91. Satz H., 1985, *Ann. Rev. Nucl. Sci.* **35**, 245; Celik T., Engles J. and Satz H., 1985, *Nuclear Physics* **B256**, 670.
92. Walecka J.D., 1995, *Theoretical Nuclear and Subnuclear Physics* (Oxford University Press, Inc., NY).
93. Glashow S.L., 1995, *Nucl. Phys.* **22**, 579; Weinberg S., 1967, *Phys. Rev. Lett.* **19**, 1264; Salam A., 1968, in, *Elementary Particle Theory*, Proc. Eighth Nobel Symposium, ed. Svartholm N., p. 367; Weinberg S., 2004, *The Making of the Standard Model*, ArXiv: hep - ph /0401010.
94. Weinberg S., 1994, *Strong Interactions at Low -Energies*, ArXiv: hep - ph/ 9412326.
95. Epelbaum E., Meissner U.-G., Glöckle W., 2003, *Nucl. Phys.* **A714**, 535; Meissner U.-G., 2005, *Quark Mass Dependence of Baryon Properties*, ArXiv: hep-ph/0509029; Müller B., 2007, *From Quark - Gluon Plasma to the Perfect Liquid*, ArXiv: nucl - th/ 0710.3366; Weise W., 2008, *Overview and Perspectives in Nuclear Physics*, ArXiv: nucl - th/ 0801.1619.
96. Ecker G., 1995, *Chiral Perturbation Theory*, ArXiv:hep - ph/9501357; Pich A., 1995, *Chiral Perturbation Theory*, ArXiv:hep - ph/9502366; Bean S.R., Bedaque P.F., Haxton W.C., 2001, in, "At the Frontier of Particle - Handbook of QCD", ed. by Shifman M. (World Scientific, Singapore); Weise W., 2007, *Yukawa's Pion, Low - Energy QCD and Nuclear Chiral Dynamics*, ArXiv: nucl - th/ 0704.1992; Bijens J., *Chiral Perturbation Theory Beyond One Loop*, ArXiv: hep-ph/0604043; 2007, *Progr. Part. Nucl. Phys.* **58**, 521.
97. Yukawa Y., 1935, *Proc. of the Physico - Mathematical Society*, **17**, 48.
98. Frosch R.F., Hofstadter R., McCarthy J.R., 1968, *Phys. Rev.* **174**, 1380.
99. Heilig K. and Steudel A., 1974, *At. Data Nucl. Data Tables* **14**, 613; Brandt H.W., Heilig K. and Steudel A., 1977; *Phys. Lett.* **A64**, 29; Aufmuth F., Heilig K. and Steudel A., 1987, *At. Data Nucl. Data Tables* **37**, 445.
100. Kelic A., Schmidt K.-H., Enqvist T., 2004, *Phys. Rev.* **C70**, 064608.
101. Shpol'sky E.V., 1974, *Atomic Physics, Part One* (Fiz-Mat. Lit., Moscow) (in Russian).
102. Shera E.B., Ritter E.T., Perkins R.B., 1976, *Phys. Rev.* **C14**, 731.
103. Lee P.L., Boehm F. and Hahn A.A., 1978, *Phys. Rev.* **C17**, 1859.
104. Bertolozzi W., Friar J., Heisenberg J., 1972, *Phys. Lett.* **B41**, 408.
105. The prehistory of quark masses is reviewed in Grasser J. and Leutwyller H., 1982, *Phys. Rep.* **87**, 77.
106. Leutwyller H., *Masses of the Light Quarks*, ArXiv: hep-ph/9405330; ArXiv: hep-ph/ 9602255; *Insights and Puzzles in Light Quark Physics*, ArXiv:hep-ph/ 07063138.
107. Froggatt C.D., *The Problem of Mass*, ArXiv: hep-ph/0312220.

108. Narison S., 2002, in, QCD as a Theory of Hadrons: from Partons to Confinement, (Cambridge University Press, Cambridge).
109. Procura M., Nusch B.U., Weise W., 2006, Phys. Rev. **D73**, 114510; Musch B., Hadron Masses, ArXiv: hep-ph/0602029.
110. Beane S.R., Orginos K., and Savage M.J., 2007, Nucl. Phys. **B768**, 38.
111. Ioffe B.L., 1995, Nucleon Spin Structure: Sum Rules, Arxiv:hep-ph/9511401.
112. Scherer S. and Schindler M.R., 2005, Chiral Perturbation Theory Primer, ArXiv:hep-ph/0505265.
113. Ioffe B.L., 2006, Progr. Part. Nucl. Phys. **56**, 232.
114. Gell-Mann M., Oakes R.J. and Renner B., 1968, Phys. Rev. **175**, 2195.
115. Pich A and Prades J., 2000, Nucl. Phys. Proc. Suppl. **86**, 236.
116. Ioffe B.L. 1981, Nucl. Phys. **B188**, 317.
117. Altarelli G., 2004, Nucl. Instr. and Methods, **A518**, 1.
118. Pospelov M. and Ritz A., 2005, Electric Dipole Moment as Probes of New Physics, ArXiv: hep-ph/0504231; 2005, Annal. Phys. (NY) **318**, 119.
119. Khriplovich I.B. and Lamoreaux S.K., 1997, CP Violation Without Strangeness: Electric Dipole Moments of Particles, Atoms and Molecules (Springer, Berlin).
120. Djouadi A., 2008, Phys. Rep. **457**, 1.
121. Ramsey-Musolf M.J. and Su S., 2008, *ibid*, **456**, 1.
122. Weinberg C.S., 1989, Rev. Mod. Phys. **61**, 1; The Cosmological Constant Problems, ArXiv:astro-ph/0005265; Tegmark M., Rees M.J., Wilczek F., Dimensionless Constants Cosmology and Other Dark Matters, ArXiv:astro-ph/0511774; Dolgov A.D., Cosmology and New Physics, ArXiv:hep-ph/0606230; Padmanabhan T., 2003, Phys. Rep. **380**, 235; Dark Energy: Mystery of the Millenium, ArXiv:astro-ph/0603114; Fuller G., Hime A., Ramsey-Musolf M., Dark Matter in Nuclear Physics, ArXiv:nucl-ex/0702031.
123. Milton K.A., 2004, J. Phys. A: Math.Gen. **37**, R209; Lamoreaux S.K., 2005, Rep. Prog. Phys. **68**, 201; Mahajan G., Sarkar S. Padmanabhan T., Casimir Effect Confronts Cosmological Constants, ArXiv: astro-ph/0604265.
124. Stacey D.N., 1966, Rep. Progr. Phys. **29**, 171.
125. Bausche J. and Champeau R.-J., 1976, Adv. At. and Mol. Physics, **12**, 39.
126. Arnikaar H.J., 1989, Isotopes in Atomic Age (Wiley, NY).
127. See, e.g. Ramsden E.N. 1985, A - Level Chemistry (Stanley Thornes Publishers, Hull); Malone L.J., 2003, Basic Concepts of Chemistry (Wiley, NY).
128. Kogan V.I., 2000, Uspekhi Fiz. Nauk **170**, 1351 (in Russian).
129. Condon E.U., Shortly G.H., 1953, The theory of Atomic Spectra (Cambridge University Press, Cambridge).
130. Rudzikas Z., 2006 Theoretical Atomic Spectroscopy (Cambridge University Press, Cambridge).
131. Striganov A.P., 1956, Uspekhi Fiz. Nauk **58**, 365 (in Russian).
132. Huber A., Udem Th., Gross B., 1998, Phys. Rev. Lett. **80**, 468.
133. Udem Th. Gross B., Kourogi M., 1997, *ibid*, **79**, 2646.
134. Vinti J.P., 1939, Phys. Rev. **56**, 1120.

135. Rosenrhal J. and Breit G., 1932, Phys. Rev. **41**, 459.
136. Racah G., 1932, Nature (London) **129**, 723.
137. Brix P. and Kopferman H., 1958, Rev. Mod. Phys. **30**, 517.
138. Goorvitch D. Davis S.P. and Kleinman H., 1969, Phys. Rev. **188**, 1897.
139. Martensson - Pendrill A. - M., Gough D.S. and Hannaford P., 1994, Phys. Rev. **A49**, 3351; Berzinsh U., Gustafsson M., Hanstrop D., 1998, Isotope Shift in the Electron Affinity of Chlorine, ArXiv: physics 9804028.
140. Hughes D.S. and Eckart C., 1930, Phys. Rev. **36**, 694.
141. Seltzer E.C., 1969, Phys. Rev. **188**, 1916.
142. Broch E.K., 1945, Arch. Math Natuv. **48**, 25.
143. Haken H., Wolf H.Ch., 2005, The Physics of Atoms and Quanta (Springer, Berlin-Heidelberg).
144. Lee P.L. and Boehm F., 1973, Phys. Rev. **C8**, 819.
145. Eliashevich M.A., 1946, Uspekhi Fiz. Nauk **48**, 482 (in Russian).
146. Anderson A. (ed), 1973, The Raman Effect (Marcell Dekker, Inc. NY).
147. Long D.A., 1977, Raman Spectroscopy (McGraw - Hill, Inc. UK).
148. Grasselli J.G., Snavey M., Bulkin B.J., 1981, Chemical Application of Raman Spectroscopy (Wiley, NY - Toronto).
149. Shymanski H.A. (ed.) 1967, Raman Spectroscopy (Plenum Press, NY).
150. Measures R.M., 1984, Laser Remote Sensing - Fundamentals and Applications (Wiley - Interscience, NY - Singapore).
151. Plekhanov V.G., 2007, J. Phys. Condens. Matter **19**, 086221 (9pp).
152. Banwell C.N., 1983, Fundamentals of Molecular Spectroscopy (Mc - Graw - Hill, London - NY).
153. Bhagavantam S and Venkatarayudu T., 1951, Theory of Groups and Its Applications to Physical Problems (Adha University Press, Waltair).
154. Danielewicz - Ferchmin I and Ferchmin A.R., 2004, Phys. Chem. Liquids **42**, 1 -36.
155. Walrafen G.E., 1964, J. Chem. Phys. **40**, 3249.
156. Chaplin M.F., 2000, Biophys. Chem. **83**, 211.
157. Kroto H.W., 1985, Nature (London) **318**, 162.
158. Kratschmer W., Fositropoulos and Hoffman D.R., 1990, Chem. Phys. Lett. **170**, 167.
159. Martin M.C. and Fabian J., 1995, Phys. Rev. **B51**, 2844.
160. Rosenberg A. and Kendziora C., 1995, ibid, **B51**, 9321.
161. Menendez J., Page J.B., and Guha S., 1994, Phil. Magazine **70**, 651.
162. Guha S., Menendez J., Page J.B., 1997, Phys. Rev. **B56**, 15431.
163. Mauersberger K., 1981, Geophys. Res. Lett. **8**, 935.
164. Thiemens M.H. Heidenreich J.E., 1983, Science **219**, 1073.
165. Thornton E.K. and Thornton E.R. 1970, Origin and Interpretation of Isotope Effect, in Collins C.J. and Bowman N.S. (eds.) Isotope Effects in Chemical Reaction (American Chemical Society Monograph) (Van Nostrand Reinhold Co., NY - London) p.p. 213 - 285.
166. Biegelsen J., Lee M.W. and Mandel F., 1973, Ann. Rev. Phys. Chem. **24**, 407 -440.

166. Weston R.E., 1999, Chem. Rev. **99**, 2115.
167. Thiemens M.H., 1999, Science **283**, 341.
168. Mauersberger K., Krankowsky D., Janssen C. and Schinke R., 2005, Adv. At. Mol. and Optical Physics **50**, 1.
169. Johnston H.S., 1966, Gas Phase Reaction Rate Theory, (The Ronald Press Company, NY).
170. Criss R.E., 1995, Stable Isotope Distribution in Global Earth Physics, A Handbook of Physical Constants (American Geophysical Union, NY).
171. Weston R.E., 2006, J. Nucl. Sci. and Technol. (Japan) **43**, 295.
172. Anderson S.M., Hulsebusch D. and Mauersberger K., 1997, J. Chem. Phys. **107**, 5385.
173. Janssen Ch., Guenther J. and Mauersberger K., 1999, *ibid*, **111**, 7179.
174. Mauersberger K., Erbacher K. and Krankowsky D., 1999, Science, **283**, 270.
175. Hathorn B.C. and Marcus R.A., 1999, J. Chem. Phys. **111**, 4087.
176. Hathorn B.C. and Marcus R.A., 2000, *ibid*, **113**, 9497.
177. Hathorn B.C. and Marcus R.A., 2001, J. Phys. Chem. **A105**, 5586.
178. Gao Y.Q. and Marcus R.A. 2002, J. Chem. Phys. **116**, 137.
179. Gao Y.Q., Chen W -Ch. and Marcus R.A. , J. Chem. Phys. **117**, 1536.
180. Babikov D., Kendrick B.K., Walker R.B., 2002, Chem. Phys. Lett. **272**, 686.
181. Babikov D., Kendrick B.K., Walker R.B., 2003, J. Chem. Phys. **118**, 6298.
182. Babikov D., Kendrick B.K., Walker R.B., 2003, J. Chem. Phys. **119**, 2577.
183. Hulston J.R. and Thode H.G., 1965, J. Geophys. Res. **70**, 3475.
184. Clayton R.N., Grossman L., Mayeda T.K., 1973, Science **182**, 485.
185. Gellene G.I., 1996, Science **274**, 1344.
186. Valentini J.J., 1987, J. Chem. Phys. **86**, 6757; Bates D.R., 1988, Geophys. Res. Lett. **15**, 13; Griffith K.S. and Gellene G.I., 1992, J. Chem. Phys. **96**, 4403.
187. Sehestedy J., Nielsen O.J., Egsgaard H., 1995, J. Geophys. Res. **100**, 20979; 1998, *ibid*, **103**, 3545.
188. Pines D., 1963, Elementary Excitations in Solids (W.A. Benjamin, Inc, NY - Amsterdam).
189. Pekar S.I., 1982, Crystaloptics and Addition Waves (Naukova Dumka, Kiev) (in Ruaaian).
190. Srivastava G.P., 1990, The Physics of Phonons (Hilger, Bristol).
191. Plekhanov V.G., 2007, Isotopes and Their Applications in Quantum Information, Preprint N002 Computer Science College, Tallinn (in Russian).
192. CallawayJ., 1964, Energy Band Structure (Academic, NY).
193. Martin R.M., 2004, Electronic Structure - Basic Theory and Practical Methods (Cambridge University Press, Cambridge).
194. Jones H., 1962, The Theory of Brillouin Zones and Electronic States in Crystals (North - Holland Co., Amsterdam).

195. Ziman J.M. , 1963, *Electrons and Phonons* (Oxford University, London).
196. Ashcroft N.W., Mermin N.D., 1975, *Solid State Physics* (Holt, Rinehart and Winston, NY - Sydney).
197. Kittel Ch., 1972, *Introduction to Solid State Physics* (J. Wiley and Sons, Inc., NY - London).
198. Lax M., Burstein E., 1955, *Phys. Rev.* **97**, 39.
199. Loudon R., 1964, *Adv. Phys.* **13**, 423; Cowley R.A., 1971, in *Raman Effect*, ed. Anderson A (Marcel Dekker, NY).
200. Birman J.L., 1974, in *Handbuch für Physik*, Vol **25/2b** (Springer, Berlin - NY).
201. Agekyan V.F., Asnin A.M., Kryukov V.M., And Markov I.I., 1989, *Fiz. Tverd. Tels* **31**, 101 (in Russian).
202. Fuchs H.D., Etchegoin P. and Cardona M., 1993, *Phys. Rev. Lett.* **70**, 1715.
203. Plekhanov V.G., 2001, *Isotope Effect in Solid State Physics*, in, *Semiconductors and Semimetals*, Vol. **68** (Eds. Willardson R.K. and Weber E.) (Academic, San Diego).
204. Hanzawa H., Umemura N., Nisida Y. and Kanda H., 1996, *Phys. Rev.* **B54**, 3793.
205. Plekhanov V.G., 2003, *Physics - Uspekhi*, **46**, 689.
206. Chrenko R.M., 1988, *J. Appl. Phys.* **63**, 5873.
207. Hass K.C., Tamor M.A., Anthony T.R., and Banholzer W.F., 1991, *Phys. Rev.* **44**, 12046.
208. Solin S.H., Ramdas A.K., 1970, *Phys. Rev.* **B1**, 1687.
209. Plekhanov V.G., 2001, *Materials Sci. & Eng.* **R35**, 141.
210. Elliott R.J., Krumhansl J.A., Leath P.L., 1974, *Rev. Mod. Phys.* **46**, 465.
211. Barker A.S. (Jr), Sievers A.J., 1975, *Rev. Mod. Phys.* **47** (Suppl. 2) s1.
212. Chang I.F., Mitra S.S., 1971, *Adv. Phys.* **20**, 360.
213. Ipatova I.P., 1988, in *Optical Properties of Mixed Crystals* (Modern Problems in Condensed Matter Sciences, Vol. 23, eds. Elliott R.J., Ipatova I.P) Ch.1 (North - Holland, Amsterdam) p. 1.
214. Plekhanov V.G., 1997, *Opt. Spectrosc.* **82**, 95.
215. Plekhanov V.G., 1995, *Phys. Rev.* **B51**, 8874.
216. Plekhanov V.G., 1993, *Opt. Spectrosc.* **75**, 31.
217. Plekhanov V.G., 2001, *J. Raman Spectrosc.* **32**, 631.
218. Plekhanov V.G., 2006, *J. Nucl. Sci. & Technol. (Japan)* **43**, 375.
219. Kapustinsky A.F., Shamovsky L.M., Bayushkina K.S., 1937, *Acta Physicochem. (USSR)* **7**, 799.
220. Plekhanov V.G., Betenekova T.A., Pustovarov V.A., 1976, *Sov. Phys. Solid State* **18**, 1422.
221. Plekhanov V.G., 1998, *Rep. Progr. Phys.* **61**, 1045.
222. Kreingol'd F.I., Lider K.F., Shabaeva M.B., 1984, *Fiz. Tverd. Tela* **26**, 3940 (in Russian).

223. Onodera Y., Toyozawa Y., 1968, J. Phys. Soc. Japan **24**, 341.
224. Kreingol'd F.I., Lider and Solov'ev K.I., 1976, JETP Lett, (Moscow) **23**, 679 (in Russian).
225. Kreingol'd F.I., Lider K.F., Sapega V.F., 1977, Fiz. Tverd. Tela **19**, 3158 (in Russian).
226. Kreingol'd F.I. and Kulinkin B.S., 1986, *ibid* **28**, 3164 (in Russian).
227. Kreingol'd F.I., 1978, *ibid*, **20**, 3138 (in Russian).
228. Bobrysheva A.I., Jeru I.I., Moskalenko S.A., 1982, Phys. Stat. Solidi (b) **113**, 439.
229. Zhang J.M., Giehler M., Ruf. T., 1998, Phys. Rev. **B57**, 1348; Zhang J.M., Ruf T., Lauck R., 1998, *ibid* **B57**, 9716.
230. Meyer T.A., Thewalt M.L.W. and Lauck R., 2004, Phys. Rev. **B69**, 115214 - 5.
231. Bir G.L. and Picus G.E., 1972, Symmetry and Deformation in Semiconductors (Science, Moscow) (in Russian).
232. Thomas D.G., (ed.) 1967, II - VI Semiconducting Compounds (Benjamin, NY).
233. Lastras - Martonez L.F., Ruf. T., Konuma M. and Aspnes D., 2000, Phys. Rev. **B61**, 12946.
234. Karaskaja D., Thewalt M.L.W., Ruf. T., 2003, Solid State Commun. **123**, 87; Karaskaja D., Thewalt M.L.W., Ruf. T., 2003, Phys. Stat. Sol. (b) **235**, 64; Thewalt M.L.W., 2005, Solid State Commun. **133**, 715.
235. Tsoi S., Alawadhi H., Lu X., Haller E.E., 2004, Phys. Rev. **B70**, 193201 - 4; Ramdas A.K., Rodriguez S., Tsoi S. Haller E.E., 2005, Solid State Commun. **133**, 709; Tsoi S., Rodriguez S., Ramdas A.K., 2005, Phys. Rev. **B72**, 153203 - 4.
236. Kim H., Rodriguez S. and Anthony T.R., 1997, Solid State Commun. **102**, 861.
237. Cardona M., 2002, Solid State Commun. **121**, 7.
238. Klochikhin A.A. and Plekhanov V.G., 1980, Sov. Phys. - Solid State **22**, 342.
239. Klemens P.G., 1958, in Solid State Physics: Advances in Research and Applications, Vol.7 (Eds. F. Seitz, D. Turnbull) (Academic, NY).
240. Holland M.G., 1966, in Physics of III - V Compounds (Semiconductors and Semimetals, Vol. 2, eds. Willardson R.K., Beer A.C.) (Academic, NY) p. 3.
241. Touloukian Y.S. Powell R.W., Ho C.Y. Klemens P.G., 1970, Thermophysical Properties of Materials, Vol. 1 (IFI.Plenum Press, NY - Washington).
242. Berman R., 1976, Thermal Conduction in Solids (Clarendon Press, Oxford).
243. Berman R.Z., 1958, Phys. Chemie. Neue Fol. **16**, 10.
244. Callaway J., 1959, Phys. Rev. **113**, 1046.
245. Peierls R., 1955, Quantum Theory of Solids (Clarendon Press, Oxford).
246. Ziman J.M., 1979, Models of Disorder (Cambridge University Press, Cambridge).
247. Pomeranchuk I.Ya., 1942, J. Phys. (USSR) **6**, 237.

248. Geballe T.H., Hull G.W., 1958, Phys. Rev. **110**, 773.
249. Onn D.G., Witek A., Qiu Y.Z, Anthony T.R. and Banholzer W.F., 1992, Phys. Rev. Lett. **68**, 2806.
250. Olson J.R., Pohl R.O., Vandersande J.W., 1993, Phys. Rev. **B47**, 14850.
251. Wei L., Kuo P.K., Thomas R.L., 1993, Phys. Rev. Lett. **70**, 3764.
252. Debye P., 1912, Ann. Phys. **39**, 789.
253. Cardona M., Kremer R.K., Sanat M., Esreicher S.K., Anthony T.R., 2005, Solid State Commun. **133**, 465.
254. Slack G.A., 1973, J. Phys. Chem. Solids **34**, 321.
255. Vandersande J.W., Zolton A., Olson J.R., 1992, Proc. Seventh Int. Conf. on Scattering of Phonons in Condensed Matter (Cornell University, Ithaca).
256. Asen - Palmer M., Bartkowsky K., Gmelin E., Phys. Rev. **B56**, 9431.
257. Capinski W.S., 1997, Appl. Phys. Lett. **71**, 2109.
258. Capinski W.S., Maris H.J., Tamura S., 1999, Phys. Rev. **B59**, 10105.
259. Ruf T., Henn R.W., Asen - Palmer M., 2000, Solid State Commun **115**, 243; Erratum, 2003, ibid, **127**, 257.
260. Inyushkin A.V., 2002, Inorganic Materials **38**, 427; Broido D.A., Ward A., Mingo N., 2005, Phys. Rev. **B72**, 014308/1 - 8.
261. Plekhanov V.G., 2000, Physics - Uspekhi **43**, 1147.
262. Omini M., Sparavigna A., 1997, Nuovo Cimento **D19**, 1537.
263. Sparavigna A., 2002, Phys. Rev. **B65**, 064305; 2003, ibid **B67**, 144305.
264. Hass K.C., Tamor M.A., Anthony T.R. and Banholzer W.F., 1992, Phys. Rev. **B45**, 7171.
265. Fuchs H.D., Grein C.H., Thomsen C., 1991, ibid, **B43**, 4835.
266. Wang D.T., Göbel A., Zegenhagen J., 1997, ibid, **B56**, 13167.
267. Tamura S., 1983, ibid, **B27**, 858.
268. Tamura S., 1984, ibid, **B30**, 849.
269. Widulle F., Serrano J. and Cardona M., 2002, Phys. Rev. **B65**, 075206/1 - 10.
270. Spitzer J., Etchegoin P., Bangolzer W.F., 1993, Solid State Commun. **88**, 509.
271. Vogelgesand R., Ramdas A.K., Anthony T.R., 1996, Phys. Rev. **B54**, 3989.
272. Widulle F., Ruf. T., Ozhogin V.I., 2001, Solid State Commun. **118**, 1.
273. Vast N., Baroni S., 2000, Phys. Rev. **B61**, 9387.
274. Vast N., Baroni S., 2000, Comput. Mater. Sci. **17**, 395.
275. Rohmfeld S., Hundhausen M., Ley L., Pensl G., 2001, Phys. Rev. Lett. **86**, 826.
276. Plekhanov V.G., Altukhov V.I., 1985, J. Raman Spectrosc. **16**, 358.
277. Plekhanov V.G., 2001, Progr. Solid State Chem. **27**, 71.
278. Plekhanov V.G., 1996, Phys. Rev. **B54**, 3869.
279. Elliott R.J., Ipatova I.P., (Eds), 1988, Optical Properties of Mixed Crystals (North - Holland, Amsterdam).

280. Parks C., Ramdas A.K., Rodriguez S., Itoh K.M., 1994, Phys. Rev. **B49**, 14244.
281. Davies G., 1993, Semicond. Sci. Technol. **8**, 127.
282. Permogorov S., Reznitsky A., 1992, J. Lumin. **52**, 201.
283. Efros A.L., Raikh M.E., 1988, in [279], Chapter 5.
284. Lifshitz I.M., 1987, Selected Works (Science, Moscow) (in Russian).
285. Kanehisa V.A., Elliott R.J., 1987, Phys. Rev. **B35**, 2228.
286. Schwabe N.F., Elliott R.J., 1996, *ibid*, **B54**, 5318.
287. Nelson R.J., Holonjak N., Groves W., 1976, *ibid*, **B13**, 5415.
288. Mahanti S.D., Varma C.M., 1972, *ibid*, **B6**, 2209.
289. Mahanti S.D., 1974, *ibid*, **B10**, 1384.
290. Bethe H.A., Salpiter E., 1957, Quantum Theory of One and Two Electron Atoms (Academic, NY).
291. Hama J., Kawakami N., 1988, Phys. Lett. **A126**, 348.
292. Betenekova T.A., Shabanova I.N., Gavrilov F.F., 1978, Fiz. Tverd. Tela **20**, 3470 (in Russian).
293. Ichikawa K., Susuki N., Tsutsumi K., 1981, J. Phys. Soc. Japan **50**, 3650.
294. Rechenberg H., 1999, in, The Casimir Effect 50 Years Later, Bordag M., (Ed.) (World Scientific, Singapore) p. 10.
295. Planck M., 1911, Verh. d. Deutsch Phys. Ges. (2) **13**, 138.
296. Nernst W., and Lindemann F.A., 1911, Z. Electrochem. **17**, 817; Einstein A., and Stern O., 1913, Ann. Phys. **40**, 551.
297. Fan H.Y., 1951, Phys. Rev. **82**, 900.
298. Zollner S., Cardona M and Gopalan S., 1992, *ibid*, **B45**, 3376.
299. Baym G., 1968, Lectures on Quantum Mechanics (Benjamin, NY) p. 98.
300. Lautenschlager P., Garriga M., Vina L., 1987, Phys. Rev. **B36**, 4821.
301. Plekhanov V.G., Phys. Solid Stat. (St. Petersburg) **35**, 1493.
302. Cardona M., 2005, Solid State Commun. **133**, 3.
303. Plekhanov V.G., 2007, Unpublished results.
304. Alawadhi H., Tsoi S., Lu X., 2007, Phys. Rev. **B75**, 205207.
305. Zhernov A.P., 2002, Fiz. Tverd. Tela (St. Petersburg) **44**, 992.
306. Diffusion in Semiconductors and Non - Metallic Solids, 1998, ed. by Beke D.L., Landolt - Börnstein, New Series, Group III, Vol. 33A (Springer, Berlin).
307. Impurities and Defects in Group IV Elements, IV - IV and III - V Compounds, 2002, ed. by Schulz M., Landolt - Börnstein, New Series, Group III, Vol. 41A2, Part α (Springer, Berlin).
308. Impurities and Defects in Group IV Elements, IV - IV and III - V Compounds, 2003, ed. by Schulz M., Landolt - Börnstein, New Series, Group III, Vol. 41A2, Part β (Springer, Berlin).
309. Mehrer H., 2007, Diffusion in Solids (Fundamentals, Methods, Materials, Diffusion - Controlled Processes) (Springer Series in Solid - State Sciences, Vol. 155) (Springer, Berlin) 654 p.

310. Heitjans P., Kärger J., 2008 (Eds), Diffusion in Condensed Matter (Methods, Materials, Models) (Springer, Berlin) 970 p.
311. Bracht H. and Stolwijk N.A., 2002, Solubility in Silicon and Germanium, Landolt - Börnstein, New Series, Group III, Vol. 41A2, Part α (Springer, Berlin).
312. Stolwijk N.A. and Bracht H., 1998, Diffusion in Silicon, Germanium and Their Alloys, Landolt - Börnstein, New Series, Group III, Vol. 33A (Springer, Berlin).
313. Bracht H., 2007, Phys. Rev. **B75**, 035210/1 - 16.
314. Bracht H., Silvester H.H., Sharp I.D., 2007, *ibid*, **B75**, 035211/1 - 21.
315. Tan T.Y., Gösele U.M. and Yu S., 1991, Crit. Rev. Solid State Phys. **17**, 47.
316. Crank J., 1975, The Mathematics of Diffusion (Oxford University Press, London - New York).
317. Fuchs H.D., Walukewicz W., Dondl W., 1995, Phys. Rev. **B51**, 16817.
318. Itoh K., Hansen W.L., Ozhogin V.I., 1993, J. Mater. Res. **8**, 1341.
319. Tan T.Y., You H.M., Yu S., Gösele U.M., 1992, J. Appl. Phys. **72**, 5206.
320. Campbell D.R., 1975, Phys. Rev. **B12**, 2318.
321. Wang L., Hsu L., Erickson J.W., Cardona M., Phys. Rev. Lett. **76**, 2342.
322. Wang L., Wolk J.A., Hsu L., 1997, Appl. Phys. Lett. **70**, 1831.
323. Beernik K.J., Sun D., Treat D.W., 1995, Appl. Phys. Lett. **66**, 3597.
324. Bracht H., Haller E.E., Eberl K and Cardona M., 1999, Appl. Phys. Lett. **74**, 49.
325. Wee S.F., Chai M.K., Gillin W.P., 1997, J. Appl. Phys. **82**, 4842.
326. Larrabee R.D., 1984, (ed) Neutron Transmutation Doping of Semiconductor Materials (Plenum Press, New York - London).
327. Schlimak I., 1999, Fiz. Tverd. Tela **41**, 837 (in Russian).
328. Ionov A.N., Matveev M.N. and Shmik D.V., 1989, J. Techn. Phys. (St. Petersburg) **59**, 169 (in Russian).
329. Brice D.K., 1971, Radiat. Effects **11**, 227.
330. Schlimak I., Ionov A.N., Rentzsch R., 1996, Semicond. Sci. Technol. **11**, 1826.
331. Snöller M.S., 1974, IEEE Trans. Electron. Devices **ED - 21**, 313; Haas W. and Snöller M.S., 1976, J. Electron. Mater. **5**, 57.
332. High - Power Semiconductor Devices, 1976, IEEE Trans. Electron. Devices **ED - 23**.
333. Hass W. and Snöller M.S., 1976, in [332] p. 803.
334. Baliga B.I., 1984, in [326] p. 167.
335. Farmer J.W and Nugent J.C., 1984, in [326] p. 225.
336. Hill M.J. Van Iseghem P.M., Zimmerman W., 1976, in [332] p. 809.
337. Muhlebauer A., Seldak F. and Voss P., 1975, J. Electrochem Soc. **122**, 1113.
338. Lark - Horowitz K., 1951, in, Proc. Conf. on Semicond. Materials, ed. by Henish H.K. (Butterworth, London).

339. Tanenbaum M. and Mills A.D., 1961, J. Electrochem. Soc. **108**, 171.
340. James H.M., Malmrös O., 1976, in [332] p. 797.
341. Van Iseghem P.V., 1976, in [332] p. 823.
342. Dzhakeli V.G. and Kachlishvili G., 1984, Sov. Phys. Semicond. **18**, 926.
343. Gulberg J., 1981, (ed), Neutron - Transmutation - Doped Silicon (Plenum Press, NY).
344. Hamanaka H., Kuriyama K., Yahagi M., 1984, Appl. Phys. Lett. **45**, 786.
345. Klahr C.N., Cohen M., 1964, Nucleonics **22**, 62.
346. Rentzsch R., Friedland K.J. and Ionov A.N., 1988, Phys. Stat. Solidi (b) **146**, 199.
347. Magerle R., Buchard A. Deicher M., 1995, Phys. Rev. Lett. **75**, 1594.
348. Kuriyama K. and Sakai K., 1996, Phys. Rev. **B53**, 987.
- 348^a. Sekine T., Uchinokura K. and Marzuura E., 1977, J. Phys. Chem. Solids **48**, 109.
- 348^b. Kawakubo T. and Okada M., 1990, J. Appl. Phys. **67**, 3111.
- 348^c. Alawadhi H., Vogelgesang R., Chin T.P., 1997, J. Appl. Phys. **82**, 4331.
349. Kuriyama K., Miyamoto Y., Koyama T and Ogawa O., 1999, J. Appl. Phys. **86**, 2352.
350. Kuriyama K., Ohbora K. and Okada M., 2000, Solid State Commun. **113**, 415.
351. Young M.H., Hunter A.T., Baron R., 1984, in [326] p.1.
352. Sze S.M., 1969, Physics of Semiconductor Devices (Wiley, NY).
353. Allan W.B., 1973, Fibre optics - Theory and Practice, (Plenum Press, London - New York).
354. Berezin A.A., 1987, J. Phys. Chem. Solids **48**, 863; *ibid*, 1989, **50**, 5.
355. Pohl R.W., 1947, Introduction into Optics (Moscow) (in Russian).
356. Zhuravleva L.M., Plekhanov V.G., 2007, Method of Fiber's Manufacture, Patent of Russian Federation N 2302381.
357. Thyagarajan K., Ghatok A.K., (ed) 1982, Lasers Theory and Applications (Plenum Press, NY).
358. Klingshirn C., 1987, in Spectrosc. Solid - State Laser Type Matter, Proc. Course Enrico Fermi, Erice (London - New York).
359. Rossi F., Kuhn T., 2002, Rev. Mod. Phys. **74**, 895.
360. Klingshitn C., Haug H., 1981, Phys. Rep. **70**, 315.
361. Lyssenko V.G., Revenko V.I., 1978, Sov. Phys. Solid State **20**, 1238.
362. Johnson Jr. W.D., 1971, J. Appl. Phys. **42**, 2732.
363. Pankov Z., 1971, Optical Processes in Semiconductors (Prentice Hill, Englewood Cliffs, NJ).
364. Dean P.J., Lightowers E.C., Wright D.R., 1965, Phys. Rev. **140**, A352.
365. Haynes J.R., 1960, Phys. Rev. Lett. **4**, 361.
366. Takiyama K., Abd - Elrahman M.I., Fujita T., Oda T., 1996, Solid State Commun. **99**, 793.

367. Collins A.T., Lawson S.C., Davies G., Kanda H., 1990, Phys. Rev. Lett. **65**, 891.
368. Sauer R., Sternschulte H., Wahl S., Thonke K., Anthony T.R., 2000, Phys. Rev. Lett. **84**, 4172.
369. Kawarada H., Yokota T., Hiraki A., 1994, Appl. Phys. Lett. **64**, 451.
370. Ruf T., Cardona M., Anthony T.R., 1998, Solid State Commun. **105**, 311.
- 370^a. Okushi H., Watanabe H., Kanno S., 202, Phjys. Stat. Solidi (a) **202**, 2051; 2003, ibid, **203**, 3226.
371. Dean P.J., 1973, Progr. Solid State Chem. **8**, 1.
372. Basov N.G., Danilychev V.A., Popov Yu.M., 1970, JETP Lett. **132**, 473.
373. Packard J.R., Campbell D.A., Tait W.C. , 1967, J. Appl. Phys. **38**, 5255.
374. Kulevsky L.A., Prokhorov A.M., 1966, IEEE - QE **2**, 584.
375. Haug H., 1982, Adv. Solid State Phys. **22**, 149.
376. Packard J.R., Tait W.C., Campbell D.A., 1969, IEEE - QE **5**, 44.
377. Liu K.C., Liboff R.L., 1983, J. Appl. Phys. **54**, 5633.
378. Plekhanov V.G., 1981, Proc. Int. Conf. LASERS - 80 (STS Press, McClean, VA, USA).
379. Schwenter N., Dossel O., Nahme N., 1982, Laser Technique for Extreme UV Spectroscopy (ATPT, NY).
380. Plekhanov V.G., 1989, Quantum Electron. (Moscow) **16**, 2156 (in Russian).
381. Gross E.F., 1976, Selected Papers (Science, Leningrad).
382. Knox R.S. 1963, Theory of Excitons (Academic Press, London - New York).
383. Brodin M.S., Reznitchenko V.Ya., 1986, in Georgabiani G., Sheinkman M.K., (eds), Physics of A₂B₆ Compounds (Science, Moscow) (in Russian).
384. Berezin A.A., 1986, Kybernetes **15**, 15; 1988, Chemtronics **3**, 116.
385. Schrödinger E., 1935, Naturwissenschaften **23**, 807.
386. Deutsch D., 1985, Proc. Roy. Soc. (London) **400**, 97.
387. Deutsch D., 1998, The fabric of Reality (Penguin Press, Allen Line).
388. Kilin S.Ya., 1999, Uspekhi Fiz. Nauk **169**, 507 (in Russian).
389. Wooters W.K., Zurek W.H., 1982, Nature, **299**, 802.
390. Dieks D., 1982, Phys. Lett. **A92**, 271.
391. Schumacher B., 1995, Phys. Rev. **A51**, 2738.
392. Kadamzev B.B., 1999, Dynamics and Information (UFN, Moscow) (in Russian).
393. Josza R., 1998, in, Lo H K., Spiller T., Popescu S., (eds) Introduction to Quantum Information aqnd Quanrum Computation (World Scientific, London).
- 393^a. Galindo A., Martin - Delgado M.A., 2002, Rev. Mod. Phys. **74**, 347.
394. Spiller T., 1998, in [393] p. 1 - 28.
395. Barenco A., 1998, in [393] p. 143 - 184.
396. Shor P.W., 1994, in Proc. 35 th Annual Symposium on Foundations of Computer Science (Santa Fe, NM, USA).

397. Grove L.K., 1997, Phys. Rev. Lett. **79**, 325.
398. Feinman R., 1982, Int. J. theor. Phys. **21**, 467.
399. Unruh P.W., 1995, Phys. Rev. **A51**, 992.
400. Shor P.W., 1996, Phys. Rev. **A52**, 2493.
401. Valiev K.A., Kokin A.A., 2001, Quantum Computers (RHD, Moscow) (in Russian).
402. Preskill J., 1998, Proc. Roy. Soc. (London) **A454**, 385.
403. Kane B.E., 1998, Nature **393**, 133.
404. Waugh J.S., Slichter C.P., 1988, Phys. Rev. **B37**, 4337.
405. Kane B.E., 2000, Fortschr. Phys. **48**, 1023.
406. Vrijen R., Yablonovich E., Wang K., 2000, Phys. Rev **A52**, 012306/1 - 10.
407. DiVincenzo D.P., 2000, Fortschr. Phys. **48**, 771.
408. Shlimak I., Safarov V.I. and Vagner I.D., 2001, J. Phys.: Condens Matter **13**, 6959.
409. Shlimak I., and Vagner I.D., 2006, ArXiv: cond - matter/0612065.
- 409^a. Yang A., Steger M., Karaiskaj D., 2006, Phys. Rev. Lett. **97**, 227401.
410. Bowden C.M. and Pethel S.D., 2000, Laser Phys. **10**, 35.
411. Schäfler F., 1992, Semicond. Sci. Technol. **7**, 260.
412. Dagata J.A., 1995, Science **270**, 1625.
413. Marchi F., 1998, J. Vac. Sci. Technol. **B16**, 2952.
414. Machida T., Yamazaki T., Ikushina K., 2003, Appl. Phys. Lett. **82**, 409.
415. Yusa G., Muraki K., Takashina K., 2005, Nature **434**, 1001.
416. Kurten M.J. and Uren M.J., 1989, Adv. Phys. **38**, 367.
417. Xiao M., Martin I., Jiang H.W., 2003, Phys. Rev. Lett. **91**, 078301.
418. DiVincenzo D.P., 1995, Phys. Rev. **A51**, 1015.
419. <http://www.nupeace.org/iai/2001/report/B43.pdf>.
420. <http://www.cbvp.com/nmrc/mia.html>.
421. Huang S. - C., 1986, Principles of tracer kinetic modeling in positron emission tomography and autoradiography in, Positron Emission Tomography and Autoradiography: Principles and Applications for the brain and Heart, ed. by M.E. Phelps, M.C. Mazotta, M.R. Schelbert (Raven, NY).
422. Berman S.R., 1997, Positron Emission Tomography of Heart in, Cardiac Nuclear Medicine, 3rd ed, ed. by M.C. Gerson, Health Professions Division (McGraw-Hill, NY); Valk P.E., Bailey D.L., Townsend D.W., 2004, Positron Emission Tomography: Basic Science and Clinical Practice (Springer, New York); Bender H., Palmelo H., Valk P.E., 2000, Atlas of Clinical PET in Oncology: PET versus CT and MRI (Springer, New York).
423. <http://www.vbvp.com/nmrc/nucmed.html>.
424. Gehrels T. (ed), 1978 Protostars and Planets (University of Arizona Press, Tuscon).
425. Libby W.F., 1952, Radiocarbon Dating (University of Chicago Press, Chicago).
426. Stuiver M., Pearson C.W., 1993, Radiocarbon **35**, 1.
427. Stuiver M., Reimer P.J., 1993, *ibid*, **35**, 215.

428. Taylor R.E., 1987, Radiocarbon Dating: An Archaeological Perspective (Academic Press, New York and London; Taylor R.E. and Aitken M.J. (eds.), 1997, Chronometric Dating in Archaeology (Plenum Press, New York).
429. Symabalisty E.M.D. and Schramm D.N., 1981, Rep. Progr. Phys. **44**, 293.
430. Aitken M.J., 1985, Thermoluminescence (Academic, London).
431. Aitken M.J., 1985, Introduction in Optical Dating (Oxford University Press, Oxford).
432. Aitken M.J., Stinger C.B. and Mellars P.A. (eds), 1993, The Origin of Modern Humans and the Impact of Chronometric Dating (Princeton University Press, Princeton, NJ).
433. Aitken M.J., 1999, Rep. Progr. Phys. **62**, 1333.
434. McKeever S.W.S., 1985, Thermoluminescence of Solids (Cambridge University Press, Cambridge).
435. Groh J. and Hevesey G.V., 1920, Ann. Phys. **65**, 318.
436. Lindros M., Hass H., Pattyn H., 1992, Nucl. Instrum. Methods **B64**, 256.
437. Restle M., Quintel H., Ronning C., 1995, Appl. Phys. Lett. **66**, 2733.
438. Amarel V.S., 1998, J. Magn. Mater. **177 - 81**, 511.
439. Lohmuller J., Hass H., Schatz G., 1996, Hyperfine Interact. **97/98**, 203.
440. Granzer H., Hass H., Schatz G., 1996, Phys. Rev. Lett. **77**, 4261.
441. Bertschat H.H., Hass H., Kowallik R., 1997, Phys. Rev. Lett. **78**, 342.
442. Tarbeyev Yu.V., Kaliteyevsky A.K., Sergeyev V.I., 1994, Metrologia **31**, 269.
443. Kuegens U. and Becker P., 1998, Meas. Sci. Technol. **9**, 1072.
444. Bulanov A.D., Devyatych G.G., Gusev A.V., 2000, Cryst. Res. Technol. **35**, 9.
445. Becker P., 2001, Rep. Progr. Phys. **64**, 1945.
446. Becker P., 2001, Metrologia **38**, 85.
447. Becker P. and Gläser M., 2003, Meas. Sci. Technol. **14**, 1249.
448. Becker P., 2003, Metrologia **40**, 366.
449. Mills I.M., Mohr P.J., Taylor B.N., 2005, Metrologia **42**, 71.
450. Picard A., 2006, Metrologia **43**, 46.
451. Becker P., Godisov O.N., Taylor P., 2006, Meas. Sci. Technol. **17**, 1854.
452. Mohr P.J., Taylor B.N., 2000, Rev. Mod. Phys. **72**, 351.

Figure captions.

Fig.1. Structure within the atom. If the protons and neutrons in this picture were 10 cm across, then the quarks and electrons would be less than 0.1 mm in size and the entire atom would be about 10 km across (after <http://www.lbl.gov/abc/wallchart/>).

Fig. 2. Atomic nomenclature.

Fig. 3. Comparison between charge (ρ_{ch}) and magnetization (ρ_m) for the proton (a) and neutron (b). Both densities are normalized to $\int dr r^2 \rho(r) = 1$ (after [57]).

Fig. 4. A mass-spectrum analysis of krypton. The ordinates for the peaks at mass positions 78 and 80 should be divided by 10 to show these peaks in their true relation to the others (after [8]).

Fig. 5. The binding energy per nucleon B/A as a function of the nuclear mass number A (after [12]).

Fig. 6. The radial charge distribution of several nuclei determined from electron scattering. The skin thickness value t is roughly constant at 2.3 fm. The central density changes very little from the lightest nuclei to the heaviest (after [62]).

Fig. 7. Coulomb potential used for defining the nuclear radius R .

Fig. 8. The spherical square-well potential, adjusted to describe correctly the binding energy E_B of the deuteron. The full depth is also given and amounts to $V_0 = U = 38.5$ MeV (after [12]).

Fig. 9. The deuteron wave function for $R = 2.1$ fm (after [8]).

Fig. 10. The potential for deuteron triplet states with even L . The distance is in units of deuteron radius $R = 4.31$ fm (after [70]).

Fig. 11. Schematic diagram of a scattering arrangement. The scattering angle θ is between wave vector \vec{k} , along the direction of the projectile, and \vec{k}' , that of the scattered particle. The result is independent of the azimuthal angle Φ unless the orientation of the spin of one of the particles involved is known (details see in text).

Fig. 12. The effect of a scattering potential is to shift the phase of the scattered wave at points beyond the scattering regions, where the wave function is that of a free particle (after [9]).

Fig. 13. Real part of NN - scattering phase shifts in degrees for low-order partial waves [74]: a - pp - scattering with contribution from the Coulomb potential removed; b - isovector np - scattering, and c - isoscalar np scattering. Filled circles in the 1S_0 and 3S_1 phase shifts of np - scattering are the calculated results using a Paris potential (after [75]).

Fig. 14. Very small changes in the NN wave function near $r = R$ can lead to substantial differences in the scattering length when the extrapolation is made (after [13]).

Fig. 15. Building blocks of matter, fermions have three quarks qqq and antiquarks $\bar{q}q\bar{q}$ as well as bosons are quarks and antiquarks.

Fig. 16. Comparison of a collection in hadronic or nuclear matter phase and within quark - gluon plasma description (after [91]).

Fig. 17. Neutron decay via weak interaction into proton (a) and Feynman diagram of this process (b).

Fig. 18. Typical spectra showing the muonic $2p - 1s$ x-ray doublet for three isotopes of Fe. The two peaks show the $2p_{3/2} \rightarrow 1s_{1/2}$ and $2p_{1/2} \rightarrow 1s_{1/2}$ transitions in the ratio 2 : 1 determined by the statistical weight $(2j + 1)$ of the initial state. The isotope shift can clearly be seen as the change in

energy of the transitions (after [102]).

Fig. 19. Balmer series in the hydrogen emission spectrum. The convergence of the lines to the series limit H_∞ is clearly seen.

Fig. 20. β lines of the Balmer series in a mixture of equal parts hydrogen and deuterium. One sees the isotope effect, which is explained by motion of the nucleus (see text).

Fig. 21. Experimental 1s - 2s spectra in hydrogen and deuterium as measured relatively to selected modes of the optical comb generator (after [132]).

Fig. 22. Alternating measurements of the 1s - 2s transition frequency in hydrogen and deuterium (after [132]).

Fig. 23. The potential energy curve of typical diatomic molecule (solid line) as a function of internuclear distance. The broken line and dotted curves are those of the quadratic and cubic functions that give the best approximation to the curve at the minimum.

Fig. 24. Idealized model of Rayleigh scattering and Stokes and anti - Stokes Raman scattering. Here ν_v is vibration frequency of molecule.

Fig. 25. Spring and ball model - three modes of vibration for H_2O .

Fig. 26. IR (1) and Raman spectra (2) of benzoic acid.

Fig. 27. IR spectra of ordinary and heavy water. Weak bands in the spectrum of 99.5% D_2O , which coincide with characteristic HDO frequencies shown by arrows, are indicative of the sensitivity of the IR spectrum to impurities (after [155]).

Fig. 28. a - unpolarized Raman spectrum in the frequency region of the pentagonal - pinch mode, for a frozen sample of nonisotopically enriched C_{60} in CS_2 at 30 K. The points are the experimental data, and the solid curve is a three - Lorentzian fit. The highest - frequency peak is assigned to the totally symmetric pentagonal - pinch A_g mode in isotopically pure $^{12}C_{60}$. The other two peaks are assigned to the perturbed pentagonal - pinch mode in molecules having one and two ^{13}C - enriched C_{60} , respectively. The insert shows the evolution of these peaks as the solution is heated. b - the points give the measured unpolarized raman spectrum in the pentagonal - pinch region for a frozen solution of ^{13}C - enriched C_{60} in CS_2 at 30 K. The solid line is a theoretical spectrum computed using the sample's mass spectrum, as described in the text (after [161]).

Fig. 29. Pressure dependence of the rate constant for the reaction $O + O_2 \rightarrow O_3$ (after [171]).

Fig. 30. a - First - order Raman scattering spectra Ge with different isotope contents [27] and b - First - order Raman scattering in isotopically mixed diamond crystals $^{12}C_x^{13}C_{1-x}$. The peaks A, B, C, D, E and F correspond to $x = 0.989; 0.90; 0.60; 0.50; 0.30$ and 0.001 [204].

Fig. 31. Second - order Raman scattering spectra in synthetic diamond with different isotope concentration at room temperature [207].

Fig. 32. Second - order Raman scattering spectra in the isotopically mixed crystals LiH_xD_{1-x} at room temperature. 1 - $x = 0$; 2 - 0.42; 3 - 0.76; 4 - 1. The arrows point out a shift of LO(Γ) phonons in the mixed crystals [218].

Fig. 33. The dependence of $\ln(\delta\%) \sim f[\ln(\frac{\partial\omega}{\partial M})]$: points are experimental values and continuous line - calculation on the formul (113) [218].

Fig. 34. Mirror reflection spectra of crystals: 1 - LiH; 2 - $\text{LiH}_x\text{D}_{1-x}$; 3 - LiD; at 4.2 K. 4 - source of light without crystal. Spectral resolution of the instrument is indicated on the diagram (after [221]).

Fig. 35. a - Reflection spectra in the A and B excitonic polaritons region of $\text{Cd}^{\text{nat}}\text{S}$ and Cd^{34}S at 1.3K with incident light in the $\vec{E} \perp \vec{C}$. The broken vertical lines connecting peaks indicate measured enrgy shifts reported in Table 18. In this polarization, the $n = 2$ and 3 excited states of the A exciton, and the $n = 2$ excited state of the B exciton, can be observed. b - Polarized photoluminescence spectra in the region of the $A_n = 2$ and $A_n = 3$ free exciton recombination lines of $\text{Cd}^{\text{nat}}\text{S}$ and Cd^{34}S taken at 1.3K with the $\vec{E} \perp \vec{C}$. The broken vertical lines connecting peaks indicate measured enrgy shifts reported in Table 18 (after [230]).

Fig. 36. a -Signatures of the E_0' and E_1 excitonic band gaps of ^{28}Si observed (dots) in photomodulated reflectivity. The solid line is a theoretical fit using the excitonic line shape. b - Photomodulated reflectivity spectra of isotopically enriched Si exhibiting isotopic shifts of the E_0' and E_1 gaps (after [235]).

Fig. 37. A - Photoluminescence (PL) and wavelength - modulated transmission (WMT) spectra of isotopically enriched ^{30}Si recorded at 20K ; B - The excitonic indirect band gap and the associated phonon energies as a function of M (after [235]).

Fig. 38. Thermal conductivity of natural abundance (1.1% of ^{13}C) diamons (lower squares), isotopically enriched (0.1% ^{13}C) diamond (upper squares), together with the low - temperaturw data of Slack (see [254]) (circles) and high - temperature data of Vandersande et al. (see Ref.[253]). The solid curves are the result of fitting the Callaway theory [244] to the data, using tha same set fitting parameters. The inset shows the calculated thermal conductivity corresponding to 1%, 0.1% and 0.001% ^{13}C concentration according to Callaway theory (after [251]).

Fig. 39. Thermal conductivity of the highly isotopically enriched ^{28}Si sample SI284 (filled circles) and the natural Si reference SINI (open circles). The filled and open triangles are other measurements for highly isotopically enriched ^{28}Si and natural Si, respectively (from Ref. [241]); "plus" symbols denote the "standard" curve for natural Si (from [241]). The thin solid and dashed lines are the theoretical results of [257] for ^{28}Si and natural Si, respectively. The thick solid line has been calculated with the same theory using the actual mass variance g_2 of sample SI284 (see, also Table 19) (after [259]).

Fig. 40. Raman shift of isotopically disordered diamond. The open symbols represent experimental values [204, 264, 270, 271]. The dashed line indicates the harmonic scaling of the phonon frequency within the VCA ($\omega \sim \overline{m}^{-1/2}$). The solid line corresponds to a fit with Eq. (2.40) for $n = 2, 3$ of Ref. [26] to all experimental data, added to the VCA scaling (after [269]).

Fig. 41. Disorder-induced shift of the Raman phonon of diamond as a function of the ^{13}C concentration. The open symbols are Raman experimental

data, whereas the asterisks correspond to ab initio calculations [27, 273]. The solid line is a fit with Eq. (2.40) for $n = 2, 3$ of Ref. [26] to all experimental data. The dotted and dot-dashed lines represent the fits to theoretical values obtained from ab initio and CPA calculations, respectively (after [269]).

Fig. 42. Disorder-induced broadening of the Raman phonon of diamond as a function of the ^{13}C concentration. The filled circles have been obtained from the Raman data by taking into account the corresponding instrumental resolutions and subtracting the anharmonic broadening $\Gamma_{\text{anh}} \approx 2 \text{ cm}^{-1}$ (FWHM). The solid line is a fit with Eq. (2.40) for $n = 2, 3$ of Ref. [26] to these points. The dotted and dot-dashed lines are the corresponding fits to the values obtained from ab initio [272, 273] and CPA [207, 264] calculations, respectively (after [269]).

Fig. 43. Disorder-induced shift of the Raman phonon of Si as a function of the ^{30}Si concentration [272]. The solid line is a fit with Eq. (2.40) for $n = 2, 3$ of Ref. [26] to the experimental data. The dot-dashed line represents the corresponding fit to the values obtained from CPA calculations (after [269]).

Fig. 44. Disorder-induced broadening of the Raman phonon of Si as a function of the ^{30}Si concentration [272]. The solid line is a fit with Eq. (2.40) for $n = 2, 3$ of Ref. [26] to the experimental data. The dot-dashed line represents the corresponding fit to the values obtained from CPA calculations (after [269]).

Fig. 45. Disorder - induced broadening of the Raman modes of the 6H - SiC polytype versus the ^{13}C concentration of the carbon sublattice. The data are taken from [275]. the solid lines represent fits with Eq. (2.40) for $n = 2, 3$ of Ref. [26] to the data points that correspond to the TO(0), TO(2/6) and TO(6/6) phonon modes (after [269]).

Fig. 46. Dependence of the half - width of the line of $2\text{LO}(\Gamma)$ phonons in Raman scattering spectra of (2) the pure crystal LiH and (3) $\text{LiH}_x\text{D}_{1-x}$. Curve (1) shows the profile of the line of exciting light (after [205]).

Fig. 47. Energy of band - to - band transitions E_g as function of isotope concentration in mixed crystals $\text{LiH}_x\text{D}_{1-x}$ at 2 K: 1 - linear dependence of E_g on x in virtual crystal model; 2 - calculation according to Eq. (121), points derived from reflection spectra indicated by crosses, and those from luminescence spectra by triangles (after [221]).

Fig. 48. Concentration dependence of half - width of the line of ground state of exciton in mirror reflection spectra at 2K: 1 - approximation of virtual crystal model; 2 - calculation according to Eq. (122); experimental points indicated by crosses (after [221]).

Fig. 49. Concentration dependence of binding energy of Wannier - Mott exciton; 1 - approximation of virtual crystal model; 2 - calculation according to Eq. (127); experimental points indicated by triangles (after [277]).

Fig. 50. Temperature dependence of the indirect gap of silicon. The points are experimental, the solid curve represents a single Einstein oscillator fit to the experimental points. The dashed line represents the asymptotic behavior at high temperature: its intercept with the vertical axis allows us to estimate the bare gap and thus the zero - point renormalization due to electron - phonon interaction (after [302]).

Fig. 51. Temperature dependence of the indirect gap measured for Ge (dots).

The solid line (through the points and at higher temperature) represents a fit a single oscillator. The thin line below 200 K represents the linear extrapolation of the single - oscillator fit to $T = 0K$, used to determine the zero - point renormalization of - 53 meV (after [27]).

Fig. 52. Energy of the indirect exciton of diamond versus temperature. The points are experimental. The extrapolation of the linear behavior of the fitted curve at high T as a straight line to $T = 0K$ leads to a zero - point gap renormalization of - 370 meV, much larger than the accuracy of 100 meV often claimed for full - blown ab initio calculations (after [27]).

Fig. 53. Zero - point energy renormalization of exciton state in LiH crystals (after [303]).

Fig. 54. Temperature shift of location of maximum of 1s exciton state in the reflection spectrum of crystals, 1 : LiH; 2 : $LiH_{0.25}D_{0.75}$; 3 : LiD. Experimental values are shown by points and the calculated values by full curves (after [221]).

Fig. 55. Schematic of the isotope heterostructure used by Fuchs et al. (after [317]).

Fig. 56. a - Experimental depth of the atomic fraction of ^{70}Ge , ^{72}Ge , ^{73}Ge , ^{74}Ge and ^{76}Ge of a diffusion - annealed sample at $586^{\circ}C$ for 55.55h. The solid line is a theoretical fit of ^{70}Ge ; b - experimental depth profiles of the same samples as in a) but before annealing (after [317]).

Fig. 57. SIMS depth profiles of ^{69}Ga and ^{71}Ga in GaP isotope epilayers annealed at $1111^{\circ}C$ for 231 min. The filled circles represent the calculated ^{69}Ga concentration profile (after [322]).

Fig. 58. SIMS depth profiles of $Al(o)$, $Ga(\square)$ and $^{71}Ga(+)$ in the as - grown $Al^{71}Ga/Al^{69}Ga/^{71}GaAs$ heterostructure (b) [see (a)] and after annealing at $1050^{\circ}C$ for 1800 s [see(b)]. Solid lines in (a) connect the data to guide the eye. Solid lines in (b) show best fits to the experimental profiles (after [324]).

Fig. 59. SIMS concentration profiles of ^{31}P and ^{30}Si after annealing of the P - implanted Si isotope structure at temperatures and times indicated in the figures. The solid line in (a) - (f) represent theoretical best fit. The lower dashed lines show the corresponding super - and undersaturation of self - interstitials and vacancies, respectively. The upper dashed line in (d) is the Si profile that is expected in the case Si diffusion proceeds under intrinsic and thermal - equilibrium conditions (after [314]).

Fig. 60. The dependence of the phosphorus atoms concentration on the neutron irradiation dose of Si crystals and followed annealing at $800^{\circ}C$ during 1 h. The dependence was measured by Hall effect (after [328]).

Fig. 61. Spreading resistance measurements of a thermal neutron irradiation doped silicon slice. Step - length on scan 1 and 2 is $250 \mu m$ and on scan 3 step - length is $50 \mu m$. Starting material has been selected greater than $1500 \Omega cm$ n - type (after [340]).

Fig. 62. Typical lateral microscopic resistivity distributions in conventionally doped silicon and in silicon doped by neutron irradiation (after [333]).

Fig. 63. Photoluminescence spectra for p - type NTD samples; displayed with intensity of luminescence due to .07 eV acceptor held constant for the four spectra (after [351]).

Fig. 64. Relative photoluminescence spectra for four n - type NTD samples. The four spectra are not normalized with respect to each other (after [351]).

Fig. 65. Reflection at a planar interface between unbounded regions of refractive indices n_{co} and $n_{cl} < n_{co}$ showing (a) total internal reflection and (b) partial reflection and refraction (after [30]).

Fig. 66. Isotopic fiber in which the core and cladding are both pure SiO_2 , but with a different isotopic composition (after [354]).

Fig. 67. Light guidance in an optical waveguide by total internal reflection (after [30]).

Fig. 68. Photoluminescence spectra of the indirect - free exciton in the type - IIa diamond under the 215 nm laser excitation with a power density $\approx 100 \text{ kW cm}^{-2}$ at a temperature of (a) 85K, (b) 125K and (c) 300K. The insert is the enlarged spectrum near the B_3 band of (b) (after [366]).

Fig. 69. Logarithmic plots of the time - decay spectra of the B_1 emission in the type - IIa diamond under the 215 nm laser excitation with power a density of $\approx 100 \text{ kW cm}^{-2}$ at temperatures of 85K (\blacktriangle); 125K (\bullet) and 300K (\circ) (after [366]).

Fig. 70. Experimental (closed circles) and theoretical (solid line) variation of the indirect - free exciton lifetimes with temperature in the type IIa diamond (after [366]).

Fig. 71. Schematic representation of pump relaxation and laser transition for (1) a three level system and (2) a four level system (after [28]).

Fig. 72. Photoluminescence spectra of free excitons at 4.2K: (1) LiH; (2) $\text{LiH}_x\text{D}_{1-x}$ and (3) LiD crystals (after [221]).

Fig. 73. Dependence of the line shape of the 2LO replica at 4.2K on the excitation light intensity I_0 : (1) 0.03; (2) 0.09; (3) 0.40 and (4) 1 (after [370]).

Fig. 74. Bloch sphere representation of a qubit (after [393^a]).

Fig. 75. Illustration of two cells in one - dimensional array containing ^{31}P donors and electrons in a Si host, separated by a barrier from metal gates on the surface. "A gates" control the resonance frequency of the nuclear spin qubits, "J gates" control the electron - mediated coupling between adjacent nuclear spins. The ledge over which the gates cross localizes the gate electric field in the vicinity of the donors (after [403]).

Fig. 76. An electric field applied to an A gate pulls the electron wave function away from the donor and towards the barrier, reducing the hyperfine interaction and the resonance frequency of the nucleus. The donor nucleus - electron system is a voltage - controlled oscillator with a tuning parameter α of the order 30 MHz (after [403]).

Fig. 77. Scheme of fabrication of a striped Si layer with a modulated concentration of nuclear spin isotopes (after [408]).

Fig. 78. Schematics of the proposed device. After NTD, ^{31}P donors appear only inside the ^{30}Si - spots and underlying ^{74}Si - strips will be heavily with ^{75}As donors. All sizes are shown in nm (after [409]).

Fig. 79. Schematics of a ^{28}Si nanowire L with an array of ^{30}Si - spots (qubits and non - qubits after NTD). Each spot is supplied by overlying A -

gate, underlying SD - channel and lateral N - gate. This device architecture allows to realize an indirect coupling between any distant qubits (after [409]).

Fig. 80. Present picture (PET) shows brain activity of a patient with Alzheimer's disease (after [422]).

Fig. 81. Calibrated radiocarbon timescale based on Irish oak. The straight line indicates the ideal radiocarbon/calender age timescale (after [426]).

Fig. 82. Part of the Turin Shroud, bearing the image of a man's head. Radiocarbon AMS dating has given a calibrated age range for the cloth of a 1260 - 1390 years of present time (see, however, text).

Fig. 83. Energy - level representation of the thermoluminescence. i - ionization due to exposure of the crystal to the flux of nuclear radiation, with trapping of electrons and holes at defects, T and L, respectively. ii - Storage during antiquity; the lifetime of the electrons in the traps needs to be much longer than the age span of the sample in order that leakage be negligible. The lifetime is determined by the depth E of the trap below the conduction band, and for dating purposes we are interested in those deep enough (~ 1.5 eV) for the lifetime to be the order of a million years or more. iii - To observe thermoluminescence the sample is heated and there is a certain temperature at which the thermal vibration of the crystal lattice causes eviction. Some of these evicted electrons reach luminescence centres, and if so, light is emitted in the process of recombining at those centres. Alternatively, the electron may recombine at a non - luminescence centre (a 'killer' centre) or be captured by a deeper trap (after [430]).

Fig. 84. The event dating, whether in thermoluminescence dating or in optical dating, is the setting to zero, or near zero, of the latent luminescence acquired at some time in the past. With sediment this zeroing occurs through exposure to daylight ('bleaching') during erosion, transport and deposition, whereas with fired materials, it is through heating. Subsequently the latent signal builds up again through exposure to the weak natural flux of nuclear radiation. For OSL the dating signal is obtained by exposure of the grains from the sample to a beam of light; for TL it is obtained by heating (after [433]).

Fig. 85. Natural glow - curve for burned flint from the lower Paleolithic site at Belvedere, Holland (after [430]).

Fig. 86. Radioactive isotopes used for solid state physics experiments (after [32]).

Fig. 87. Photoluminescence spectra of undoped and ^{111}In doped GaAs successively taken 4h; 7h; 12h; 22h; 2d; 4d and 9d after doping. all spectra are normalized to the intensity of the (e, C) peak. In the inset, the height I_{Cd}/I_C of the (e,C) peak in these spectra is shown a function of time after doping with ^{111}In . The solid line is a theoretical fit (see text) (after [347]).

Fig. 88. Raman spectra at room temperature taken for the various annealing temperatures of (100) oriented NTD GaAs irradiated with neutron doses. The coupling L_+ mode is observed at annealing temperature above 600°C (after [348]).

Fig. 89. Infrared - absorption spectra at room temperature taken for the various annealing temperatures of the NTD GaAs used for the Raman scattering

experiments (after [348]).

Fig. 90. Photoluminescence (PL) spectra taken at 15K for unirradiated and NTD - GaP. PL peaks 1, 2 and 3 in unirradiated GaP represent $S_p - C_p$ DA pair recombination, its LO - phonon replica, and 2LO - phonon replica, respectively. 1.65 and 1.87 eV emissions in NTD - GaP are attributed to $Ge_{Ga} - Ge_P$ complex and $S_p - C_p$ DA pair recombination, respectively (after [350]).

Fig. 91. Variation of the half - width W with the square root of the temperature T for the 1.65 eV in NTD - GaP. solid line is a theoretical fit with $h\nu$ 0.025 eV (after [350]).

Fig. 92. Molar mass versus density of Si single crystal samples. The result for the molar volume derived from the linear data is $M_{Si}/\rho = 12.0588207$ (54) $cm^3 mol^{-1}$ (after [446]).

Table 1. Fundamental interactions

Interaction	FQ	Mass	Range (m)	RS	Spin	T C-S (m^2)	TTS (s)
Strong	Gluon	0	10^{-15}	1	1	10^{-30}	10^{-23}
Weak	$W^\pm; Z$	81; 93 GeV/c ²	10^{-18}	10^{-5}	1;1	10^{-44}	10^{-8}
Electromagnetic	Photon	0	∞	$\alpha = 1/137$	1	10^{-33}	10^{-20}
Gravity	Graviton	0	∞	10^{-30}	2	-	-

Here - FQ field quant; RS relative strength; TC-S - typical cross - section; TTS - typical time scale.

Table. 2. The basic properties of the atomic constituents.

Particle	Charge	Mass (u)	Spin (\hbar)	Magnetic Moment (JT ⁻¹)
Proton	e	1.007276	1/2	$1.411 \cdot 10^{-26}$
Neutron	0	1.008665	1/2	$- 9.66 \cdot 10^{-27}$
Electron	- e	0.000549	1/2	$9.28 \cdot 10^{-24}$

Table 3. Sample values of nuclear magnetic dipole moments (after [58]).

Nuclide	$\mu(\mu_N)$
n	- 1.9130418
p	+ 2.7928456
² H(D)	+ 0.8574376
¹⁷ O	- 1.89379
⁵⁷ Fe	+ 0.09062293
⁵⁷ Co	+ 4.733
⁹³ Nb	+ 6.1705

Table 4. Some values of nuclear electric quadrupole moments (after [58]).

² H(D)	+ 0.00288
¹⁷ O	- 0.02578
⁵⁹ Co	+ 0.40
⁶³ Cu	- 0.209
¹³³ Cs	- 0.003
¹⁶¹ Dy	+ 2.4
¹⁷⁶ Lu	+ 8.0
²⁰⁹ Bi	- 0.37

Table 5. Masses of electron, nucleons and some nuclei (after [56]).

Particle	Number of Protons	Number of Neutrons	Mass (MeV)
e	0	0	0.511
p	1	0	938.2796
n	0	1	939.5731
${}^2_1\text{H}$	1	1	1876.14
${}^3_1\text{H}$	1	2	2808.920
${}^3_2\text{He}$	2	1	2808.391
${}^4_2\text{He}$	2	2	3728.44
${}^7_3\text{Li}$	3	4	6533.832
${}^9_4\text{Be}$	4	5	8392.748
${}^{12}_6\text{C}$	6	6	11174.860
${}^{16}_8\text{O}$	8	8	14895.077
${}^{238}_{92}\text{U}$	92	146	221695.831

Table 6. Table of main families of particles.

Family	Particle	Fundamental
Lepton	electron	yes
Lepton	neutrino	yes
Hadron	proton	no
Hadron	neutron	no
Hadron	delta	no
Hadron	sigma	no
Hadron	many	more

	Particle	Symbol	Spin	Parity	BE(MeV)
	Proton	p	1/2	+	
	Neutron	n	1/2	+	
Table 7. Properties of nucleons and few - nucleonssystems.	Deuteron	${}^2\text{H}$	1	+	2.2246
	Triton	${}^3\text{H}$	1/2	+	8.482
	Helion	${}^3\text{He}$	1/2	+	7.718
	Alpha	${}^4\text{He}$	0	+	28.28

Here - BE - binding energy; MM - magnetic moment; QM - quadrupole moment; RMS CR - RMS charge radius.

Table 8. Nucleon - nucleon scattering length (a) and effective range (r_e)
s = 0; T = 1 (fm) s = 1; T = 0 (fm)

pp: a	-17.1±0.2	
pp: r_e	2.794±0.015	
nn: a	-16.6±0.6	
nn: r_e	2.84±0.03	
np: a	-23.715±0.15	5.423±0.005
np: r_e	2.73±0.03	1.73±0.02

Table 9. Characteristics of the quarks.

Flavor	Electric Charge (e)	Mass (GeV/c ²)
u - up	+ 2/3	0.004
d - down	- 1/3	0.008
c - charm	+ 2/3	1.5
s - strange	- 1/3	0.15
t - top	+ 2/3	176
b - beauty (bottom)	- 1/3	4.7

Table 10. Characteristics of the leptons.

Flavor	Electric charge (e)	Spin	Mass (Gev/c ²)
ν_e - electron neutrino	0	1/2	$<7 \cdot 10^{-9}$
e^- - electron	-1	1/2	0.000511
ν_μ - muon neutrino	0	1/2	< 0.00027
μ^- - muno (mu - minus)	-1	1/2	0.106
ν_τ - tau neutrino	0	1/2	<0.03
τ^- - tau (tau - minus)	-1	1/2	1.771

Table 11. The root - mean - square radius ($\langle r^2 \rangle^{1/2}$) for different calcium isotopes.

Nucleus	⁴⁰ Ca	⁴² Ca	⁴⁴ Ca	⁴⁸ Ca
$\langle r^2 \rangle^{1/2}$ (fm)	3.4869	3.5166	3.5149	3.4762

Table 12. The wavelength of some lines of the various spectral series in hydrogen. The series with $m = 3$ was observed in 1924 by Pfund; it begins with a line of $\lambda = 74000\text{\AA}$, but is not shown in the table.

$n \setminus m$	Lyman	Balmer	Paschen	Bracket
2	1216 \AA			
3	1026 \AA	6563 \AA		
4	973 \AA	4861 \AA	18751 \AA	
5	950 \AA	4340 \AA	12818 \AA	40500 \AA
Year of discovery	1906	1885	1908	1922

Table 13. Energy corrections for motion of the nucleus for the Rydberg numbers of several one - electron atoms.

Atom	H(¹ H)	D(² H)	T(³ H)	He ⁺	Li ²⁺
A	1	2	3	4	7
$-\frac{\Delta E}{E} \cdot 10^4$	5.45	2.75	1.82	1.36	0.78

Table 14. The symmetry elements of the C_{2V} point group (see, e.g. [200]).

C _{2V}	E	C ₂	$\sigma_V(xz)$	$\sigma_V(yz)$		
A ₁	1	1	1	1	z	x ² ; y ² z ²
A ₂	1	1	-1	-1	R _z	xy
B ₁	1	-1	1	-1	x, R _y	xz
B ₂	1	-1	-1	1	y, R _x	yz

Table 15. Main vibrations of water isotopologues.

Gas	ν_1, cm^{-1}	ν_2, cm^{-1}	ν_3, cm^{-1}
H ₂ ¹⁶ O	3657.05	1594.75	3755.93
H ₂ ¹⁷ O	3653.15	1591.32	3748.32
H ₂ ¹⁸ O	3649.69	1588.26	3741.57
HD ¹⁶ O	2723.68	1403.48	3707.47
D ₂ ¹⁶ O	2669.40	1173.38	2787.92
T ₂ ¹⁶ O	2233.9	995.37	2366.61

Table 16. Main vibrations of liquid ordinary and heavy water (cm^{-1}).

Vibrations	H ₂ O	D ₂ O
combination of ν_2 + libration	2127.5	1555
ν_2	1643	1209.4
ν_1, ν_2 and overtone of ν_2	3404	2504

Table 17. Values of the energy of maxima (in meV) in exciton reflection spectra of pure and mixed crystals at 2K, and energies of exciton binding E_b , band-to-band transitions E_g (after [221]).

Energy, meV	LiH	LiH _{0.82} D _{0.18}	LiH _{0.40} D _{0.60}	LiD	⁶ LiH (78K)
E_{1s}	4950	4967	5003	5043	4939
E_{2s}	4982	5001	5039	5082	4970
E_b	42	45	48	52	41
E_g	4992	5012	5051	5095	4980

Table 18. The energy shifts of all of the transitions studied in [230] are given in terms of the Cd³⁴S minus the Cd^{nat}S energy, ΔE .

Transition	Method	ΔE (cm^{-1})
I ₂	PL	10.6±0.1
I ₂ ^z	PL	11.1±0.1
I ₂ ^a	PL	10.6±0.1
A _{n=1} (Γ_6)	A	10.8±0.2
A _{n=1} (Γ_5^L)	PL	11.0±0.2
A _{n=1} (Γ_5^L)	R⊥	10.9±0.2
A _{n=2}	PL	11.3±0.4
A _{n=2}	PL⊥	11.1±0.4
A _{n=2}	R⊥	10.2±0.5
A _{n=3}	PL	11.8±1.1
A _{n=3}	PL⊥	10.9±0.6
A _{n=3}	R⊥	10.7±0.6
B _{n=1} (Γ_1)	R	10.9±0.3
B _{n=1} ($\Gamma_5^L + \Gamma_5^T$)	R⊥	10.6±0.4
B _{n=2}	R	9.4±1.2
B _{n=2}	R⊥	9.8±1.2
C _{n=1} (Γ_1)	R	15±6
C _{n=1} (Γ_5)	R⊥	14±5

The methods used were photoluminescence spectroscopy (*PL) and reflection spectroscopy (R). For measurements made using polarized light, the || or ⊥ specifies the orientation of the **E** vector vs the c axis.

Table 19. Some very often used in everyday life RI (see text)

Isotope	Half - life	Applications
Actinium - 225	10.0 d	An alpha emitter that shows promise in the treatment of certain types of cancer
Californium - 252	2.64 y	Used to treat cervical cancer melanoma, brain cancer treatment
Cobalt - 60	5.27 y	A gamma emitter used in irradiations food and medical equipment sterilization
Tungsten - 188	69.8 d	Used to prevent the re - closure (restenosis) of coronary arteries folowing heart surgery
Copper - 67	61.9 h	Used to label monolocal antibodies and destroy target tumors; PET scanning
Strontium - 82	25.6 d	PET scanning
Calcium - 42	Stable	Along with calcium - 44 used in human calcium retention studies
Lithium - 6	Stable	Neutron capture therapy research
Carbon - 11	20.3 m	Radiotracer in PET scans to study normal/abnormal brain function
Germanium - 68	271 d	PET imaging
Bismuth -213	46 m	Used for targeted alpha therapy (TAT) especiallycancers
Holmium - 213	26 h	Being developed for diagnosis and treatment of liver tumours
Iodine - 125	60 d	Used in cancer brachytherapy (prostate and brain)
Iodine -131	8d	Widely used in treating thyroid cancer. A strong gamma emitter, but used for beta therapy
Iridium - 192	74 d	Supplied in wire form for use as an internal radiotherapy source for cancer treatment (used then removed)
H - 3	12.3 y	Labeling PET imaging

Table 20. Electron concentrations and the coupling modes of NTD GaAs (after [348]).

Sample	EC (cm ⁻³)	LO - phonon frequency (cm ⁻¹)	L ₊ mode (cm ⁻¹)	PF (cm ⁻¹)
unirradiated	$1 \sim 2 \times 10^7$	296.6		
as - irradiated	a	295.6		
500 ⁰ C annealed	a	297.8		
600 ⁰ C annealed	8.2×10^{16}	296.0	299	96.4
650 ⁰ C annealed	2.2×10^{17}	296.6	304	158
700 ⁰ c annealed	2.5×10^{17}	296.2	305	168

a) Since the conduction is dominated by Mott-type hopping conduction (M. Satoh and K. Kuriyama, Phys. Rev. B40, 3473 (1989), the electron concentration can not be measured by the van der Pauw method.

EC = Electron Concentration;

PF = Plasma Frequency.